

On the roll damping of surfaced submarines

R.H. Vogels

Master Thesis

Front cover: Photograph of Zr. Ms. Zwaardvis at sea.

Source: <http://www.rdm-archieff.nl/RDM-NB/RDM-320.htm> (accessed April 7, 2015)

On the roll damping of surfaced submarines

MASTER THESIS

For the degree of Master of Science in Maritime Technology at Delft
University of Technology

R.H. Vogels

June 1st, 2016

Graduation committee:

prof. dr. ir. R.H.M. Huijsmans	Delft University of Technology
dr. ir. J.A. Keuning	Delft University of Technology
SBN-b.d. ir. K. Visser	Delft University of Technology
ir. B. Nienhuis	Defence Materiel Organisation

Abstract

This thesis investigates the roll damping of surfaced submarines. Modern diesel-electric submarines can spend a significant time sailing in surfaced condition. When sailing in this condition, the submarine will roll due to the excitation by waves. The (very) large rolling angles that occur are bothersome to the crew and possibly dangerous to the submarine and its systems. The large angles occur, because the roll damping of a submarine is low when compared to ordinary surface ships. The rudders contribute the most to the roll damping of a submarine. Hardly any research into the roll damping of submarines is found in the open literature. For these reasons, the following research question is formulated:

Which rudder configuration provides the most roll damping for a surfaced submarine at speed?

Six different rudder configurations are compared over a range of roll amplitudes, roll frequencies and forward speeds. The comparison is made using a newly developed mathematical model. The mathematical model calculates the lift and drag forces generated by the rudders using thin airfoil theory, whilst taking the effects of very high angles of attack and the vicinity of the free surface into account.

The model is validated against an extensive series of experiments on a model submarine. The model submarine had a scale of 1:24. Forced oscillation tests were performed at the towing tank of Delft University of Technology. Forces normal to the rudders and the torque acting on the hull were measured.

The results of the experiments showed that the mathematical model could be used to predict the qualitative trends in the roll damping of surfaced submarines. For every combination of roll amplitude, roll frequency and forward speed that was studied, the trend was similar: the large X-rudders with bowplanes generate the most roll damping. Adding bowplanes to a given aft rudder configuration always increases the roll damping.

Contents

Abstract	i
1 Introduction and problem statement	1
2 Theory: Equation of motion	5
2-1 Rotation of a rigid body	5
2-1-1 Definition of coordinate systems	5
2-1-2 Equation of motion	6
2-2 Non-linear roll damping	7
2-3 Damping components	7
3 Damping through appendages	11
3-1 Flow definitions	11
3-2 Rudder dimensions	12
3-3 Generation of lift	13
3-3-1 Two-dimensional flow	14
3-3-2 Three-dimensional flow	14
3-3-3 Hull effects	15
3-3-4 Vicinity of the free surface	16
3-3-5 Ventilation	18
3-3-6 Variation of the angle of attack	19
3-3-7 High angles of attack and stall	22
3-4 Drag	24
3-5 Correction for unsteady flow	25
3-6 Normal force	26
3-7 Mathematical model	28

4	Experimental set-up	29
4-1	Measuring the roll damping	29
4-1-1	Roll decay test	29
4-1-2	Oscillating moment	30
4-1-3	Forced oscillation	30
4-1-4	Forces to be measured	30
4-2	Properties of the model	31
4-3	Forcing the roll motion	33
4-3-1	Hexamove	33
4-3-2	Linear drive with scotch yoke	33
4-4	Mounting of the model	34
4-5	Measurement equipment	37
4-6	Measurement matrix	37
5	Data processing	41
5-1	Clipping measurement signals	41
5-2	Minimum amplitude condition	41
5-3	Unreliable experimental results	43
5-4	Noise	43
5-5	Spectral components of the signal	43
5-6	Base of comparison	44
5-7	From forces to moments	46
5-8	Determination of in and out of phase parts of the moment	49
6	Results	51
6-1	Usable measurements	51
6-2	Repeatability	51
6-3	Validation of the mathematical model	53
6-3-1	Bowplanes	53
6-3-2	Aft rudders	55
6-4	Bare hull	62
7	Conclusions	65
7-1	Conclusions	65
7-2	Recommendations for further research	66
A	Sonar flankarrays	69
A-1	Assumptions	69
A-2	Calculations	70
B	Partial flooding of the casing	73
B-1	Assumptions	73
B-2	Calculations	75
B-3	Conclusion	76

C	Lift coefficients of the NACA 0018 foil	79
D	Experimental results	81
D-1	Bowplanes	82
D-2	Aft rudders	96

Introduction and problem statement

Submarines are designed to operate below the water surface. However, diesel-electric submarines can spend a significant time sailing in the free surface, rather than being submerged. There are several reasons for this, both technical and operational. For instance, submarines cannot dive when the water depth is smaller than the safe operating depth. The North Sea for instance, is generally considered to be too shallow for submerged sailing. An operational reason is the fact that submarines may not be allowed to dive in areas where other submarines are known to be present.

The increased distance to operational areas and longer surfaced sailing times have shown that submarines are prone to severe rolling motions in bad weather conditions. Extreme rolling angles of forty-five to fifty degrees are mentioned by Efimov et al. (2003) in sea state 6-7. Rolling angles of fifteen degrees or more are not uncommon, even in moderate sea states. These large rolling angles are bothersome to the crew and possible dangerous to the structure of the submarine and its systems due to the increased loads.

The roll amplitude is strongly dependent on the roll damping. The shape of most submarine hulls is such that very little roll damping is expected: the hull resembles closely a circular cylinder with hardly any protrusions, other than the rudders. The reported large rolling angles are thus not unexpected.

Hardly any research into the roll damping of surfaced submarines has been found in the open literature. This thesis attempts to partially close this gap by investigating the roll damping of submarines sailing in a surfaced condition. For a typical submarine hull, as shown in Figure 1-1, the rudders are assumed to contribute the most to the roll damping. The sail of the submarine is above the water surface when sailing in the free surface and does not contribute to the roll damping. Although the roll damping could be increased by the use of bilge keels, it is felt that bilge keels would be an unwanted appendage. They would generate underwater noise, which increases the submarines detectability. Rudders will also generate underwater noise, but are indispensable to a submarine. Hence the focus of this thesis on different rudder configurations:

Which rudder configuration provides the most roll damping for a surfaced submarine at speed?

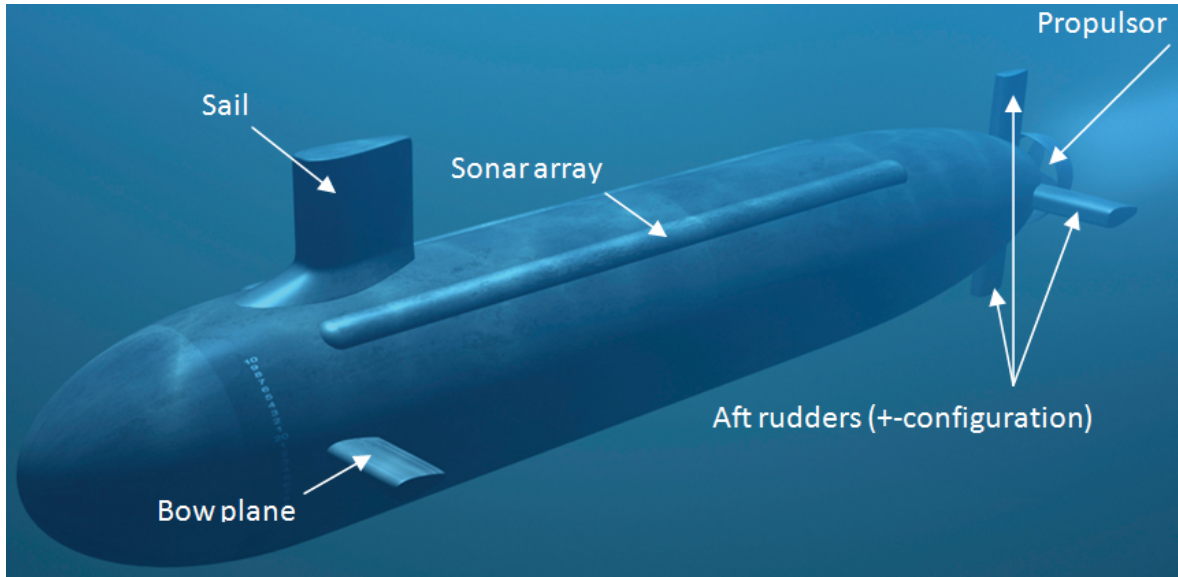


Figure 1-1: A typical submarine with bowplanes and aftrudders in +-configuration.

Source: <http://www.army-suppliers.info/supplier/bruel-and-kjaer> (accessed on April 15, 2016)

The rudder configurations that will be investigated are:

- Rudders in +-configuration
- Rudders in X-configuraton
- Bowplanes

The +-configuration of the aft rudders is shown in Figure 1-1. When the aft rudders are rotated by 45° , the configuration is called an X-configuration. A sketch of the rudder configurations is shown in Figure 1-2. The +- and X-configuration are the two configurations of the stern mounted rudders that are currently in use on submarines. In addition to these stern mounted rudders, submarines have a pair of diving planes that may either be mounted on the sail or on the bow of the submarine. When mounted on the bow, as is shown in Figure 1-1, these rudders contribute to the roll damping in the surfaced condition. Sail mounted dive planes are far above the water surface in surfaced condition and do not contribute to the roll damping.

For the purpose of this thesis, the rudders are assumed to remain fixed, i.e.: the rudders will not be actively or passively controlled. It is a fair assumption that active control of the rudders may increase the roll damping significantly, but active roll damping is out of scope for this thesis.

The span of the aft rudders is assumed to be maximized within the bounding box surrounding the submarine hull. This is a fair assumption: keeping the span within the bounding box prevents the rudders from damage whilst mooring or grounding. A span smaller than the span allowed by the bounding box is unlikely: a larger span is more beneficial for the course keeping stability and manoeuvrability of the submarine.

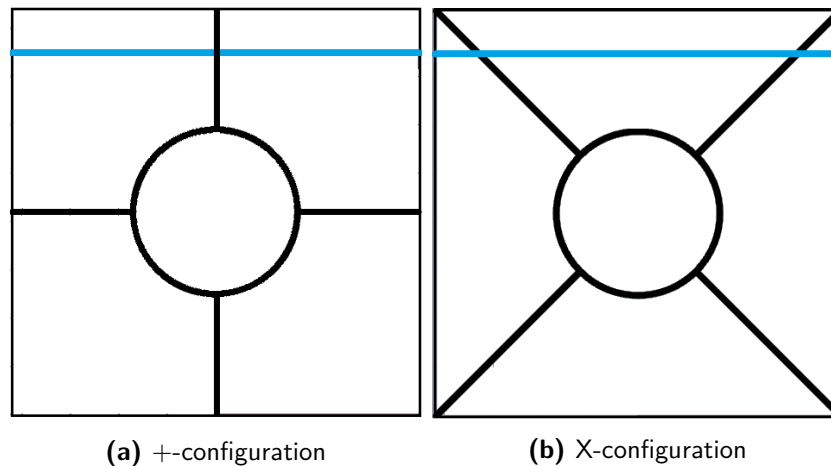


Figure 1-2: The two aft rudder configurations investigated in this thesis.

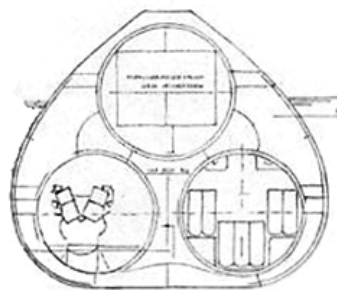


Figure 1-3: The cross-section of a three cylinder submarine.

Source: <http://rdm-archieff.nl/RDM-NB/RDM-280> (accessed December 16, 2015)

The submarine considered for this thesis is a diesel-electric submarine with a more or less circular cross-section. Although other hull shapes exist, such as the three cylinder shown in Figure 1-3, they will not be investigated in this thesis.

To answer the research question, a mathematical model is developed to calculate the roll damping of a surfaced submarine. The model is validated against experimental data. A rather extensive series of experiments have been carried out to determine the hard to measure roll damping. The usable data of these experiments is used to validate the mathematical model.

First, in Chapter 2, the equation of motion for a rolling submarine and the factors that contribute to the roll damping are introduced. In Chapter 3, the generation of forces by the rudders is studied. Chapter 4 describes the experiments that have been performed in the towing tank of Delft University of Technology, while Chapter 5 describes the way in which the experimental data is processed to create usable information. Chapter 6 will discuss the results of the experiments. Finally, in Chapter 7 conclusions are drawn and recommendations for further research are given.

Theory: Equation of motion

This chapter describes the theory behind the roll motion of a submarine. Attention will be given to the mathematical description of a rotating body (Section 2-1) and to the (non-linear) damping of the roll motion (Section 2-2).

2-1 Rotation of a rigid body

A rolling submarine behaves as a rigid body: any deformations of the submarine during the motion are small enough to be neglected. In this section the reference coordinate systems will be introduced and the equation of motion for a rotating rigid body will be presented.

2-1-1 Definition of coordinate systems

Throughout this thesis, two right handed coordinate systems will be used:

1. A ship bound coordinate system x_b, y_b, z_b , with the x-axis pointing forward and coinciding with the axis of rotation of the submarine¹. The y-axis points to port and the z-axis is pointing vertically upwards. The origin is placed on the vertical line passing through the center of gravity. This coordinate system is shown in Figure 2-1.
2. A directionally fixed coordinate system x, y, z . This coordinate system coincides with the ship bound coordinate system when the ship is at rest. However, rather than being bound to the ship, the directionally fixed coordinate system moves with the average velocity of the ship.

The roll motion of a submarine is defined as a rotation φ around the x-axis in the directionally fixed coordinate system. Forces are measured in the ship bound coordinate system.

¹In general, ships are assumed to rotate around their center of gravity. (Surfaced) submarines are not different in that respect. In this research however, the axis of revolution of the hull is chosen as the axis of rotation for the roll motion. The reason for this is given in Chapter 4.

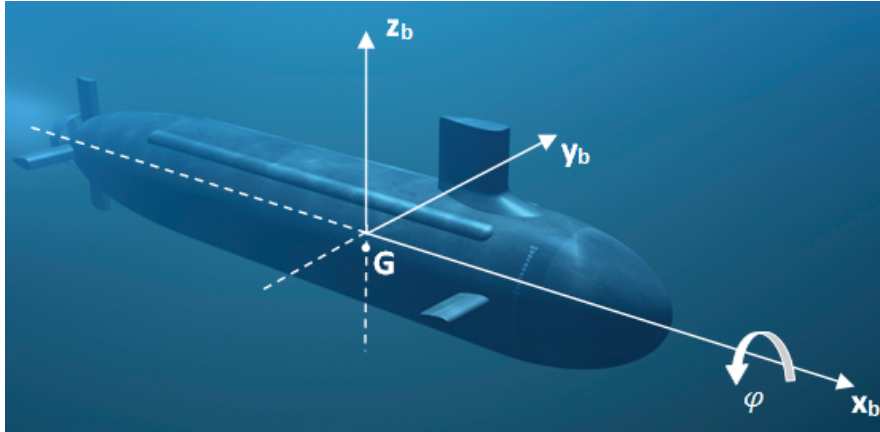


Figure 2-1: The ship bound coordinate system x_b, y_b, z_b .

Source: <http://www.army-suppliers.info/supplier/bruel-and-kjaer> (accessed on April 15, 2016)

2-1-2 Equation of motion

The rotation of a rigid body with a single degree of freedom around its center of gravity can be modelled as a mass-spring-damper system. The corresponding equation of motion is:

$$\sum M = I(\omega)\ddot{\varphi} + B(\omega, \dot{\varphi})\dot{\varphi} + C\varphi \quad (2-1)$$

In which:

- $\sum M$ = the sum of all external moments acting on the body
- I = the mass moment of inertia
- B = the damping term
- C = the spring term
- φ = the roll angle
- $\dot{\varphi}$ = the roll velocity
- $\ddot{\varphi}$ = the roll acceleration
- ω = the roll frequency

The mass moment of inertia consists of two parts:

$$I = I_{xx} + I_{\varphi\varphi} \quad (2-2)$$

I_{xx} is the mass moment of inertia of the body itself. It is a physical property of the body and independent of frequency or amplitude of the roll motion. When the body is (partially) submerged, such as a ship, the surrounding water is accelerated by the motion of the body. This causes an increase of the total moment. The added mass moment of inertia, $I_{\varphi\varphi}$, represents the additional moment acting on the submarine, which is in phase with the acceleration. The damping term contains all moments acting on the hull that are out of phase with the roll motion. The spring term is the static stability of the ship.

2-2 Non-linear roll damping

The roll damping of ships is a widely investigated subject. Some of the first work in the field of roll damping has been performed by Froude in 1861² and the research continues to this day. Despite the significant amount of publications over the past two hundred years, the roll damping cannot yet be predicted accurately for every ship type in every circumstance. The problematic prediction of roll damping is caused by the non-linearity due to the viscous nature of the roll damping and the strong influence of forward speed on the damping (as stated by Himeno (1981), Chakrabarti (2001) and Falzarano et al. (2015), amongst others). The current standard work on the prediction of roll damping is by Himeno (1981).

Himeno expands the damping term of Eq. (2-1) in a series of $\dot{\varphi}$:

$$B(\omega, \dot{\varphi}) = B_1\dot{\varphi} + B_2\dot{\varphi}|\dot{\varphi}| + B_3\dot{\varphi}^2 + \dots \quad (2-3)$$

In which:

$$\begin{aligned} B_1, B_2, B_3 &= \text{damping coefficients} \\ \dot{\varphi} &= \text{the roll velocity} \end{aligned}$$

The coefficients B_1 , B_2 and B_3 from Eq. (2-3) may be dependent on the roll amplitude and the roll frequency. As such, they can be taken as constants for a given steady-state roll motion.

Himeno (1981) linearises Eq. (2-3). The linearised damping coefficient is called the equivalent damping. The equivalent damping depends on the amplitude and the frequency of the motion:

$$B_e\dot{\varphi} = B(\omega, \dot{\varphi}) \quad (2-4)$$

In which :

$$B_e = \text{the equivalent damping}$$

Himeno describes several methods to express the equivalent damping in terms of the non linear damping coefficients. These will not be treated here, the reader is referred to Himeno (1981). Interesting for this research however, is the assumption that the equivalent damping is a linear composition of several damping components.

2-3 Damping components

Himeno (1981) states that the roll damping of surface ships is composed of seven components, which can be superimposed to determine the total damping:

$$B_e = B_F + B_E + B_L + B_W + B_{BKN} + B_{BKH} + B_{BKW} \quad (2-5)$$

²The papers of Froude are bundled and have been republished: Froude (1955)

In which:

- B_e = the equivalent damping from Eq. (2-4)
- B_F = the damping coefficient due to skin friction
- B_E = the damping coefficient due to eddy shedding
- B_L = the damping coefficient due to the generation of lift by the hull
- B_W = the damping coefficient due to radiated waves
- B_{BKN} = the damping coefficient due to normal forces on the bilge keels
- B_{BKH} = the damping coefficient due to the change in the pressure distribution over the hull as a result of the bilge keels
- B_{BKW} = the damping coefficient due to radiated waves from the bilge keels

Schmitke (1978), amongst others, stresses that appendages to the hull contribute significantly to the roll damping and should thus be included in the determination of the roll damping. Note that damping due to appendages (other than bilge keels) is not included in the seven damping components of Eq. (2-5)! As such, the damping of these appendages should be added to the equivalent damping. For the investigated submarine hull, the appendages consist of the four aft rudders and - depending on the configuration - two bowplanes. The influence of these rudders on the roll damping is investigated in Chapter 3. Some submarines have sonar arrays protruding from the sides of the submarine. A quick calculation shows that the influence of these arrays can be neglected. See Appendix A.

For a rolling submarine, most of the components in Eq. (2-5) can be neglected. Due to the absence of bilge keels, the last three terms of Eq. (2-5) can be ignored. Furthermore, since the cross-section of the submarine is almost circular, it is assumed that the potential damping can be neglected. Also, since the hull has no sharp edges or knuckles, the damping due to the shedding of eddies and due to the generation of lift by the hull is negligible: there are no discontinuities from which eddies can be shed, nor is there a shape over which a pressure difference can develop to generate lift.

In the experiments that were performed as part of this research it was shown that indeed only very small waves were generated by the hull, thus supporting the above assumption that these damping components can be neglected. Finally, the only remaining component is the damping due to skin friction.

Skin friction component

Himeno (1981) cites Kato (1958) for an expression for the coefficient B_F . In the case of turbulent flow - which is assumed to be the case for a full scale ship - and in the absence of forward speed, the coefficient becomes:

$$B_{F0} = 0.787 \rho S r_e^2 \sqrt{\omega \nu} \left(1 + 0.00814 \left(\frac{r_e^2 \varphi_A^2 \omega}{\nu} \right)^{0.386} \right) \quad (2-6)$$

In which:

- ρ = the density of the water
- S = the wetted surface area
- r_e = the effective bilge radius
- ν = the kinematic viscosity of the water
- ω = the roll frequency
- φ_A = the roll amplitude

Himeno (1981) uses an approximation formula for the effective bilge radius. Kato (1958), whose work was used by Himeno, studied rotating cylinders and used the radius of these cylinders for r_e . One can assume the submarine hull to be nothing but bilge radius. Hence, the effective bilge radius is taken as the (known) radius of the submarine hull.

The skin friction coefficient changes when forward speed is present. A simple correction can be applied to get the damping coefficient with forward speed ((Tamiya and Komura, 1972), as cited by Himeno (1981)):

$$B_F = B_{F0} \left(1 + 4.1 \frac{U}{\omega L} \right) \quad (2-7)$$

In which:

- B_F = the damping coefficient due to skin friction at forward speed
- B_{F0} = the damping coefficient due to skin friction at zero forward speed
- U = the forward speed of the ship
- ω = the roll frequency
- L = the length of the ship

Damping through appendages

As mentioned in Chapter 2 and stressed by Froude in 1861¹ and Schmitke (1978), the appendages of a hull contribute significantly to the roll damping. In the case of a submarine, the appendages are by far the major component in the roll damping. This chapter will study the different physical phenomena that play a part in the generation of roll damping by the rudders. The knowledge gained from this study will then be used to develop a mathematical model to predict the roll damping.

The main assumption made throughout this chapter, and indeed the remainder of this thesis, is that the rudders of a submarine behave as if they were wings. A two-dimensional wing of uniform section shape is called an airfoil. Airfoils have been extensively studied and their behaviour is well understood. The behaviour of an airfoil can be adjusted to account for the three-dimensional flow effects experienced by a wing.

The chapter will start by defining the flow in which the rudders operate and by investigating the behaviour of airfoils when placed in a two-dimensional flow. The behaviour in a three-dimensional flow will be discussed next, followed by the discussion of other relevant conditions in which the rudders operate.

3-1 Flow definitions

The flow in which the rudder is placed is a combination of two different flows: the forward flow, which is a result of the forward speed of the submarine, and the transverse flow, which is caused by the rolling motion of the submarine. These flows are perpendicular to each other and have to be added to find the effective flow in which the rudder operates². Unless the effective flow coincides with the forward flow, i.e.: the transverse flow is zero, the effective flow will be at an angle of attack with the mean chord line of the rudder.

¹See the republished papers of Froude: (Froude, 1955).

²An interesting parallel can be drawn here with sailing yachts: The wind speed and wind direction that are experienced by the sails is a combination of the true wind and the forward velocity of the yacht. The vector sum of these two components is called apparent wind speed and is used to calculate the forces generated by the sail (Fossati, 2009).

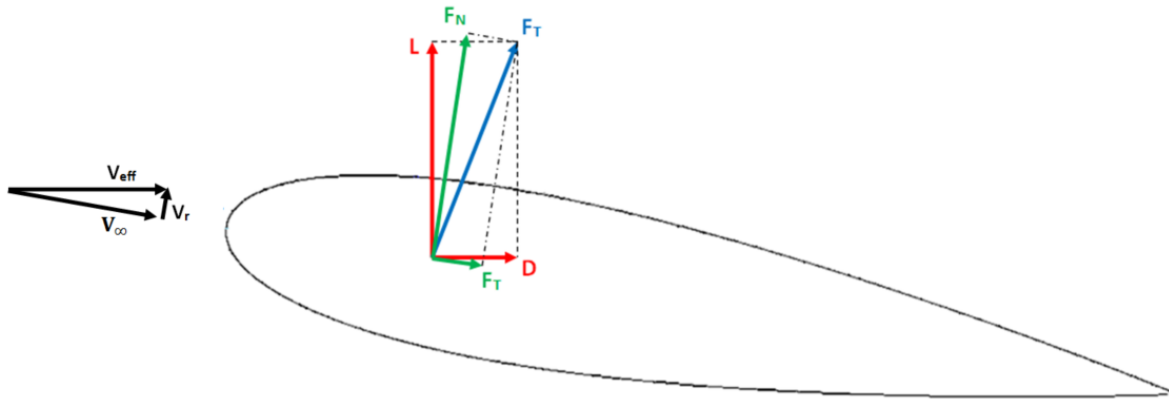


Figure 3-1: An airfoil with the directions of the different forces and flows acting on the rudder. In red the lift and drag forces. The black arrows to the left indicate the three different flows: the forward flow V_∞ , the transverse flow V_r , and the effective flow V_{eff} .

Due to the rolling motion of the submarine, the rudders operate in an unsteady flow: the transverse flow continuously changes in magnitude and direction, thus causing the angle of attack and the magnitude of the effective flow to change. A quasi-static approach is chosen, in which the flow is assumed to be steady for each moment in time for which the forces are calculated. Since the flow is continuously changing, a correction factor needs to be applied to account for unsteady effects. This factor is discussed in Section 3-5.

Lift and drag forces are defined as being normal and tangential to the undisturbed, effective flow. Undisturbed means that changes in flow direction because of upwash or downwash are not taken into account. These lift and drag forces are generated by a wing when it is placed at an angle of attack in a flow. Lift and drag forces can be combined to find the force normal to the wing. It is this force that is opposing the roll motion and is thus responsible for the damping generated by the wing. Figure 3-1 shows the direction of the different forces and velocities on a wing.

3-2 Rudder dimensions

The lift and drag forces of a rudder are dependent on the dimensions of the rudder, which are dependent on the rudder configuration. The span of the rudders is maximized within the bounding box around the hull. Breadth and draft of the hull are not to be exceeded, to prevent damage to the rudders when mooring the submarine or in a grounding event. Hence, the span is largest in the X-configuration. Figure 3-2 shows the two rudder configurations and the maximum rudder span allowed within the bounding box around the hull.

The bowplanes will always protrude outside the bounding box. To allow for mooring of the submarines, bowplanes are in general either retractable or folding. As a result, the span of the bowplanes is not limited by the maximum breadth of the submarine.

Table 3-1 gives some typical dimensions of the rudders. It is assumed that all four of the aft rudders have the same dimensions.

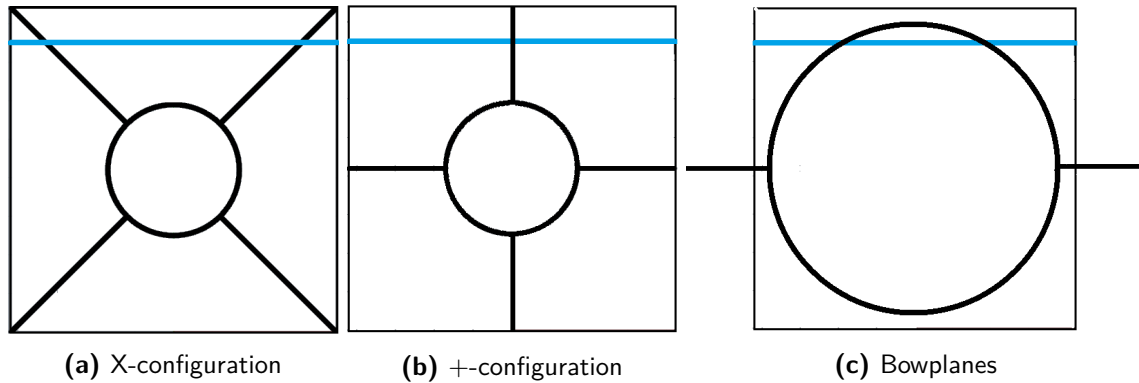


Figure 3-2: The two configurations of the aft rudders, shown with bounding box and the waterline when surfaced. The span of the rudders in X-configuration is clearly larger than in the cross-configuration. The bowplanes are shown too, with the bowplanes protruding outside of the bounding box.

The aspect ratio is an important geometrical parameter which is strongly related to ratio between the lift and drag developed by the wing. The geometric aspect ratio of a wing is defined as the ratio between the span and the chord of the wing:

$$AR = \frac{b}{c} \quad (3-1)$$

Since wings often have different chords at root and tip of the wing, the geometric aspect ratio is also often defined as the ratio between the projected surface and the span:

$$AR = \frac{b^2}{S_p} \quad (3-2)$$

In which:

- AR = the geometric aspect ratio
- b = the span of the wing
- c = the chord of the wing
- S_p = the planform area of the wing, i.e.: the area of the projection of the wing on a plane parallel to the wing

Besides the geometric aspect ratio, an effective aspect ratio exists. The effective aspect ratio is a correction on the geometric aspect ratio to account for changes in circulation around the wing. The effective aspect ratio is treated in more detail in Section 3-3-3.

3-3 Generation of lift

Thin airfoil theory is used for the calculation of lift for a specific airfoil or wing. Thin airfoil theory is developed in the period 1910-1920 by Ludwig Prandtl and his colleagues at Göttingen, Germany. Anderson (2011) gives a good overview of this theory and its applications. Hoerner (1975) gives many examples of lift generation in nearly every situation, supported by experimental data.

The lift produced by a wing is given by:

$$L = C_L \frac{1}{2} \rho V_{\text{eff}}^2 S_p \quad (3-3)$$

In which:

- L = the lift force
- C_L = the lift coefficient
- ρ = the density of the fluid in which the wing is submerged
- V_{eff} = the velocity of the effective flow
- S_p = the planform area of the wing

The lift coefficient depends on the flow over the wing. The flow is different for two- and three-dimensional flow conditions. Other effects, such as the vicinity of the free surface or the proximity and shape of the submarine hull further alter the flow conditions and thus the lift coefficient. In the remainder of this section, each of these conditions is studied.

3-3-1 Two-dimensional flow

For an airfoil at small to moderate angles of attack, the lift coefficient is given by (Anderson, 2011):

$$C_L = 2\pi\alpha \quad (3-4)$$

In which:

- α = the angle of attack in radians

This linear relation between the lift coefficient and the angle of attack remains valid as long as the flow is attached to the airfoil. For larger angles of attack, the flow separates from the low pressure side. With growing separation, the lift coefficient diminishes and the airfoil is said to be stalled. More on this in Section 3-3-7.

3-3-2 Three-dimensional flow

The flow around a three-dimensional wing is quite different from the flow around a two-dimensional airfoil. In the three-dimensional case, the flow over the wing is influenced by the

Table 3-1: Main dimensions of the rudders

		X-configuration	+ -configuration	Bowplanes
Span	[m]	4.3	2.5	2.7
Chord	[m]	2.9	2.9	2.5
Area	[m ²]	13	8.0	6.6
Geometric aspect ratio	[-]	1.42	0.82	1.10
Effective aspect ratio	[-]	2.20	1.45	2.20 [†]
Profile shape		NACA 0018	NACA 0018	NACA 0018

[†] Eq. (3-6) would result in an effective aspect ratio of 2.3, which is more than twice the geometric aspect ratio. Hoerner (1975) states that the maximum effect of a single end plate is the doubling of the geometric aspect ratio. Hence the effective aspect ratio of the bow rudders is taken as the double of the geometric aspect ratio.



Figure 3-3: The tip vortex from the starboard bowplane is visible as a depression in the water surface behind the bowplane, within the red ellipse.

finite dimensions of the wing. The pressure difference between the upper and lower side of the wing decreases when approaching the wing tip, since there is a flow from the high pressure side to the low pressure side over the tip. Due to this ‘leaking’, the wing generates less lift. The effect of the wing tips on the lift generation is stronger for wings with a smaller span, since the area influenced by the tips will be relatively larger. The flow from the high to low pressure side of the wing creates a vortex behind the wing tip. This vortex is seen during the experiments when the rudder tip was close to the water surface, see Figure 3-3.

Larsson and Raven (2010) give the following equation for the lift coefficient of a three-dimensional wing with an elliptical load distribution:

$$C_L = \frac{2\pi}{1 + \frac{2}{AR_e}} \alpha \quad (3-5)$$

In which:

- C_L = the lift coefficient
- AR_e = the effective aspect ratio
- α = the angle of attack in radians

Note that for large aspect ratios, when the three-dimensional wing approaches a two-dimensional situation, Eq. (3-5) approaches Eq. (3-4). The assumption of elliptic loading is generally valid for most rudders. The effective aspect ratio takes the actual flow (and thus the load distribution) around the wing into account. The effective aspect ratio will be treated somewhat more extensively in Section 3-3-3.

3-3-3 Hull effects

The hull has a major influence on the lift generation of the rudder: it changes the circulation around the rudder, which influences the lift generation.

Effective aspect ratio

When a wing is attached to a large flat plate perpendicular to the wing, the pressure distribution over the wing changes. The plate prevents the disadvantageous flow that is ‘leaking’ from the high to the low pressure side of the wing, thus changing the pressure distribution over the wing: the pressure is now distributed as if the span was twice as large. This effect is accounted for in the effective aspect ratio. Since the pressure distribution equals the pressure distribution of a wing of twice the span, the effective aspect ratio is twice as large as the geometrical aspect ratio.

In the case of a submarine, the rudder is attached to the hull which acts as an endplate to the rudder. The hull is not flat, but curved, which is a less effective shape for an endplate. Hoerner (1975) gives the effective aspect ratio for a wing attached to a circular cylinder:

$$AR_e = AR \left(1 + \frac{d}{b} \right) \quad (3-6)$$

In which:

- AR_e = the effective aspect ratio
- AR = the geometric aspect ratio
- d = the diameter of the cylinder
- b = the span of the wing taken to the center of the cylinder

Based on Eq. (3-6), the effective aspect ratio is about 1.8 times the geometric aspect ratio, for the submarine studied in this research.

3-3-4 Vicinity of the free surface

The lift coefficient of Eq. (3-5) assumes that the wing is deeply submerged. Deeply submerged means that the wing is not influenced by the free surface of the water. In the case of a surfaced submarine, most of the rudders operate close to the free surface or even pierce through the free surface.

Take a deeply submerged wing with its circulation. Upon bringing this wing to the free surface, which is a surface of constant pressure, the circulation has to change to maintain the constant pressure condition. Assume a second, but imaginary, circulation of equal strength, direction and distance above the free surface. Since these circulations cancel each other at the free surface, the constant pressure condition is maintained. The combined (virtual) flow field of these two circulations now equals the flow field experienced by the rudder. In this flow field, the lift coefficient is reduced, due to the reduction in circulation.

The flow field of the wing now resembles the flow field of the lower plane of a biplane. Hoerner (1975) uses this similarity and gives the following equations for the lift coefficient of a horizontal hydrofoil:

$$\frac{d\alpha^o}{dC_L} = K_2 \left(10 + \frac{10}{AR_e^2} \right) + K_i \frac{20}{AR_e} \quad (3-7)$$

$$K_2 = \frac{16 \left(\frac{h}{c} \right)^2 + 2}{16 \left(\frac{h}{c} \right)^2 + 1} \quad (3-8)$$

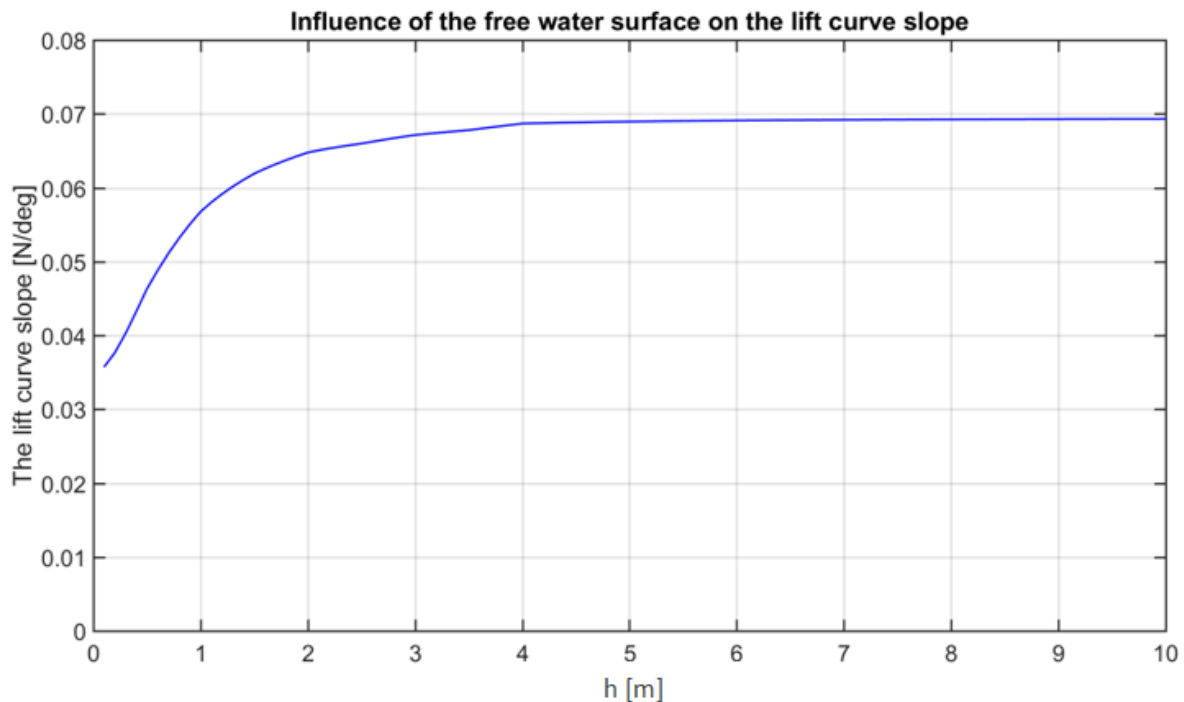


Figure 3-4: The influence of the submergence (h) on the lift curve slope of a horizontal wing. The wing has a span of 5 m, a chord of 2 m and an effective aspect ratio of twice the geometric aspect ratio.

In which:

α° = the angle of attack in degrees

C_L = the lift coefficient

AR_e = the effective aspect ratio

K_i = a value depending on the ratio of submergence and span that can be read from Figure 3-5

h = the submergence of the wing at a point at half the span of the wing

c = the chord

The effect of the free surface on the lift curve slope can be significant. The lift curve slope can be up to half the value of the lift curve slope for a deeply submerged wing. To show this effect, a sample calculation has been performed for a rudder at different submergence depths. This sample wing has a span of five meters and a chord of 2 meters. The effective aspect ratio is taken to be twice the geometric aspect ratio. The submergence is varied from 0.1 m to 10 m. The values of the lift curve slope are calculated using Eq. (3-7) and Eq. (3-8) and are shown in Figure 3-4. It is clear that for shallowly submerged wings the effect of the free surface is significant.

Based on the submergence to chord and the submergence to span ratios from Eq. (3-8) and Figure 3-5, it is taken that the lower rudder of the +-configuration and the lower two rudders of the X-configuration can be treated as deeply submerged rudders. All these rudders have a submergence greater than 4.5 m.

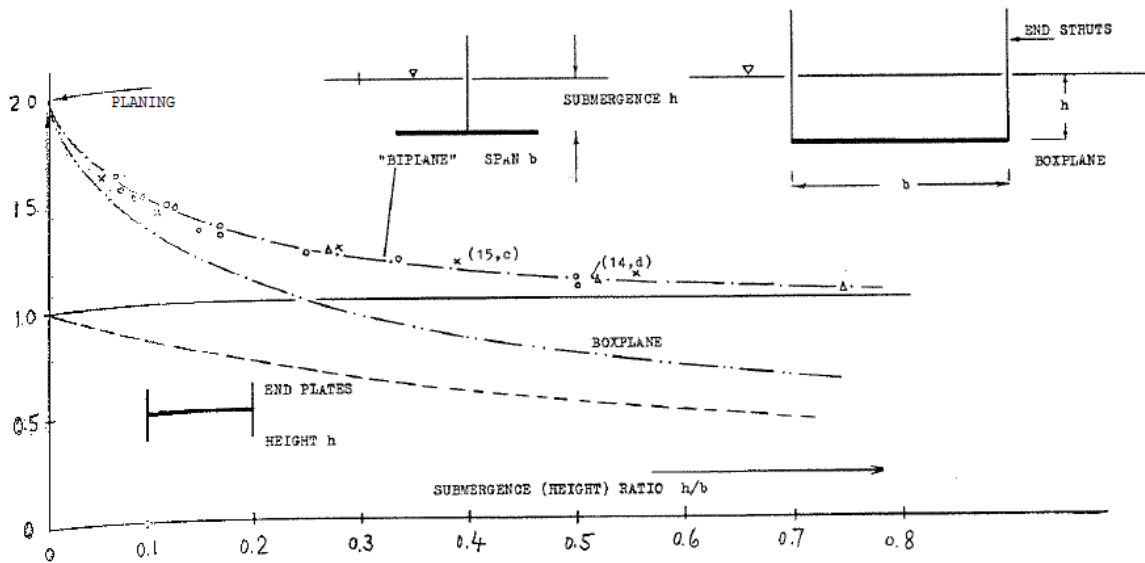


Figure 3-5: The value of K_z as a function of the submergence ratio. Reproduced from Hoerner (1975)

The surface piercing rudders in the X- and +-configurations can be treated as a surface piercing strut (Hoerner, 1975):

$$\frac{d\alpha^\circ}{dC_L} = 11 + \frac{11}{AR_e^2} + \frac{26}{AR_e} \quad (3-9)$$

In which:

- α° = the angle of attack in degrees
- C_L = the lift coefficient
- AR_e = the effective aspect ratio

3-3-5 Ventilation

Since the rudders operate close to the surface, or even pierce through the water surface, ventilation may occur. When ventilation occurs, the flow around the rudder is disturbed as an air-filled pocket is created on the low pressure side. The pressure difference drops and the lift generated by the rudder decreases sharply. Breslin and Skalak (1959) studied the ventilation of surface piercing struts. Part of this study was the investigation of ventilation inception on a NACA 4412 and a circular arc strut. Breslin and Skalak found that there is a speed at which ventilation inception starts and a far lower speed at which a ventilated cavity closes. The ventilation inception is dependent on the angle of attack of the strut with the effective flow.

The inception velocity and the angle of attack determine if and how ventilation starts: as a result of the tip vortex or as a result of leading edge separation. The results of Breslin and Skalak are shown in Figure 3-6. The rudders of the submarine investigated do not have one of the profiles shown in Figure 3-6. The sharp edged circular arc profile will suffer from leading edge separation before the round nosed NACA 0018 separates. The NACA 4412 has a smaller

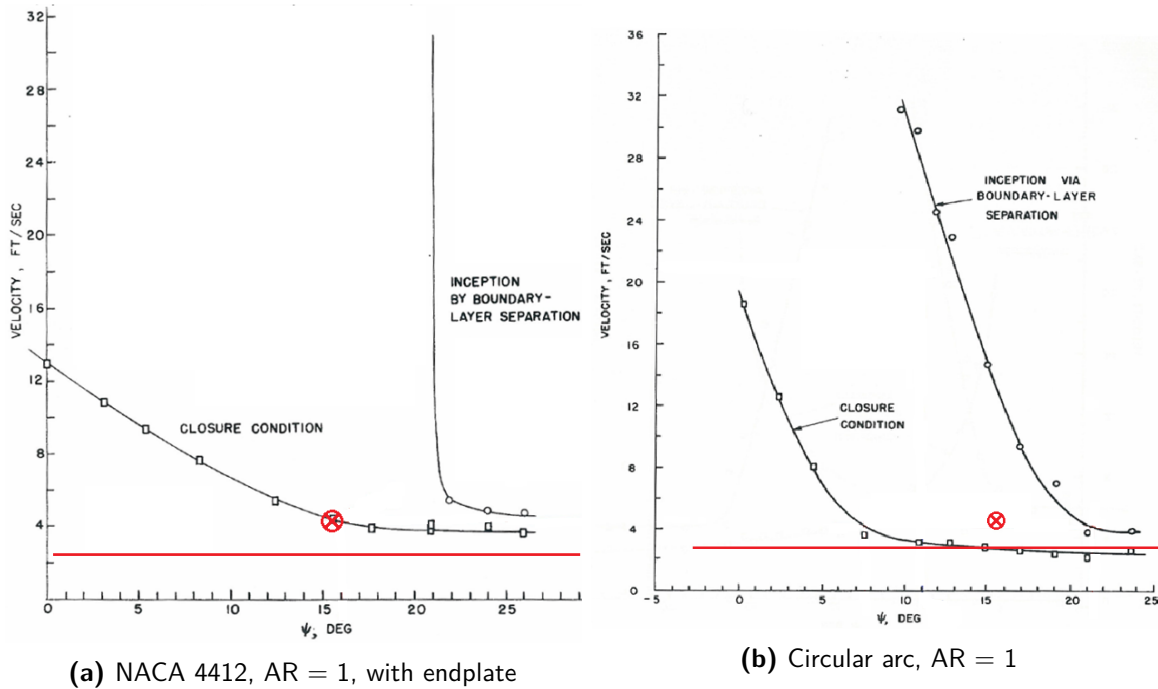


Figure 3-6: Two surface piercing struts with ventilation inception and ventilation closure lines. \otimes indicates the condition of maximum effective speed, while the red line indicates the speed at which the maximum angle of attack occurs. The maximum angle of attack (29 deg) lies outside the range of the graphs. Reproduced from Breslin and Skalak (1959)

nose radius and thickness as the NACA 0018 used in the submarine and is thus expected to suffer from separation earlier. Hence, the figures are on the conservative side.

Based on these figures, the following conclusion can be drawn: on the model scale that will be used in the experiment ventilation will not occur. The maximum velocities at the surface piercing struts and the angles of attack are too low for ventilation inception. However, it should be noted that these values assume calm, undisturbed water. Even small disturbances in front of the rudder may trip the creation of a ventilated cavity. If ventilation occurs, it will be due to these disturbances.

In the experiments that are part of this research, no ventilation has been observed. In a few experiments, some air bubbles were seen attached to the top part of the rudder. No reduction in the normal force on the rudder was however measured. Therefore it is concluded that, in accordance with the results in Figure 3-6, no ventilation has occurred.

3-3-6 Variation of the angle of attack

In the previous sections, it was assumed that the angle of attack was a constant value for the wing. However, due to the rolling motion of the wing and the influence of the boundary layer, this is not the case. This section discusses the variation in the angle of attack due to these two factors.

Effect of the roll motion

The angle of attack is defined by the ratio between the forward flow and the transverse flow:

$$\alpha = \tan^{-1} \left(\frac{V_r}{V_\infty} \right) \quad (3-10)$$

In which:

- V_r = the transverse flow velocity
- V_∞ = the forward flow velocity

The transverse flow velocity is a function of the roll frequency, roll amplitude and the spanwise position:

$$V_r = \dot{\varphi} r \quad (3-11)$$

$$\dot{\varphi} = -\varphi_A \omega \sin(\omega t) \quad (3-12)$$

In which:

- r = the radial distance from the axis of rotation to the position on the wing at which the angle of attack is to be determined
- φ_A = the amplitude of the roll motion
- ω = the frequency of the roll motion
- t = the moment in time at which the angle of attack is to be determined

Eq. (3-11) and Eq. (3-12) readily show that the transverse flow velocity oscillates between $+\varphi_A \omega r$ and $-\varphi_A \omega r$. Hence, the angle of attack oscillates in time. Also, Eq. (3-11) shows a linear relation between the spanwise position of a point and its corresponding transverse velocity. The angle of attack increases over the span of the wing.

Effect of the boundary layer

Due to the forward velocity of the submarine, a boundary layer develops. Given the large Reynolds number of a sailing submarine, the flow can safely be considered to be turbulent³. Following Hoerner (1965), it is assumed that the boundary layer over the forward part of the hull, which has a favourable pressure gradient, develops as the boundary layer over a flat plate:

$$\frac{\delta}{x} \approx \frac{0.16}{Re_x^{1/7}} \quad (3-13)$$

In which:

- δ = the thickness of the boundary layer
- x = the relevant distance, measured from the bow of the submarine
- Re_x = the Reynolds number based on length x

Over the aft part of the hull, which has an adverse pressure gradient, the growth of the boundary layer is much stronger. Hoerner states that the annular area of the boundary layer

³Transition from laminar to turbulent flow does not happen at a fixed Reynolds number. The turbulence level of the undisturbed flow in front of the ship and the roughness of the hull are just two parameters that influence the transition to turbulent flow. However, White (2009) states that for a typical commercial surface, transition occurs at $Re = 5 \cdot 10^5$. A value that, at 6 kn forward speed, is reached after just 20 cm hull length.

at the maximum diameter is transformed to a circle of equal area at the pointed end of the body. The additional increase in boundary layer thickness is given by:

$$\delta' = 0.02 \frac{d}{d_x} x' \quad (3-14)$$

In which:

- δ' = the increase in boundary layer thickness
- d = the maximum diameter of the hull
- d_x = the diameter of the hull at position x
- x' = the distance from the point of maximum diameter

For the submarine considered, the boundary layer has a thickness of 1.85 m at the aft rudders. At the bowplanes however, the boundary layer is only 9 cm thick.

The velocity is not uniform inside the boundary layer. Directly adjacent to the hull the velocity is zero. At the edge of the boundary layer, the velocity equals the free stream velocity. The velocity distribution for a turbulent boundary layer depends on the local pressure gradient. Assuming that the Reynolds number is sufficiently large to prevent boundary layer separation and taking flat plate flow as a first estimate, the velocity profile in the boundary layer is given by (White, 2009):

$$\frac{u}{V_\infty} = \left(\frac{y}{\delta} \right)^{1/7} \quad (3-15)$$

In which:

- u = the flow velocity at distance y from the hull
- V_∞ = the free stream velocity
- y = the distance measured normal to the hull into the boundary layer
- δ = the boundary layer thickness

Due to the adverse pressure gradient which exists over the aft part of the hull, the actual velocity profile will differ from the one mentioned above. The velocity close to the wall will be smaller.

The result of the boundary layer is that the local velocities will be lower. As a result, the local angle of attack increases. This effect is stronger when approaching the root of the rudder. The ruddertip operates outside of the boundary layer and is therefore not affected by the boundary layer.

Combined effect

The influence of the spanwise position on the local lift force is investigated. To account for the varying angle of attack and transverse velocity, a strip approach is used in calculating the lift force generated by a wing on a strip of area dS . Calculations on a strip are performed using the angle of attack and the effective velocity at half the width of the strip:

$$dL = \frac{1}{2} \rho C_L V_{\text{eff}}^2 dS_p \quad (3-16)$$

$$V_{\text{eff}} = \sqrt{V_f^2 + V_r^2} \quad (3-17)$$

$$V_f = \begin{cases} V_\infty & \text{outside the boundary layer} \\ u & \text{inside the boundary layer} \end{cases} \quad (3-18)$$

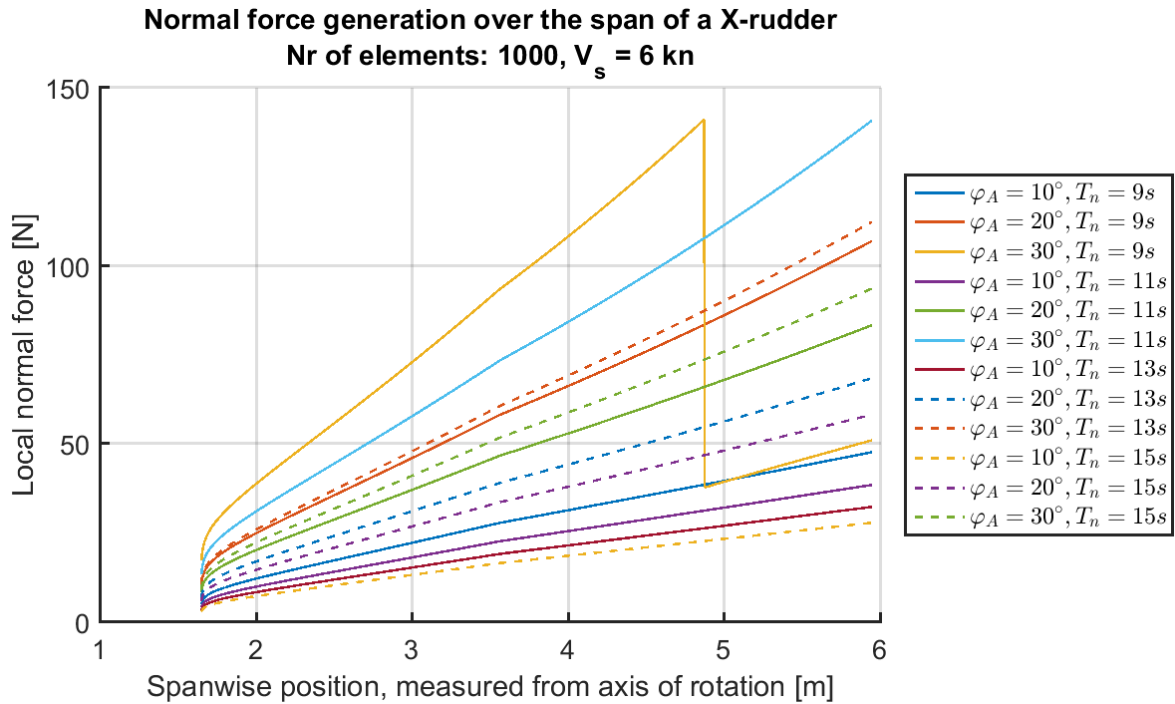


Figure 3-7: Calculation of the maximum normal force generated by a X-rudder using strips for each combination of roll amplitude and roll frequency tested during the experiments. Forward velocity of 6 kn. Notice how in the most heavily loaded case the rudder tip stalls and the normal force drops due to the loss of lift.

In which:

- dL = the local lift force generated on the strip
- ρ = the fluid density
- C_L = the local lift coefficient
- V_∞ = the undisturbed flow velocity
- V_r = the local transverse flow velocity
- u = the local longitudinal flow velocity in the boundary layer as given by Eq. (3-15)
- dS_p = the projected area of the strip

The results for a X-rudder are shown in Figure 3-7. Please note that this figure shows the normal force generated by the rudder, which mainly consists of the lift force, but also includes drag forces. In this case the rather large number of a 1000 strips are used to calculate the lift force. The figure clearly shows that for the most extreme case, the outer part of the rudder stalls and the local normal force drops sharply. This phenomenon cannot be captured using only a single strip.

3-3-7 High angles of attack and stall

As a result of the variation in flow velocity over the span of the wing, as mentioned in Section 3-3-6, the angle of attack varies between the tip and the root of the wing. The angle of attack is

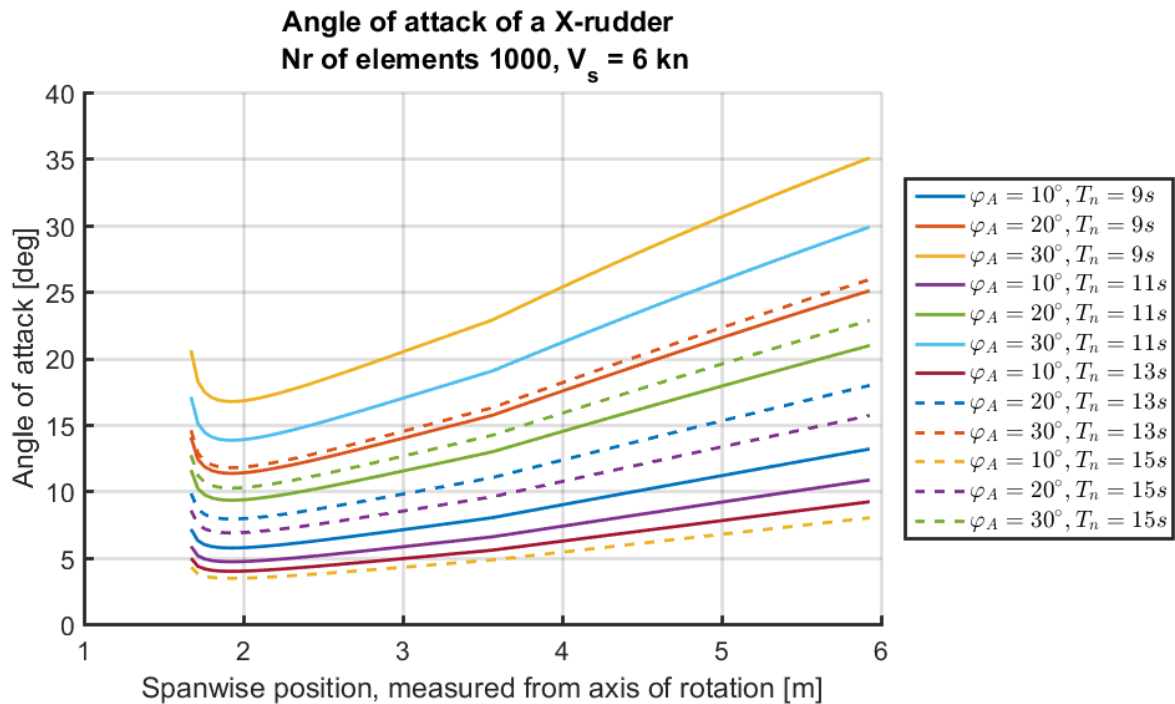


Figure 3-8: The variation of the angle of attack over the span of a X-rudder. The angle of attack increases sharply at the root of the rudder due to the boundary layer. The angles of attack have been calculated for an undisturbed free stream velocity of 6 kn. At the maximum forward speed of 12 kn, the angles of attack are all much smaller.

largest at the very root of the wing, where due to the boundary layer the longitudinal flow velocity approaches zero and at the tip, where the transverse velocity is large. See Figure 3-8.

Given the high angle of attack, it is expected that the wing will (partially) stall. At stall, the lift coefficient will drop significantly due to the detachment of the flow over the low pressure side of the rudder. Hence, Eq. (3-5) is no longer valid.

Sheldahl and Klimas (1981) investigated the NACA0018 foil, which is the foil section used for the aft rudders, up to angles of attack of 180 degrees. The Reynolds numbers at which Sheldahl and Klimas investigated the foil ($Re = 5 \cdot 10^6$) are close to the Reynolds number of the actual rudders ($Re = 7.45 \cdot 10^6$). The data of Sheldahl and Klimas is only applicable to airfoils. In Section 3-3 it was shown that a correction factor can be applied to the two-dimensional lift coefficient to obtain the three-dimensional lift coefficient (see Eq. (3-5)). It is assumed that this correction is also applicable to the two-dimensional lift coefficient in the post stall regime. With the thus obtained lift coefficients, it is possible to calculate the lift force both before and after stalling of the rudders. The lift coefficients have been included in Appendix C.

Change in stall angle

The stall angle is dependent on the effective aspect ratio of the wing. Molland and Turnock (2007) give the relation between the aspect ratio of a wing and the corresponding stall angle.

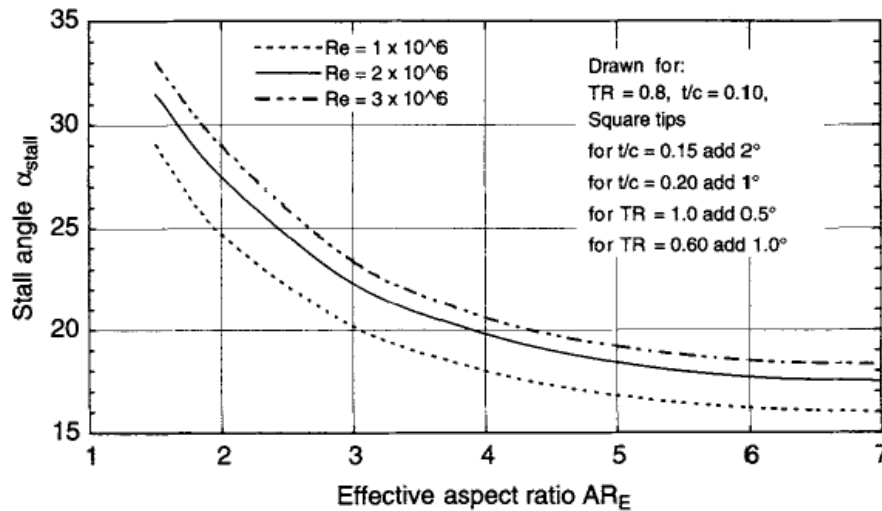


Figure 3-9: The relation between stall angle and effective aspect ratio. Reproduced from Molland and Turnock (2007)

Figure 3-9 shows the significant delay for stall when the aspect ratio is reduced. The delay in stall angle can be explained by the relative increase in chord of the wing. When the chord is increased, the flow regains the possibility to reattach itself to the wing, thus postponing the full-out stall of the wing. The linear part of the lift curve slope from Sheldahl and Klimas (1981) is extended to the stall angle according to Figure 3-9. For angles of attack greater than the stall angle, the lift curve is assumed to drop to the values given by Sheldahl and Klimas (1981).

3-4 Drag

The drag of a wing does also contribute to the normal force acting on the wing and should thus be included in the calculations. The drag of a wing consists of two main components:

1. The profile drag
2. The induced drag

The profile drag is the drag that a two-dimensional body experiences when placed in a fluid flow. For a streamlined body, such as a wing, at a low angle of attack, this drag is very low. If the angle of attack is increased, the drag increases too. At the extreme situation of 90 degrees angle of attack, the wing behaves as if it were a flat plate perpendicular to the flow. Following Hoerner (1965), the profile drag is modelled by the following equation, which is valid for a three-dimensional wing:

$$C_{D_0} = 1.2 \sin^3 \alpha \quad (3-19)$$

In which:

- C_{D_0} = the profile drag coefficient
- 1.2 = the drag of a flat plate placed perpendicular to the flow, as stated by Hoerner (1965) or White (2009)
- α = the angle of attack

The induced drag is a drag component that is only experienced by a three-dimensional wing. It is related to the circulation around the wing and is thus directly linked to the lift that is being generated. Assuming an elliptical circulation over the rudder, the following well known equation is used to determine the induced drag, as can be found in Hoerner (1965) and Anderson (2011) and others:

$$C_{D_i} = \frac{C_L^2}{\pi AR_e} \quad (3-20)$$

In which:

- C_{D_i} = the induced drag coefficient
- C_L = the lift coefficient
- AR_e = the effective aspect ratio

In the case that the circulation is not elliptical, as is the case for the rudders of a submarine, the induced drag will increase while the lift drops. As a first estimate of the lift and drag forces experienced by a wing, an elliptical distribution of the circulation is however assumed.

The total drag coefficient is the sum of the profile drag and the induced drag:

$$C_D = C_{D_0} + C_{D_i} \quad (3-21)$$

Since the induced drag is dependent on the local lift coefficient, the drag is calculated using the same strip wise approach as applied to the lift calculation: a local drag coefficient is determined for each strip over the span of the wing. With these local drag coefficients and the local effective velocity, the local drag is calculated. The summation of the local drag forces over the wing results in the total drag force:

$$dD = \frac{1}{2} \rho V_{\text{eff}}^2 C_D dS_p \quad (3-22)$$

$$D = \sum dD \quad (3-23)$$

In which:

- dD = the local drag force
- ρ = the fluid density
- V_{eff} = the local effective fluid velocity
- C_D = the local drag coefficient
- dS_p = the projected strip area over which the calculation is performed
- D = the total drag force

3-5 Correction for unsteady flow

In the previous sections it is assumed that the wing is positioned in a (quasi-)static flow condition. For a rolling submarine this is not the case and with continuously changing flow conditions, the lift generated by the rudder will be different from the (quasi-)static case.

The quasi-static approach incorporates the change in wetted area and aspect ratio of the top rudders for each time step. It also takes the change in effective velocity and angle of attack into account. It does not, and cannot, incorporate the effect of the unsteady wake and the acceleration of the fluid.

The oscillating motion of the wing accelerates the surrounding water, which influences the pressure distribution and hence the circulation around the wing. In addition, the wake behind the wing is unsteady: the strength of the shed vortices from the wing is dependent on the circulation. With the circulation changing over the oscillation, the strength of the shed vortices changes too and the induced velocity on the wing by the vorticity in the wake is not constant.

Ogilvie (1958) calculated the effect of unsteadiness on the forces generated by a two-dimensional hydrofoil. Assuming that the correction for unsteadiness for a three-dimensional hydrofoil is equal to the correction for a two-dimensional hydrofoil, Ogilvie derives a correction factor for the effects of unsteady vorticity in the wake and the acceleration of mass by the hydrofoil. He uses a reduced frequency to characterize the oscillatory motion. The reduced frequency relates the frequency of the oscillation to the time it takes for a vortex to develop over the chord of the rudder:

$$\omega' = \frac{\nu c}{2V} \quad (3-24)$$

In which:

- ω' = the reduced frequency
- c = the chord
- ν = the oscillatory frequency of the motion
- V = the forward speed of the wing

The resulting correction factors that have to be applied to the quasi-static force calculations can be read from the graph shown in Figure 3-10.

Applying this theory to the oscillating rudders of a submarine results in significant reductions of the lift and drag forces.

3-6 Normal force

The normal force can now be calculated by combining the lift and drag forces and the correction for the oscillatory lift generation:

$$N = (L \cos \alpha + D \sin \alpha) \cdot K \quad (3-25)$$

In which:

- N = the normal force
- L = the lift force
- D = the drag force
- K = the correction factor for the oscillatory lift generation

It is this normal force that causes the roll damping. It is also the force that has been measured in the experimental phase of this research.

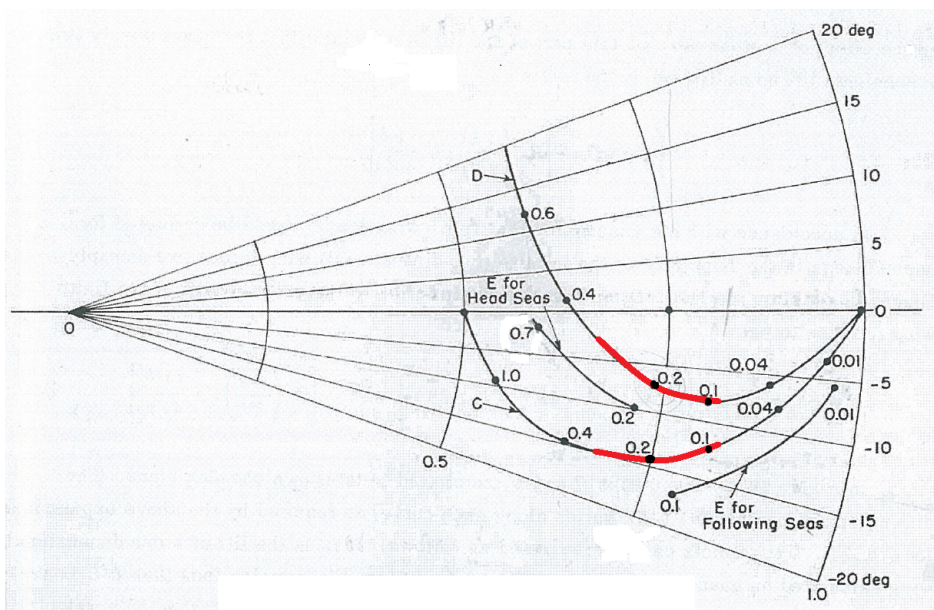


Figure 3-10: The reduction of the 2D-liftcoefficient by the effect of unsteady vorticity in the wake and the acceleration of mass by a hydrofoil. Line 'C' is the correction factor if only the unsteady vorticity in the wake is taken into account. Line 'D' gives the correction factor for the combined effect of an unsteady wake and the acceleration of mass by the hydrofoil. The radial distance indicates the reduction factor, while the angle gives the phase shift associated with the unsteady lift. The values along the line are dimensionless frequencies ω' . The range relevant for the experiments performed is marked in red. Reproduced from Ogilvie (1958).

3-7 Mathematical model

Using the theory described in this chapter, a mathematical model has been created to predict the roll damping of a submarine. In the basis, the model uses the known geometry of the submarine and a given roll amplitude and roll frequency to calculate the normal force acting on the rudders of the submarine. From this normal force it is just a small step to the corresponding damping moment.

Experimental set-up

The mathematical model that has been developed is based on the theory that is described in Chapter 3. To validate this model, a rather large number of experiments have been carried out. This chapter describes the set-up of the experiments and the way in which the measurements have been carried out.

4-1 Measuring the roll damping

The experiments were carried out at the large towing tank of the Delft University of Technology. The dimensions of the towing tank are shown in Table 4-1. To validate the model, the roll damping of the model submarine has to be experimentally determined.

4-1-1 Roll decay test

A common way to determine the roll damping of a ship or model is to perform a roll decay test. In such a test, the model is given an initial roll angle and then released. The roll angle is measured as the model oscillates. The rate at which the roll amplitude decreases with each oscillation can be used to calculate the roll damping. The disadvantage of roll decay tests is that the amplitude of the oscillation is continuously decreasing. Since the damping is dependent on the roll amplitude, the damping will not be constant over the length of the decay test. Also, the roll frequency in a roll decay test will be equal to the eigenfrequency of the model. It is thus not possible to measure the influence of other frequencies on the roll damping. For these reasons, no roll decay tests have been performed.

Table 4-1: The dimensions of the large towing tank of Delft University of Technology

Length	142	[m]
Width	4.22	[m]
Depth	2.50	[m]
Maximum carriage velocity	8.00	[m/s]

4-1-2 Oscillating moment

A second way of measuring the roll damping is by applying a known, oscillating, moment to the model. By measuring the roll motion and with a known mass moment of inertia and stability of the model, the damping can be determined by solving Eq. (2-1). This is an attractive and relatively easy way of measuring the roll damping.

The moment can be applied by means of a couple of contra-rotating gyroscopes, mounted inside the model. By rotating the spinning gyroscopes, a moment is created that causes the model to roll. The disadvantage of this method is that the size of the moment is dependent on the frequency at which the gyroscopes are rotated: for low frequencies, the moment will be low. The available roll moment excitor at the towing tank of the Delft University of Technology is however too small to create the large moments needed for the large roll angles. Hence, no exciting moment has been used to determine the roll damping in these experiments.

4-1-3 Forced oscillation

An alternative way of measuring the roll damping is to force the roll motion on the model. By measuring the moment acting on the model, the damping can be determined by solving Eq. (2-1), if the mass moment of inertia and the stability of the model are known. With the total moment that is acting on the hull being measured, there is a second way of calculating the roll damping. The phase difference between the moment and the roll angle gives the damping moment: The total moment is the combination of the moments due to inertia, damping and stability. The moments due to inertia and stability are in phase with the motion, while the moment due to damping is out of phase with the motion (see Eq. (2-1)). By determining the out of phase part of the measured total moment, the damping moment is found.

The advantage of using forced oscillation tests is that any motion can be forced on the model. The motion is not restricted to the eigenfrequency of the model and the oscillation can be maintained at the same condition for as long as is needed. This gives flexibility in the measurements and the possibility to investigate the influence of the roll frequency on the roll damping. For these reasons, forced oscillation tests are the preferred way of testing in this research.

4-1-4 Forces to be measured

A number of forces are to be measured to be able to determine the roll damping of the model. As stated in Section 4-1-3, the total moment acting on the model has to be measured. In addition to this moment, the normal force on the rudders of the model is measured. By measuring both the normal force on the rudders and the total moment on the entire model, the influence of the hull on the damping moment can be determined. It also provides a second method of determining the roll damping, in accordance with the conclusion of Chapter 2, that the rudders cause nearly all of the roll damping.

Finally, the roll angle of the model is measured. By measuring the actual roll angle, it is possible to check the actual motion with the desired motion.

4-2 Properties of the model

A model of scale 24 of a representative diesel-electric submarine has been created for the purpose of the experiments. Table 4-2 gives the relevant main dimensions of the model. A photo of the model is shown in Figure 4-1.

Some full scale properties of a submarine have been left out in the model. No sonar flank arrays have been included in the model, nor can water enter the space between the inner and outer hull (the casing). Initial studies have shown that these properties have a negligible effect on the roll motion of the submarine. Therefore they are left out. The studies proving this point can be found in Appendix A and Appendix B.

The model is made of a polyester hull, stiffened with wooden bulkheads. The stern of the hull and the top half of the hull are detachable, to allow access to the inside of the model. The stern is bolted to the hull. By bolting the stern in different positions, the stern can be rotated and the rudders can thus be mounted in +- or X-configuration. Rudders can be mounted at fixed positions at the bow and stern of the model. Force sensors to measure the rudder normal forces are mounted inside the hull. The rudder shafts are passed through openings in the hull to the force sensors. To prevent water from entering the hull, latex seals are used. For the bow rudders, the latex seals were later on replaced by grease to prevent the water from entering. The replacement was necessary because the latex seals were bearing part of the load, thus causing the sensor to measure too low a loading on the rudder. This problem will be treated in more detail in Chapter 5. Figure 4-2 shows the way in which the rudder shafts are passed through the openings in the hull.

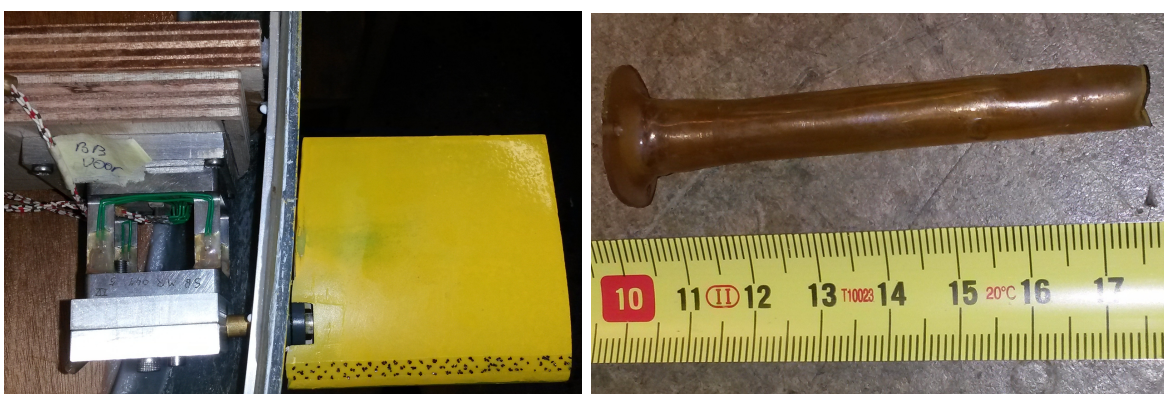
Lead bricks are fixed in the model to provide the proper ballasting. The ballast is raised inside the model, to place it closer to the axis of rotation, thus reducing the mass moment of inertia of the model as far as possible. The model is made watertight by applying sealant to the seams in the hull and by means of the latex or grease seals. Nonetheless, water may enter the hull. To remove the water, two screw pumps are mounted in the hull. The exit hoses of the pumps, the wires providing power to the pumps and the wires connecting the sensors to the measurement computer are fed through a hole on top of the sail.

Table 4-2: Main dimensions of the model

L_{oa}	2.8	[m]
L_{wl}	2.1	[m]
B_{max}	0.35	[m]
T	0.31	[m]
∇	0.20	[m ³]
VCG	0.16	[m]
GM	0.012	[m]
VCB	0.17	[m]



Figure 4-1: The model used in the experiments, with large X-rudders and bowplanes mounted.



(a) Bowplane, with hull opening (grey) and dynamometer (on the left). **(b)** Latex seal used to waterproof shaft opening. The flange on the left will be clamped in the hull opening.

Figure 4-2: Mounting of the portside bowplane.

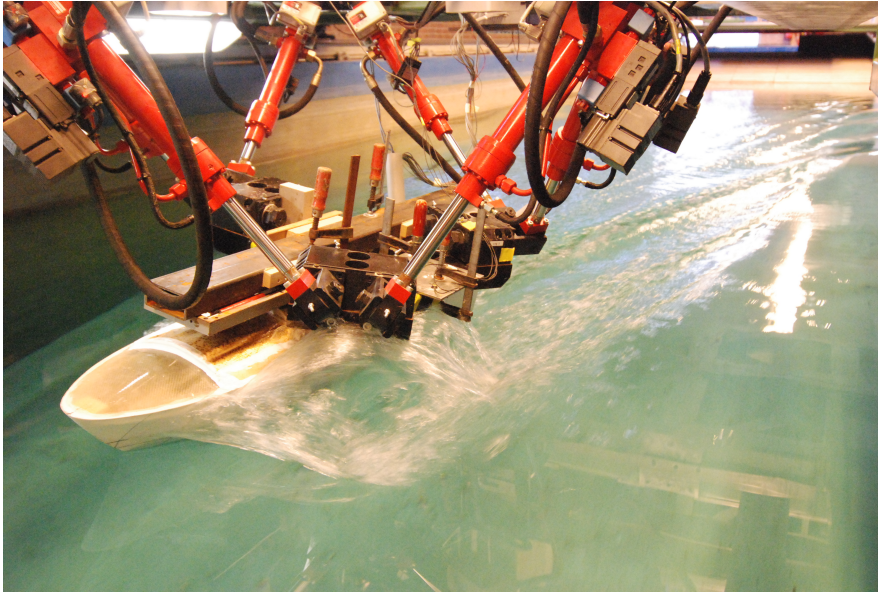


Figure 4-3: The hexamove of Delft University of Technology
Source: www.3me.tudelft.nl (accessed April 16, 2016)

4-3 Forcing the roll motion

Several possible methods to force the roll motion on the model are investigated. Two of the most promising methods are discussed here.

4-3-1 Hexamove

A possible way of forcing the roll motion on the model is by means of the Hexamove. The Hexamove is a platform with six hydraulic cylinders that can be used to precisely position a model underneath the carriage of the towing tank. By controlling the hydraulic cylinders, the position of the model can be changed during the measurement. The Hexamove is capable of forcing a pure roll motion on the model. The Hexamove is shown in Figure 4-3.

The advantage of the Hexamove is that no further supports are needed to mount the model and hence there is no disturbance in the water by support frames or drive mechanisms. However, a major disadvantage of the Hexamove is the limited stroke of the cylinders. Given the relatively low height of the model above the waterline and the mounting height of the Hexamove on the carriage, the maximum roll angle that could be forced on the model would be too low to create the wanted large roll angles. Hence, the Hexamove was not used for this research.

4-3-2 Linear drive with scotch yoke

A second way of forcing the roll motion on the model is by using a linear motor, which is connected through a scotch yoke and two connecting rods to the model. This set-up can be seen in Figure 4-4.



Figure 4-4: The linear motor, with the two connecting rods and the aft part of the shaft that transfers the roll motion to the model.

The advantage of this set-up is that it can force a pure roll motion on the model of sufficient amplitude and at all the required roll frequencies. The driving mechanism causes a disturbance in the water, but since this is behind the model it is assumed to have no influence on the measurements. This is the driving mechanism that is used in the experiments.

A sinusoidal motion is forced on the model. The slotted connection between the connecting rods and the linear motor calls for a non-sinusoidal motion of the linear motor. The displacement of the motor is instead given by the following equation:

$$x = L \tan(\varphi_A \sin(\omega t)) \quad (4-1)$$

In which:

- x = the displacement of the linear motor
- L = the vertical distance between the pivot point and the linear motor
- φ_A = the amplitude of the roll motion
- ω = the frequency of the roll motion

4-4 Mounting of the model

A free sailing model was briefly considered, but it would be quite hard to force the roll motion on a free sailing model. A free sailing model would also require active control of rudders by an autopilot and an engine driving the propeller, all of which would cause moments acting on the hull. These moments would interfere with the measurement of the damping moment. For these reasons, the model was fixed to and towed by the carriage.

The roll damping is the subject of research. As such, it is attractive to limit the motion of the model to only one degree of freedom: roll. All other motions that might be coupled to the roll motion are excluded. The advantage of this approach is that every change in roll damping is



Figure 4-5: Inner end of the shaft and its connection to the force sensors for the total torque measurements. One of the sensors can be seen on the left.

directly reflected in the measured moment and not partially lost in other, coupled, motions. Pure roll is achieved by fixing all other motions of the model.

In the experiments, the model was rotated around the axis of revolution of the hull, which does not coincide with the center of gravity. The center of gravity is slightly lower than this axis, to obtain an inherent stable model. As a result of this offset, the motion is not strictly pure roll. The model will be subjected to sway and heave motions, as the center of gravity sways and heaves with the oscillation. The difference in height between the axis of rotation and the center of gravity is 1.5 cm. With this small offset, the heave motion of the center of gravity will be 2 mm and the sway motion 8 mm, which is deemed small enough to be neglected.

The model will be mounted underneath the carriage of the towing tank between two support frames. Two frames are used to ensure that the model is correctly aligned with the towing tank and to limit bending stresses and deformations in the set-up. The total set-up can be seen in Figure 4-6. The model is connected to the frames by two shafts: one front and one aft. The front shaft is fixed to the model, while the aft shaft is fixed to the forcing mechanism and passes through the hull, where it is connected to two force sensors to measure the total torque on the hull, see Figure 4-5.

A disadvantage of using two frames to support the model is that the flow in front of the model is influenced by the front support. Figure 4-7 shows the submergence of the support at zero and at the highest forward speed. At the highest forward speed, the bow wave reaches the thicker part of the support. However, since resistance measurements are no part of the experiment, the effect of the support on the measurements is assumed to be negligible. In fact, the disturbances caused by the support probably help to trip the boundary layer to cause turbulent flow over the full length of the model, just as on a full scale submarine. Hence the disadvantage of this set-up is deemed smaller than the advantage of limiting bending stresses and the better alignment of the model.

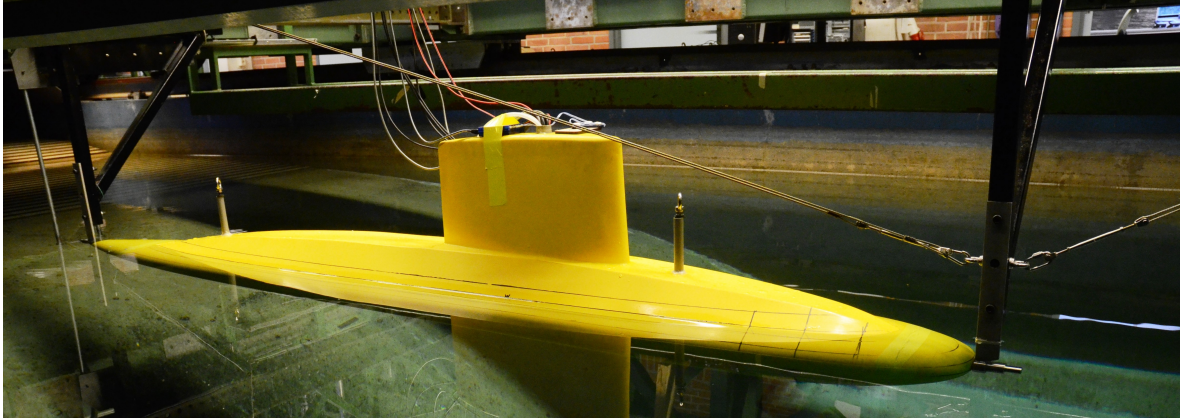
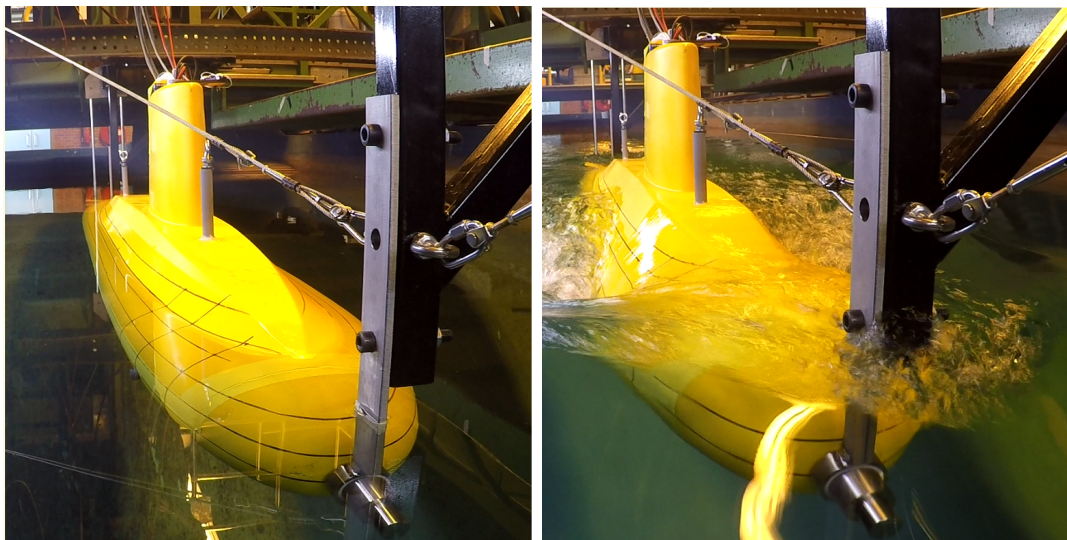


Figure 4-6: Model in the experimental set-up. The front support is braced by the steel wires to increase the stiffness of the set-up. The connecting rods of the driving mechanism can be seen at the far left.



(a) Forward speed = 0 m/s.

(b) Forward speed = 1.26 m/s

Figure 4-7: Submergence of the front support at different forward speeds.

4-5 Measurement equipment

In the experimental set-up, a maximum of six forces is measured. The forces are forces normal to four rudders (two front, two aft) and the torque acting on the hull. Only two of the four aft rudders can be measured at once, due to the limited space inside the hull to mount the force sensors. Two opposite rudders can be measured at once. The position of the model, in six degrees of freedom, is measured through an optical measurement device (Certus). In addition to these forces, the forward speed of the towing tank carriage is measured.

The forces are measured using two types of force sensors. The forces on the rudders are measured using so called 'dynamometers'. A dynamometer consists of two parallel plates, connected by four small strips. When a force is applied to the dynamometer, the strips bend. Strain gauges are glued to each of the strips. The deformation measured by the strain gauges is a measure for the force applied to dynamometer. A dynamometer is shown in Figure 4-2a. The dynamometer is a reliable force sensor, which is stiff in five out of six degrees of freedom and has a relative low noise level. They are available in 5 kgf, 10 kgf, 20 kgf and 40 kgf. For these experiments, the smallest sensors have been used.

The second type of force sensor is used to measure the torque acting on the hull. This sensor is a commercially available force sensor and works according to the same principle as the dynamometer. This sensor is shown in Figure 4-5. The advantage of this sensor is the smaller footprint when compared to the dynamometer, making it better suitable to mount at the position needed to measure the torque. The range of these sensors is 20 kgf.

The sample rate used for the sampling is 1000 Hz for the force sensors and 50 Hz for the Certus. The sampled signals are amplified and filtered. A second order lowpass filter is used, with a 3 dB reduction of the power of the signal at 100 Hz. At 10 Hz the reduction is less than 0.1%, while at 1000 Hz the power of the signal is less than 0.1%. With this configuration of the filter, frequencies below 10 Hz are virtually unaffected, both in power and in phase, and can be used in the signal processing.

The filtered signals of the force sensors and the Certus are saved separately, together with their time vectors, on the measurement computer.

4-6 Measurement matrix

The measurement matrix contains all the different combinations of variables that will be measured during the experiment. There are four variables that will be varied:

- Forward speed (V_s)
- Roll amplitude (φ_A)
- Roll frequency (ω)
- Rudder configuration

The model will be tested at three forward speeds, equivalent to 6, 8 and 12 knots at full scale. A forward speed of 12 knots is a typical maximum velocity for a surfaced submarine. The

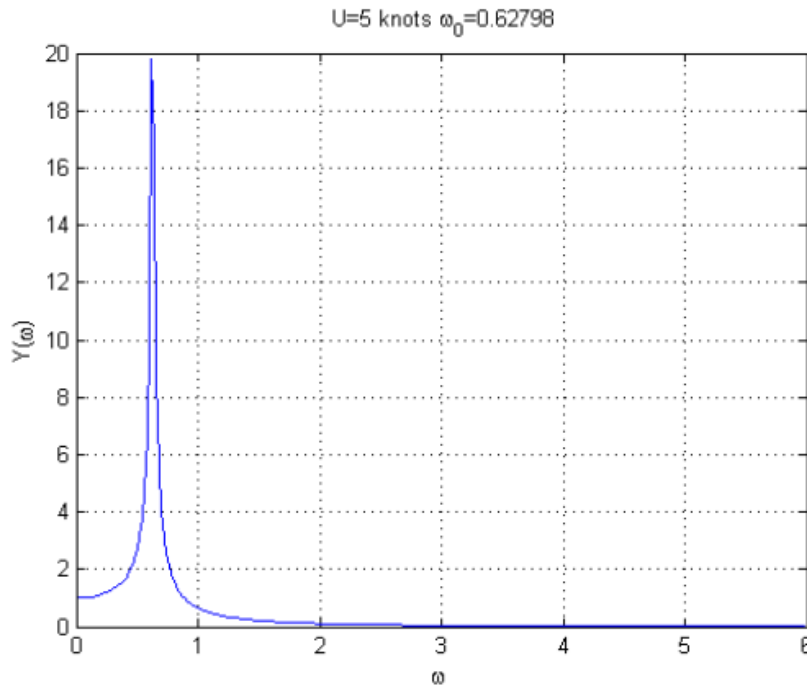


Figure 4-8: A typical transferfunction for the roll motion of a surfaced submarine with forward speed, plotted against the dimensionless wave amplitude. Note the sharp peak in the transfer function. Reproduced from Hedberg (2006).

lower speeds of 6 and 8 knots are chosen to give a spread over the typical forward speeds at which a surfaced submarine operates.

Three roll amplitudes will be tested: 10, 20 and 30 degrees. 30 degrees of roll amplitude seems to be a not unreasonable large amplitude that occurs during full scale operations. See for instance Efimov et al. (2003). The lower roll amplitudes are included to investigate the roll motion under less severe circumstances.

A total of four roll frequencies will be tested: 0.70, 0.57, 0.48 and 0.42 rad/s¹. It is expected that the roll response of a surfaced submarine will mainly be in its eigenfrequency. This is for instance shown in the transfer functions given by Hedberg (2006), one of which is shown in Figure 4-8. The eigenfrequency in roll will change from submarine to submarine. To account for this spread in eigenfrequencies, a range of frequencies has been chosen.

In total, six different rudder configurations will be tested:

- Hull with small rudders in X-configuration
- Hull with bowplanes and small rudders in +-configuration, horizontal rudders being measured
- Hull with bowplanes and small rudders in +-configuration, vertical rudders being measured

¹These roll frequencies correspond to the roll periods 9, 11, 13 and 15 s.

- Hull with bowplanes and large rudders in X-configuration
- Hull with large rudders in X-configuration
- Bare hull, without rudders

Here, ‘small rudders’ refers to the rudders that correspond to the +-configuration. The X-configuration is measured with both the small and the large rudders, to study the effect of increasing the rudder size. The hull is measured in X-configuration both with and without bowplanes, to study the effect of the bowplanes. The +-configuration needs to be measured twice, because the vertical rudders operate in a clearly different flow than the horizontal rudders. Both need to be measured. The effect of the orientation of the rudders is measured by comparing the +-configuration and the X-configuration with small rudders.

The total number of tests in the test matrix is thus 216. A number of measurements will be repeated to check the repeatability of the measurements. In addition to these tests, test runs will be performed to measure the stability of the model, both with and without forward speed. Hence, the total number of measurements will be larger than 216.

The choice for such a large measurement matrix is deliberate. By measuring this many combinations, the model can be validated over the whole domain of interest.

The length of the measurements is such that at least ten steady-state oscillations are measured. Since the runs in the towing tank are time based rather than based on the actual number of oscillations, more oscillations are measured for the higher frequencies. The number of oscillations is always far greater than the number of oscillations than is common practice (ITTC, 2008).

Chapter 5

Data processing

The raw measurement data needs a certain amount of checking and processing before any conclusions can be drawn from the measurements. This chapter describes the process of checking and processing used to create information from raw measurement data.

5-1 Clipping measurement signals

Each measurement in the experimental phase was started before the model was actually rolling and stopped after the model had come to a complete standstill. As a result, two transient phases were measured in addition to the steady state phase. In these transient phases, the model has not yet reached the required forward velocity and roll amplitude and is still accelerating. The parts of the measurement signals that correspond to these transient phases are removed from the measurement signal. Figure 5-1 shows an example of a measurement signal in which the different phases are marked.

In those cases where peaks appear in the measurement signal and where it is clear that those peaks are due to some anomaly, the corresponding part of the measurement signal is removed before further analysis is performed. An extreme example of such a peak is shown in Figure 5-2.

5-2 Minimum amplitude condition

The sensors that have been used need a minimal load before they perform accurately. If the load is too small, the signal is unreliable: the magnitude of the signal cannot be relied upon to be accurate. As a rule of thumb, the load needs to be above 4%-5% of the maximum load of the sensor to be reliable. Each signal was checked to see if this minimum amplitude requirement was met. If this was not the case, the signal was removed from the data set.

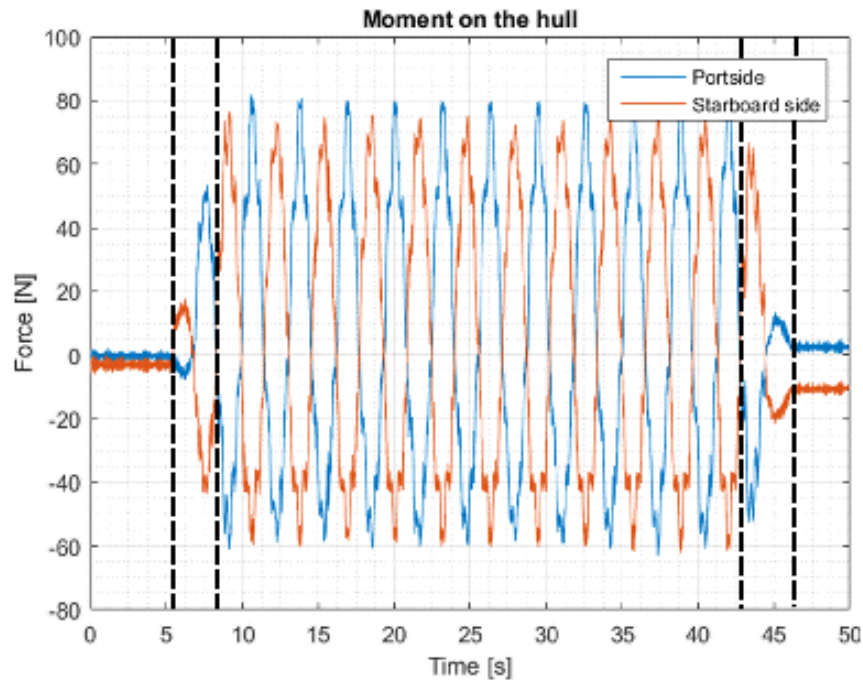


Figure 5-1: Measurement signal. The dashed lines indicate the change from each phase to the next. Respectively: Model fully stopped - transient phase - steady state - transient phase - model fully stopped. Only the steady state phase is relevant for the experiment.

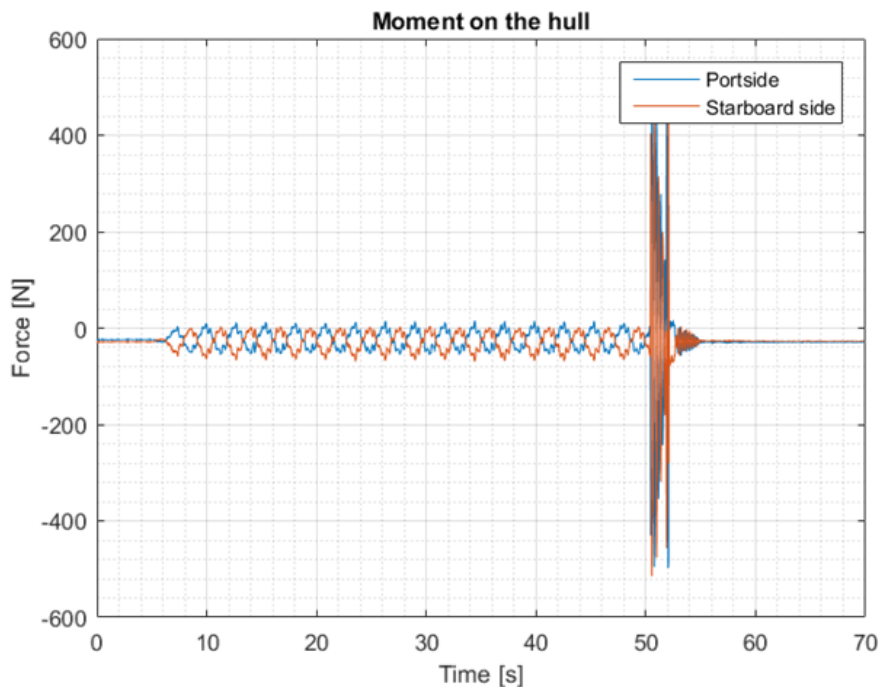


Figure 5-2: Measurement signal showing extreme peaks. The peaks are caused by a malfunction of the drive motor and can thus be excluded from further processing.

5-3 Unreliable experimental results

For some experiments, the measurement signals are known to be unreliable. In those cases the signals have been removed from the dataset. The signals are declared unreliable if the signal is lost during the measurement run or when the mean is clearly not constant. This can be the result from a wet or even submerged sensor due to water ingress in the model. When the signal amplitude is too small, as stated in Section 5-2, the signals is declared unreliable as well.

A second reason for rejecting a series of experimental data is the failing of one of the bow sensors. The bow rudders are expected to produce anti-symmetrical forces: the rudders are placed in the same flow and perform the same motion, only with a phase difference of 180 degrees. Hence, the amplitudes of the signals are expected to be the same. It was noticed during the experiments that the signals of the portside sensor were differing from the signals from the starboard side sensor. Upon inspection, the port sensor turned out to be slightly deformed, thus changing its measurement properties. The sensor was replaced, but all previous signals were declared unreliable.

For another series of experiments, the starboard bow sensor gave a lower force amplitude than the port sensor. After realigning the sensor with the opening in the hull this effect disappeared. Presumably, the rudder shaft rubbed against the sides of the hull opening. The measurement signals for which this was the case were declared unreliable and removed from the data set.

5-4 Noise

Every measurement signal has a certain amount of noise obscuring the actual signal. This need not be a problem, as long the level of noise is low with respect to the signal itself. To determine the noise level, the signal to noise ratio of the signal has been determined. The signal to noise ratio compares the power of the noise to the power of the signal itself:

$$SNR = \left(\frac{\text{rms}(\text{signal})}{\text{rms}(\text{noise})} \right)^2 \quad (5-1)$$

In which:

- SNR = the signal to noise ratio
- rms = the root mean square
- signal = the signal without noise
- noise = the disturbance on the signal

A signal to noise ratio of less than five is deemed too low to extract the signal with reasonable accuracy. Every measurement signal for which the signal to noise ratio was less than five has been excluded from the data set.

5-5 Spectral components of the signal

The measurement signals contain a significant amount of noise and other disturbances. A Fourier transformation has been applied to the signals, to identify the frequency components of

the measurement signal. A typical result of this Fourier transform is shown in Figure 5-3. The lower peaks in the signal correspond to either higher harmonics of the signal or disturbances in the roll motion. Figure 5-4 shows the Fourier transforms of the signals of the force sensors in the hull and the corresponding roll motion sensor. The Fourier transform of the roll motion should only contain a single frequency: the desired frequency for the roll motion. However, if the motion of the model is not sine shaped, more frequencies will be found in the Fourier transform. These other frequencies cause reactions of the measured forces at those frequencies.

An example: In the right hand graph of Figure 5-4, the Fourier transform of the roll motion is shown. The highest peak corresponds to the desired roll frequency. In addition to this peak, two smaller peaks can be seen at 10 rad/s and 17 rad/s. These peaks account for irregularities in the sine shape of the roll motion. In the left hand graph, the Fourier transform of the hull forces is shown. At 10 rad/s and 17 rad/s, peaks appear in the Fourier transform. These peaks are directly related to the peaks in the roll motion signal. If the roll motion would have been a proper sine, the peaks at 10 rad/s and 17 rad/s in the force signal would not exist. The other peaks in the force signal are higher harmonics of the frequency.

The discrepancy between the actual shape of the roll motion and a sine shape, is caused by the linear motor that is used to force the motion. The linear motor receives an analogue signal that corresponds to the required displacement of the motor. A PID controller is used to ensure that the required displacement matches the current displacement. When the coefficients of the PID controller are not optimal for the motion, the motion will not exactly match the required motion. The less optimal the settings of the controller, the more the actual motion will deviate from the required sine shaped motion. This has been tested for a few measurements where the actual roll motion clearly deviated from the required motion. It was seen that for a different set of PID coefficients, the roll motion improved and the peaks in the force spectrum reduced.

It is possible to exclude unwanted frequencies from the measurement signal by removing them from the Fourier transform. After removal, an inverse Fourier transform is made to regain a signal in the time domain. Frequencies higher than 10 Hz should for instance already have been filtered in the analogue filter in the measurement set-up. Frequencies higher than 10 Hz can thus be regarded as noise and be removed from the signal. An example of this filtering is shown in Figure 5-5.

5-6 Base of comparison

The mathematical model predicts the shape of the signals. This knowledge has been used in processing the experimental data. Based upon the mathematical prediction, it was known that a relatively simple comparison based on (fitted) sine function is not possible. The validation of the mathematical model with the experimental results will therefore take place by comparing the time traces of the calculated and measured forces.

For a deeply submerged rudder, subjected to a sinusoidal motion, a sinusoidal force signal is expected. Experimental data confirms the expectation. An example is shown in Figure 5-6. For surface piercing rudders however, due to the changing wetted area and aspect ratio, the force is no longer expected to be sinusoidal. Experimental data confirmed this expectation. Figure 5-7 shows the experimental data of a surface piercing rudder and a sine fit through the measurement signal.

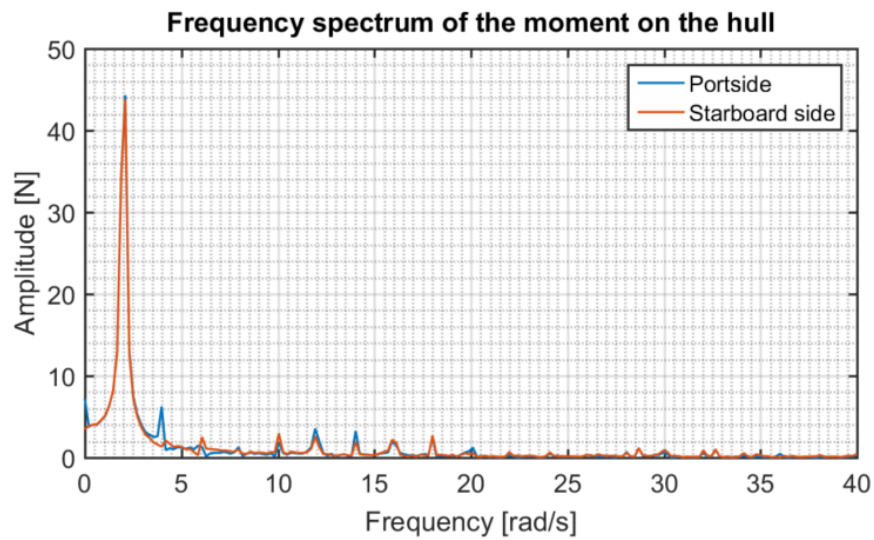


Figure 5-3: A typical Fourier transform of the measurement signal. The major peak corresponds to the oscillation frequency.

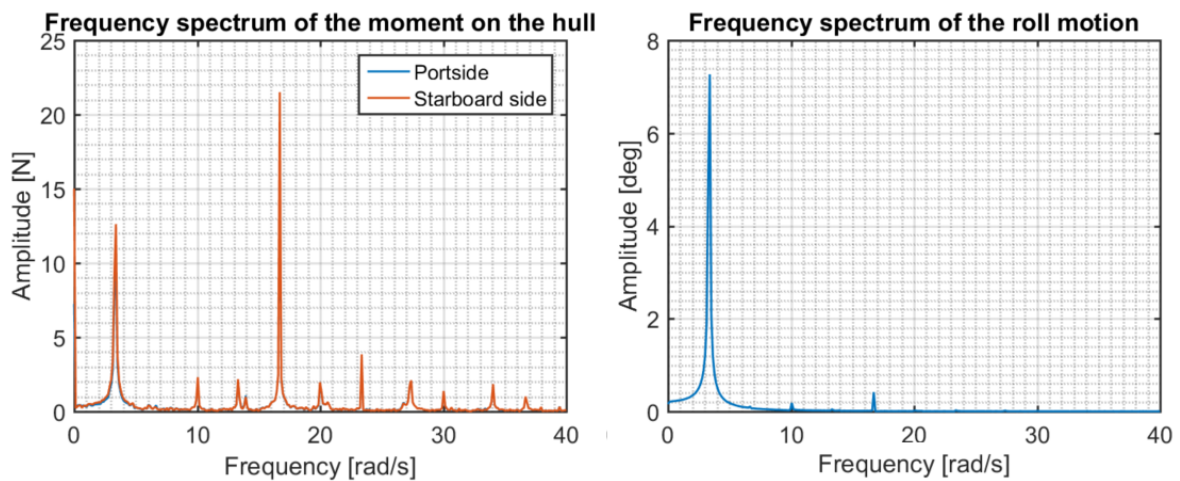


Figure 5-4: Left: Fourier transform of force sensors. Right: Fourier transform of the corresponding roll motion.

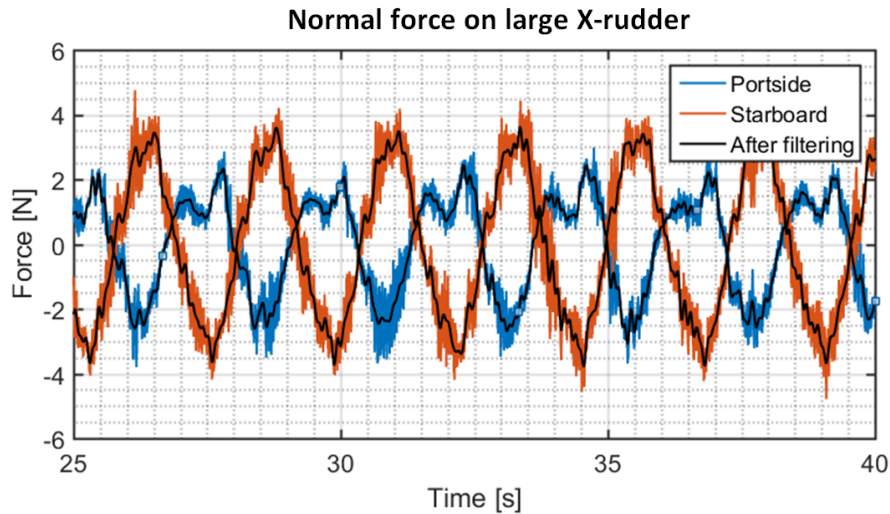


Figure 5-5: An example of a signal for which the frequency components above 10 Hz have been removed using a Fourier transform.

The signals from the torque sensors in the hull are expected to be more sinusoidal than the signals of the surface piercing rudders. Here, the total of all rudder forces combined with inertia and stability moments is measured. By combining more forces, the influence of one or two small non-sinusoidal signals is reduced. For most experiments, this is indeed the case, as can be seen in Figure 5-8a. However, in those cases where the linear motor does not produce a perfect sinusoidal motion, the influence of the other frequencies in the motion signal is strongly sensed by the torque sensors, as can be seen in Figure 5-8b. Therefore, it is not always possible to approximate these signals with a simple sine function.

Since the signals of the surface piercing rudders and the torque signals are composed of multiple frequencies, it is not possible to compare the experimental results and the results of the mathematical model by means of an amplitude. Comparing by means of the power of the signal is possible, but information about the specific 'humps and hollows' of the signal would be lost. Hence, the choice has been made to compare the actual time traces of the signals. In that way, the best comparison is made for all the measurements.

5-7 From forces to moments

The six sensors in the hull measure forces. To get the corresponding moments, these calculations are made:

$$M_{\text{bow}} = (F_{\text{PS}} - F_{\text{SB}})_{\text{bow}} \cdot 0.464 \quad (5-2)$$

In which:

- M = the moment produced by the specified forces
- F = the forces measured in the experiments

The calculation for the aft rudders depends on the configuration. In the case of X-rudders

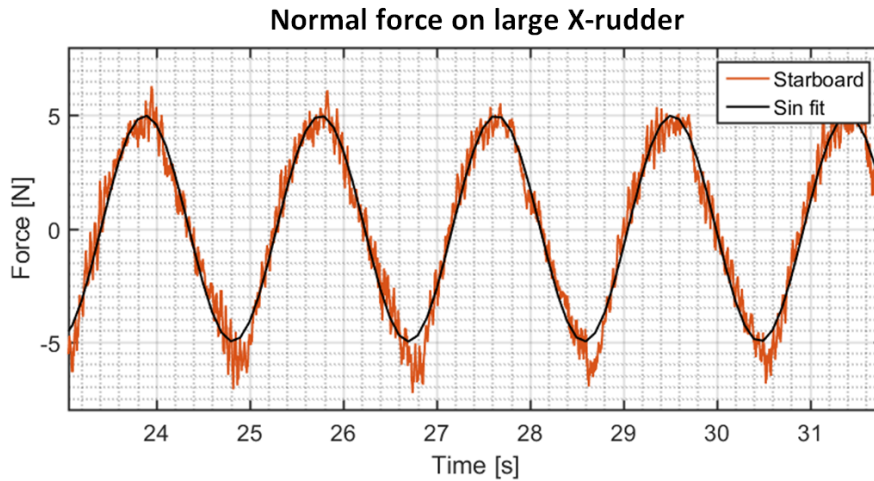


Figure 5-6: Force signal of a deeply submerged rudder. The black line is a sine fitted through the signal. It can be seen that the force signal is almost sinusoidal.

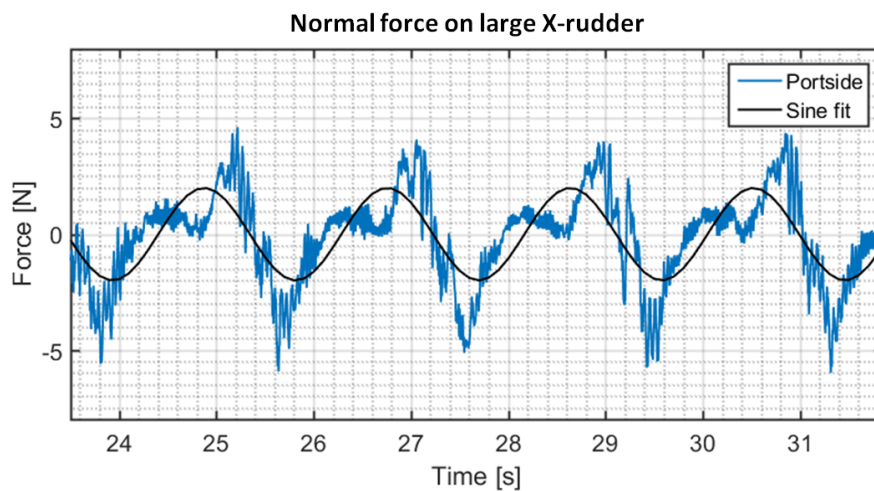
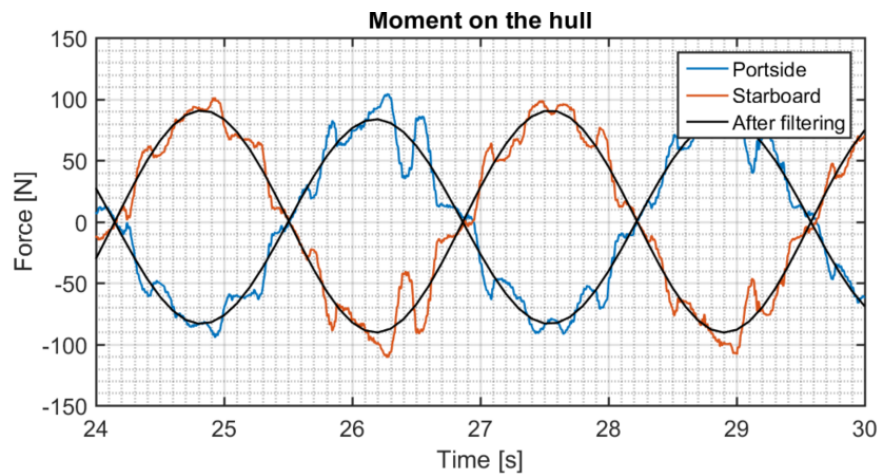
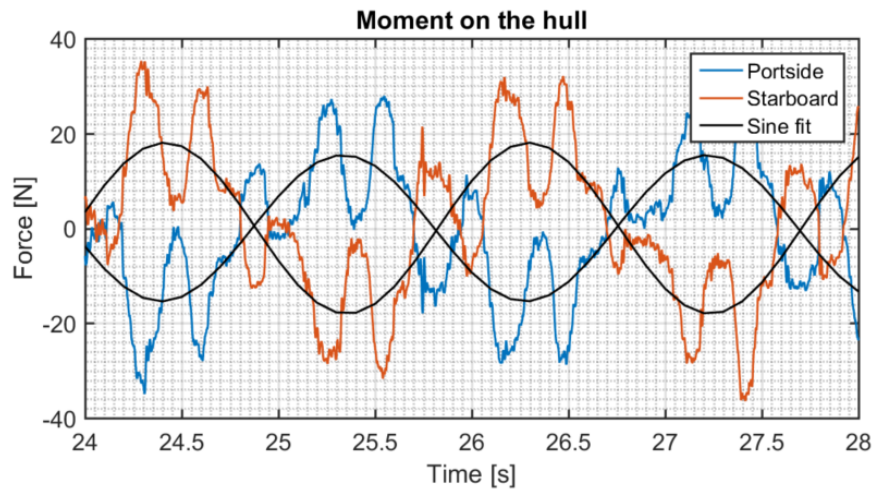


Figure 5-7: Force signal of a surface piercing rudder. The black line is a sine fitted through the signal. The sine is a poor fit for this measurement signal.



(a) Torque signal with very small disturbance from the drive motor.



(b) Torque signal with large disturbance from the drive motor.

Figure 5-8: Torque signals of the hull. Sine functions are fitted through the signals. In the top graph, the sine is an acceptable representation of the signal, while in the bottom graphs the sine is a very poor fit through the signals.

(both small and large):

$$M_{\text{aft}} = (F_{\text{PS}} - F_{\text{SB}})_{\text{aft}} \cdot 2 \cdot r \quad r = \begin{cases} 0.398 & \text{For large X-rudders} \\ 0.298 & \text{For small X-rudders} \end{cases} \quad (5-3)$$

In the case of rudders in cross-configuration, the forces of the measurements of the horizontal and vertical rudder set-ups need to be combined:

$$M_{\text{aft}} = (F_{\text{PS}} - F_{\text{SB}})_{\text{aft}} \cdot 0.298 + (F_{\text{bottom}} - F_{\text{top}}) \cdot 0.298 \quad (5-4)$$

The total moment that is acting on the whole model is given by:

$$M_{\text{total}} = (F_{\text{PS}} - F_{\text{SB}})_{\text{hull}} \cdot 0.15 \quad (5-5)$$

5-8 Determination of in and out of phase parts of the moment

In those cases where the torque signals can be approximated by a sine function, see Section 5-6, it is possible to determine the roll damping of the model. For this, the signal is split into parts in phase with the motion and out of phase with the motion. The out of phase part is the roll damping of the model. The derivation of this calculation is given here.

$$\varphi = \varphi_A \sin(\omega t + c) \quad (5-6)$$

$$M = M_A \sin(\omega t + \epsilon) \quad (5-7)$$

In which:

- φ = the roll angle at time t in radians
- φ_A = the roll amplitude
- ω = the roll frequency
- t = the time
- c = the phase of the roll motion
- M = the torque acting on the hull at time t in Nm
- M_A = the amplitude of the moment
- ϵ = the phase of the moment

The phase angle between the motion signal and the moment signal equals:

$$\text{Phase angle} = c - \epsilon \quad (5-8)$$

Eq. (5-7) must be rewritten to contain a part in phase and a part out of phase with the roll motion:

$$M = M_A \sin(\omega t + \epsilon) = A \sin(\omega t + c) + B \cos(\omega t + c) \quad (5-9)$$

Using the trigonometric addition formulas, Eq. (5-9) can be rewritten to:

$$A \sin(\omega t) \cos(c) + A \sin(c) \cos(\omega t) + B \cos(\omega t) \cos(c) - B \sin(\omega t) \sin(c) = M_A \sin(\omega t) \cos(\epsilon) + M_A \cos(\omega t) \sin(\epsilon) \quad (5-10)$$

Assume $\omega t = 0$. Than, Eq. (5-10) reduces to:

$$A \sin(c) + B \cos(c) = M_A \sin(\epsilon) \quad (5-11)$$

Assume $\omega t = \frac{\pi}{2}$. Then, Eq. (5-10) reduces to:

$$A \cos(c) - B \sin(c) = M_A \cos(\epsilon) \quad (5-12)$$

Eq. (5-11) and Eq. (5-12) can be taken together and rewritten as:

$$\begin{bmatrix} \sin(c) & \cos(c) \\ \cos(c) & -\sin(c) \end{bmatrix} \begin{bmatrix} A \\ B \end{bmatrix} = \begin{bmatrix} M_A \sin(\epsilon) \\ M_A \cos(\epsilon) \end{bmatrix} \quad (5-13)$$

And hence:

$$\begin{bmatrix} A \\ B \end{bmatrix} = \begin{bmatrix} \sin(c) & \cos(c) \\ \cos(c) & -\sin(c) \end{bmatrix}^{-1} \begin{bmatrix} M_A \sin(\epsilon) \\ M_A \cos(\epsilon) \end{bmatrix} \quad (5-14)$$

Now, the part of the moment that is in phase with the motion is given by:

$$M_{\text{in phase}} = A \sin(\omega t + c) \quad (5-15)$$

And the part of the moment that is out of phase with the motion is given by:

$$M_{\text{out of phase}} = B \cos(\omega t + c) \quad (5-16)$$

Where A and B are given by Eq. (5-14).

Chapter 6

Results

This chapter will describe the results from this research. As stated in Section 5-6, a comparison is made in the time domain between the results of the mathematical model and the results of the experiments. This chapter will show a number of these comparisons. The full set of time traces of the experiments and the corresponding mathematical results is included in Appendix D.

6-1 Usable measurements

As stated in Section 4-6, a large number of experiments have been carried out. All experiments were studied and checked against the conditions mentioned in Chapter 5. In this process, quite some experiments had to be rejected. For most of the rejected experiments, the amplitude of the measured force signals was too small to be reliable. Unfortunately, it was not possible to change the force sensors for these experiments with sensors with a smaller range, because the smallest sensors available were already used.

The experiments that provided usable data are listed in Table 6-1, Table 6-2, Table 6-3, Table 6-4 and Table 6-5. For the bowplanes and the large X-rudders the desired measurement matrix has been mostly covered, with only the cases with a low loading (low velocity and lower frequencies) being omitted. The measurements with +-configuration and small X-rudders have hardly been covered however. For the purpose of validation of the mathematical model however, it is felt that validation can still be achieved. The calculations of shallowly submerged horizontal foils can be validated against experimental data on the bowplanes. The calculations for the small X-configuration are essentially equal to the calculations for the large X-configurations and can therefore be validated against the experimental data from the large X-configuration.

6-2 Repeatability

Several combinations of rudder configuration, forward speed, roll amplitude and roll frequency were measured more than once. Reason for these additional measurements was to study the

Table 6-1: Bowplanes

If the same condition has been measured multiple times, this may result from repeat measurements with the same configuration, or from the same conditions with a different aft rudder configuration.

Velocity [m/s]	Frequency [rad/s]			
	2.052	2.368	2.798	3.420
0.63	-	30	30	20, 30 (2x)
0.84	30	30 (2x)	20, 30 (2x)	20 (2x), 30 (2x)
1.26	20, 30	20 (2x), 30	10, 20, 30 (2x)	10, 20, 30

Table 6-2: Small X-configuration

Velocity [m/s]	Frequency [rad/s]			
	2.052	2.368	2.798	3.420
0.63	-	-	-	-
0.84	-	-	-	30
1.26	-	-	-	-

Table 6-3: +-configuration, horizontal rudders

Velocity [m/s]	Frequency [rad/s]			
	2.052	2.368	2.798	3.420
0.63	-	-	-	-
0.84	-	-	-	30
1.26	-	-	-	30

Table 6-4: +-configuration, vertical rudders

Velocity [m/s]	Frequency [rad/s]			
	2.052	2.368	2.798	3.420
0.63	-	-	-	-
0.84	-	-	-	30
1.26	-	-	-	30

Table 6-5: Large X-configuration

If the same condition has been measured multiple times, this may result from repeat measurements with the same configuration, or from the same condition with a different configuration (with or without bowplanes).

Velocity [m/s]	Frequency [rad/s]			
	2.052	2.368	2.798	3.420
0.63	-	-	30	30 (2x)
0.84	-	30	30 (2x)	20 (2x), 30 (4x)
1.26	30	30 (2x)	20, 30 (2x)	20, 30 (2x)

repeatability of the experimental results. The conditions that have been measured multiple times are indicated in Table 6-1 and Table 6-5. In some cases, the rudder configuration was different, but the forward velocity, roll frequency and roll amplitude were equal. Bowplanes have been measured with different aft rudders configuration and the large X-configuration has been measured with and without bowplanes.

The experiments show a very good repeatability. Figure 6-1 and Figure 6-2 show how well the experimental data reproduced. Although these two graphs show only the results of one condition for the aft rudders and one condition for the bowplanes, they are representable for all the other cases.

6-3 Validation of the mathematical model

The time traces of the experimental results and the mathematical model are compared to draw a conclusion on the validity of the mathematical model. To make the comparison of the signals easier, the phase angles are adjusted in such a way that the roll motions are synchronised for both signals.

6-3-1 Bowplanes

Phase angle

The calculated results of the mathematical model and the experimental results are almost equal. The results from the mathematical model show a small phase difference with the experimental results, with the experimental results being slightly less out of phase with the motion. The phase difference appears to be dependent on the rotational velocity: for low roll frequency and low roll amplitude (see Figure 6-3a), the phase difference is larger than for high roll frequencies and roll amplitude (see Figure 6-3b).

The lift and drag forces that are calculated in the model are proportional to the velocity squared, which is out of phase with the motion. However, water is accelerated by the rudders, which causes a force in phase with the motion and thus creating a phase difference with the calculated results. This inertia force is excluded from the model as it was expected to be small.

Shape of the signal

The shape of both the mathematical results and the experimental results is very similar. The mathematical results are not influenced by higher harmonics or disturbing frequencies of the linear motor, which can be seen to be present to some extent in the experimental signals.

Magnitude of the signal

The calculated signal gives a good prediction of the magnitude of the experimental signal. In those cases where the phase difference is larger, the calculated signal under predicts the

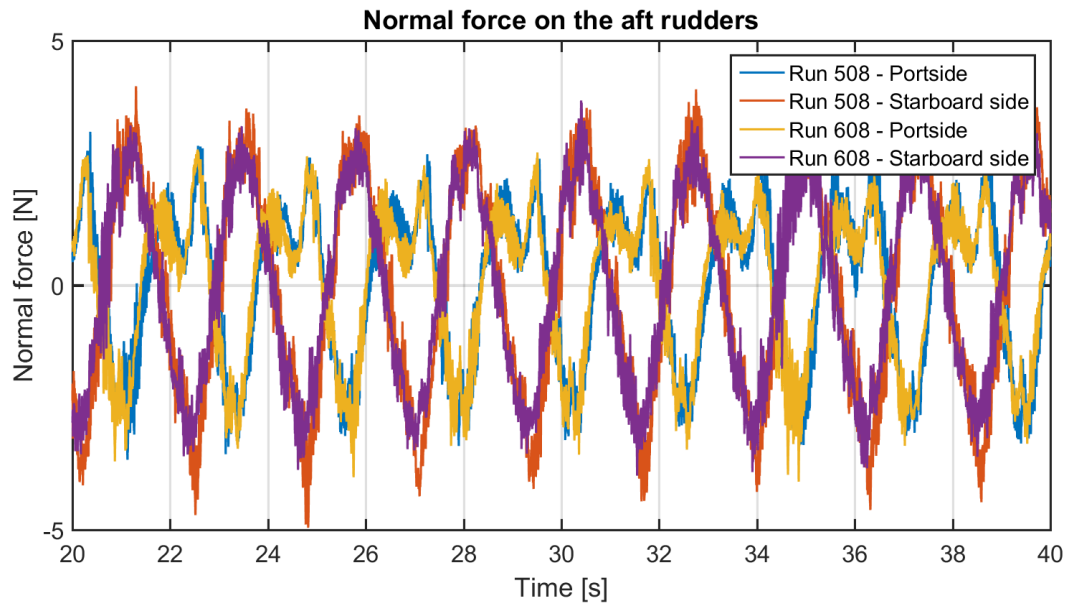


Figure 6-1: Comparison of the force signals of aft rudders in large X-configuration for two experiments.

Conditions: $V = 0.63 \text{ m/s}$, $\varphi_A = 30^\circ$, $\omega = 2.798 \text{ rad/s}$

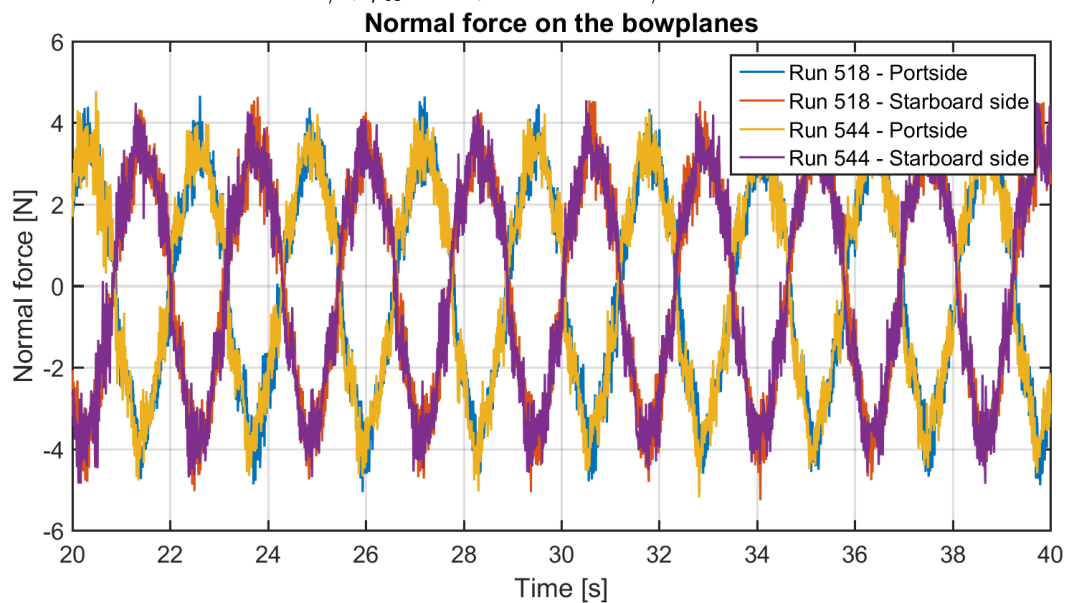


Figure 6-2: Comparison of the force signals of the bowplanes for two experiments.

Conditions: $V = 1.26 \text{ m/s}$, $\varphi_A = 20^\circ$, $\omega = 2.798 \text{ rad/s}$

Table 6-6: Difference in out of phase force magnitude of the bowplanes.

Run number	ΔF Portside [N]	ΔF Starboard side [N]
458	0.10	0.11
462	0.14	0.27
464	0.31	0.37
478	0.30	0.27
484	0.23	0.19
488	0.30	0.37
490	0.55	0.52
500	0.62	0.49
502	0.38	0.38
508	0.46	0.45
512	0.25	0.18
514	0.39	0.33
516	0.26	0.19
518	0.49	0.46
520	0.81	0.69
524	0.42	0.43
526	0.61	0.63
530	0.42	0.38
532	0.67	0.68
534	0.36	0.29
540	0.40	0.35
542	0.65	0.68
544	0.45	0.44
546	0.71	0.70
548	0.98	0.98

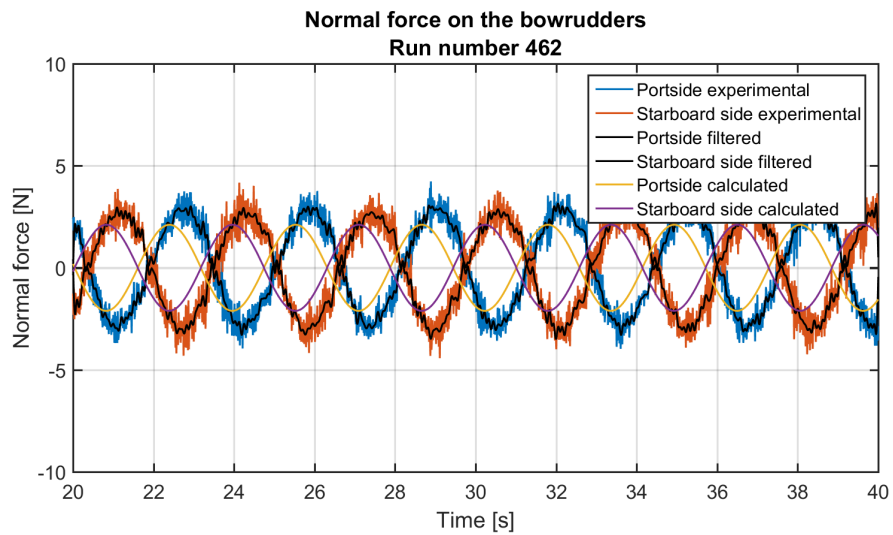
experimental results. This is not unexpected, as the measured force signal contains an in phase part, which is not included in the calculations.

Since the rudders stay submerged over the length of the oscillation, an approximation by means of a sine function can be made. Given this approximation it is possible to calculate the part of the force that is out of phase with the motion (following Section 5-8). Table 6-6 shows the difference between the calculated results and the out of phase part of the measured signal. In all cases, the measured force is under predicted, but the actual difference is always very small, less than 1 Newton.

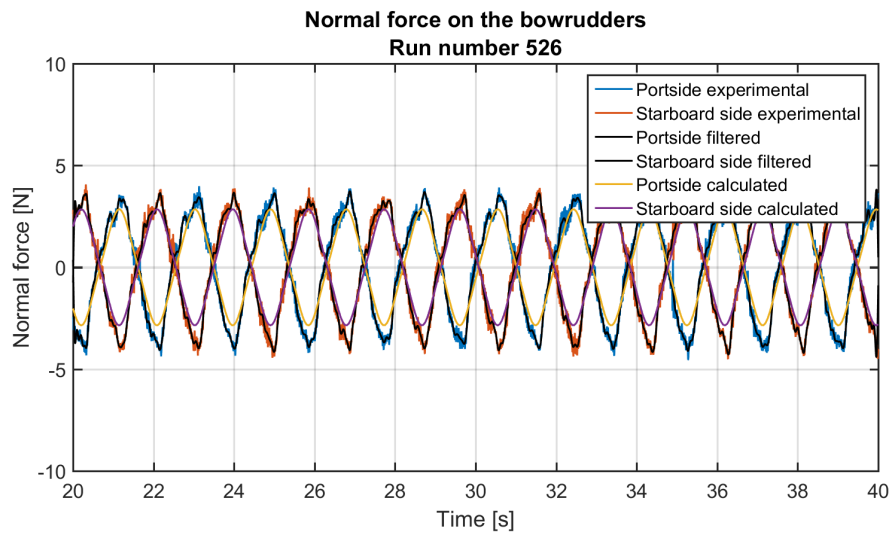
6-3-2 Aft rudders

Phase angle

In general the phase of the force signal is well captured by the calculations. For the large X-configuration, the phase angles are almost identical. For the horizontal rudders in the



(a) $V = 1.26 \text{ m/s}$, $\varphi_A = 20^\circ$, $\omega = 2.052 \text{ rad/s}$



(b) $V = 0.63 \text{ m/s}$, $\varphi_A = 30^\circ$, $\omega = 3.420 \text{ rad/s}$

Figure 6-3: Phase shift between the calculated and measured results of the bowplanes.

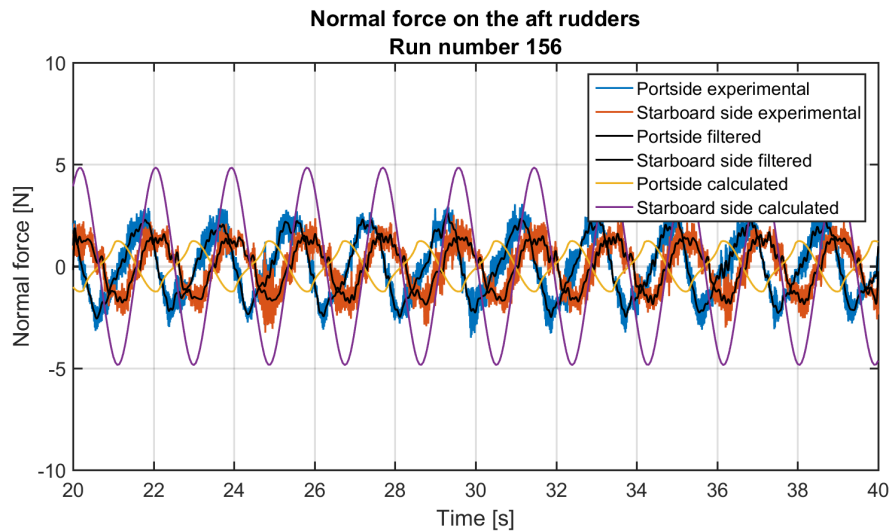


Figure 6-4: Small X-configuration
 $V = 0.84 \text{ m/s}$, $\varphi_A = 30^\circ$, $\omega = 3.420 \text{ rad/s}$

+ -configuration, a small phase difference is found. It is assumed that this difference is analogue to the difference found at the bowrudders, see Section 6-3-1: the force due to the acceleration of water is not included in the calculations, which causes the phase shift.

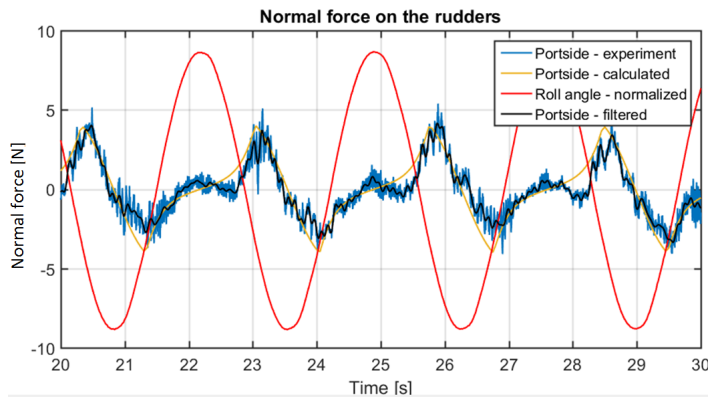
In the cases of the small X-configuration and the top rudder of the + -configuration, a significant phase shift was observed. See Figure 6-4 and Figure 6-6. In both cases, the badly matched signals correspond to small, barely surface piercing, rudders. The phase of the measured signal is shifted significantly in the direction of the motion, to the point of being almost in phase with it, indicating that the inertia forces are dominating the normal force experienced by the rudder. The lift forces are apparently very small, which is in accordance with the calculated results.

Shape of the signal

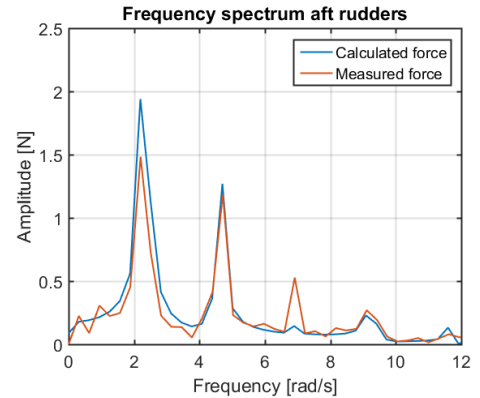
In general, the shape of the measured signal is captured quite well by the calculations. Even the more complex signal shape of the surface piercing rudders in the large X-configuration, is fairly well captured.

Figure 6-5a and Figure 6-5c show the force signals of the surface piercing rudder and the corresponding calculations. The calculated result in Figure 6-5c is not as good an approximation of the measured signal as in Figure 6-5a. The spectra of the signals are shown in Figure 6-5b and Figure 6-5d. The spectra show that the prominent third harmonic is not captured by the mathematical model. The extent in which this peak pronounces itself in the time domain varies from experiment to experiment and is dependent on the measured variables.

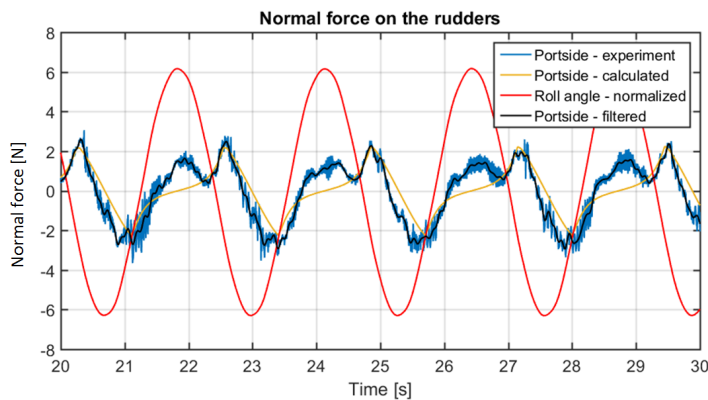
There are two cases where the calculated force signal does not match the measured signal. These cases are the runs with a + -configuration, with the vertical rudders being measured. The shape of the signals of the top rudders is not captured. The signals are shown in Figure 6-6. The measured signals of the top rudders do not show the flattened shape of the calculated signal.



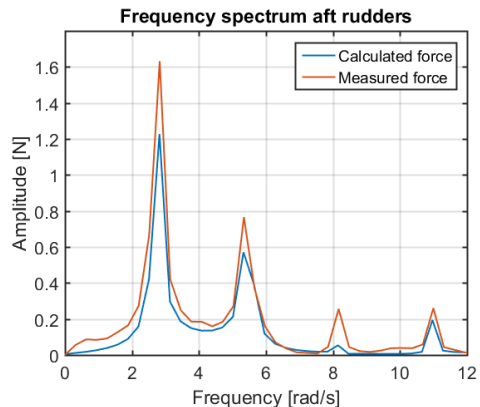
(a) Large X-configuration, with bowplanes
 $V = 1.26 \text{ m/s}$, $\varphi_A = 30^\circ$, $\omega = 2.368 \text{ rad/s}$



(b) Frequency spectrum
 $V = 1.26 \text{ m/s}$, $\varphi_A = 30^\circ$, $\omega = 2.368 \text{ rad/s}$

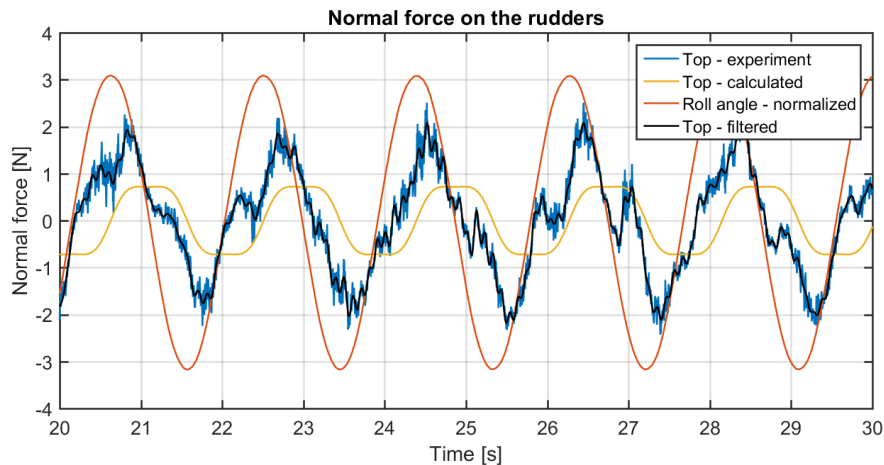
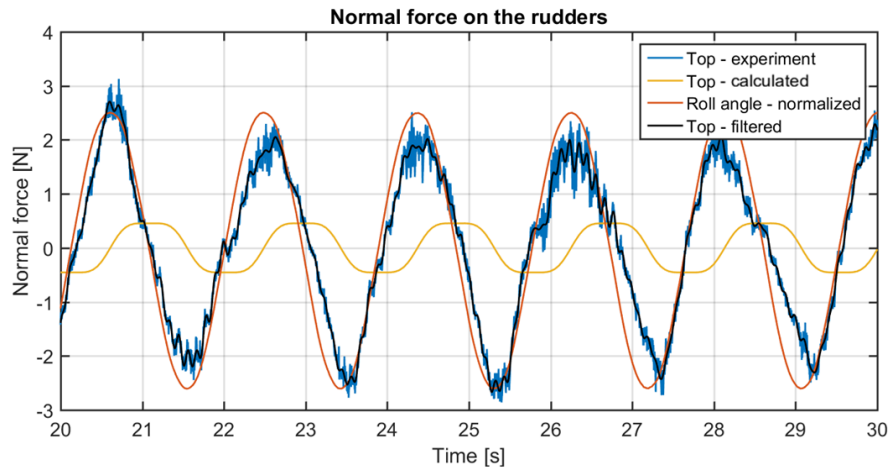


(c) Large X-configuration, with bowplanes
 $V = 0.63 \text{ m/s}$, $\varphi_A = 30^\circ$, $\omega = 2.798 \text{ rad/s}$



(d) Frequency spectrum
 $V = 0.63 \text{ m/s}$, $\varphi_A = 30^\circ$, $\omega = 2.798 \text{ rad/s}$

Figure 6-5: Surface piercing rudder of the large X-configuration. Comparison of measured and calculated forces. Note the pronounced peak of the third harmonic that is not captured by the model.

(a) $V = 1.26 \text{ m/s}$, $\varphi_A = 30^\circ$, $\omega = 3.420 \text{ rad/s}$ (b) $V = 0.84 \text{ m/s}$, $\varphi_A = 30^\circ$, $\omega = 3.420 \text{ rad/s}$ **Figure 6-6:** +-configuration, top rudder

The flat tops of the calculated signal are caused by the reduction in the area and effective aspect ratio of the rudder. The shape of the calculated signal is however influenced by a dominating in phase inertia force, as described in the paragraph on the phase angle.

Magnitude of the signal

For the large X-configuration, there is a distinct difference in how well the magnitude of the force signals is captured by the model: the signal of the surface piercing rudder is captured quite well. The signal of the deeply submerged rudder is either captured rather well, or clearly overestimated. See Figure 6-7. The cases where the signal is captured well, correspond to conditions of higher angles of attack, just up to the point of stall. The cases that are overestimated, do all have lower angles of attack. Table 6-7 shows the magnitude of the over estimated signals. It is striking that the fractional deviation between the calculated and measured results is nearly constant. This suggests that the lift curve slope of the model is too steep. When considering the cases where the force was well predicted (see Table 6-8), a nearly

Table 6-7: Magnitude of force signal of the deeply submerged rudder
Overestimated cases

Run number	Measured signal [N]	Calculated signal [N]	Δ [N]	Fraction
464	3.7	5.6	1.9	0.65
490	4.0	6.4	2.4	0.62
500	4.0	6.4	2.4	0.62
514	3.0	5.0	2.0	0.60
518	3.3	4.9	1.6	0.67
520	4.8	7.6	2.8	0.63
526	3.4	4.6	1.2	0.73
548	6.3	9.3	3.0	0.67
602	4.3	6.4	2.1	0.67
616	2.6	4.1	1.5	0.63
624	3.6	4.9	1.3	0.73
646	4.3	6.0	1.7	0.71
648	6.7	9.3	2.6	0.72
657	4.9	7.5	2.6	0.65

Table 6-8: Magnitude of force signal of the deeply submerged rudder
Cases that are well predicted

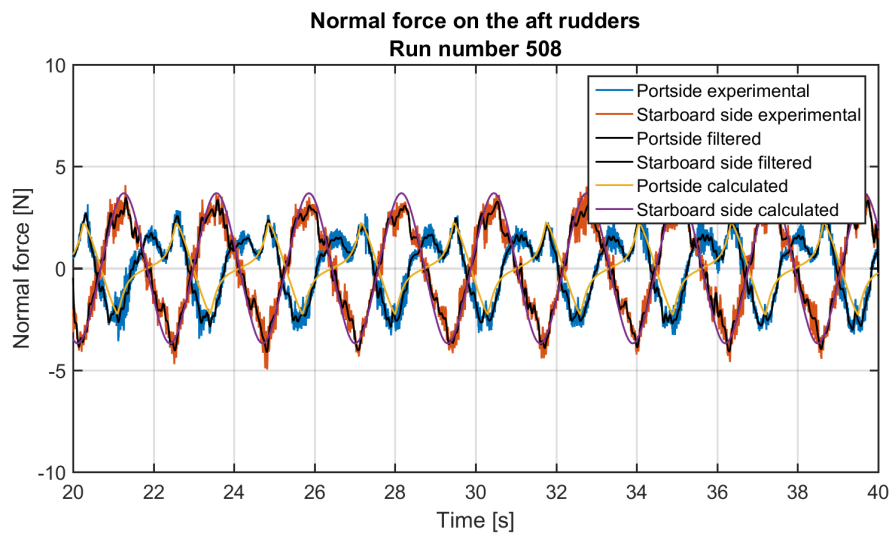
Run number	Measured signal [N]	Calculated signal [N]	Δ [N]	Fraction
508	3.5	3.7	0.2	0.94
530	3.4	3.9	0.5	0.87
532	5.5	6.1	0.6	0.90
540	3.4	3.9	0.5	0.87
542	5.4	6.1	0.6	0.88
608	3.0	3.7	0.7	0.81
636	3.8	4.5	0.7	0.84
642	5.0	6.0	1.0	0.83

constant fractional deviation is found for the different experiments. The deviation is however much smaller than in the cases from Table 6-7.

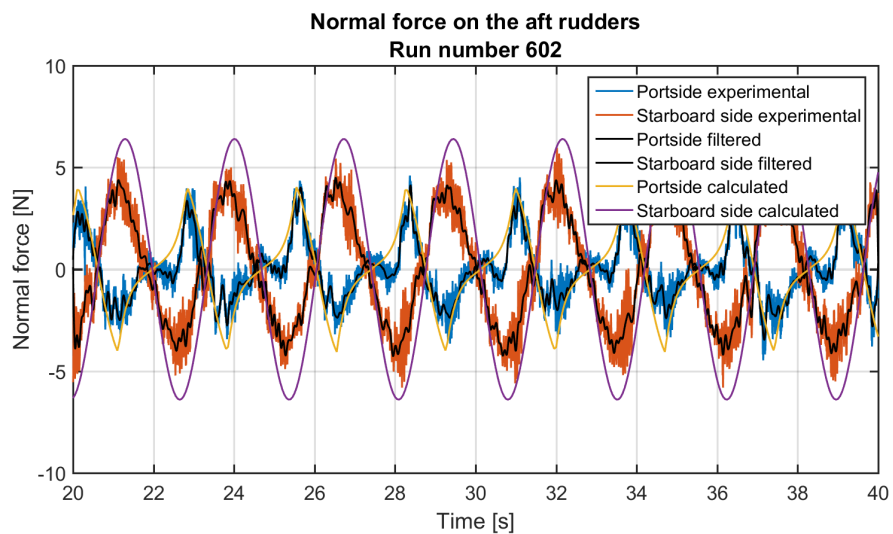
In the cases of the horizontal rudders in +-configuration, the behaviour of the calculated solution is quite similar to that of the bowplanes. The signal magnitude is slightly lower than the measured signal magnitude, but only marginally.

In the case of the vertical rudders in +-configuration, the same trend as for the large X-configuration is visible: the magnitude of the signal of the deeply submerged rudder is overestimated when the angles of attack are lower (i.e.: when the rudder is less heavily loaded).

For the small X-configuration a significant deviation in magnitude of the deeply submerged rudder is found (see Figure 6-4). The calculated result is nearly three times as high as the measured result. The lift curve slope is clearly significantly overestimated.



(a) Large X-configuration
 $V = 0.63 \text{ m/s}$, $\varphi_A = 30^\circ$, $\omega = 2.798 \text{ rad/s}$



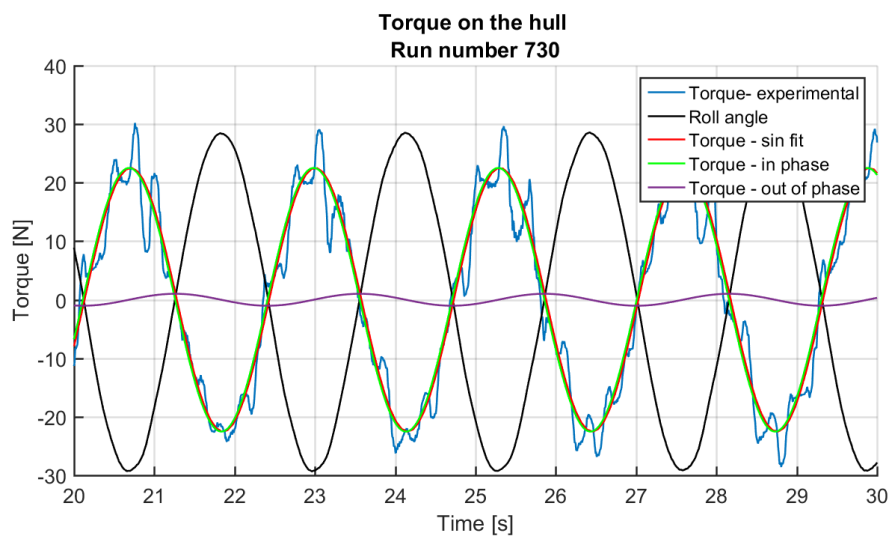
(b) Large X-configuration
 $V = 1.26 \text{ m/s}$, $\varphi_A = 30^\circ$, $\omega = 2.368 \text{ rad/s}$

Figure 6-7: Comparison of measured and calculated force signals, large X-configuration

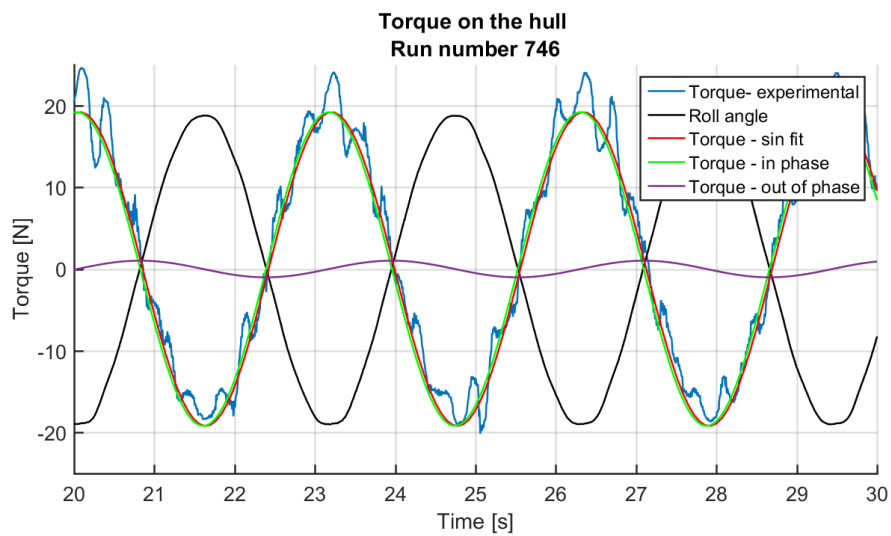
6-4 Bare hull

In Chapter 2 and Chapter 3 it was assumed that by far the greatest contribution to the roll damping was due to the normal forces experienced by the rudders. To investigate the validity of this assumption, a number of experiments without any rudders have been performed. According to the theory of Chapter 2, any roll damping that is present is caused by skin friction. The roll damping can be derived from the phase difference between the torque signal and the roll motion.

Figure 6-8 shows the typical torque signals for the bare hull. Figure 6-8a is a case where higher damping is expected due to the larger roll motion, while Figure 6-8b represents a case with a smaller, slower roll motion. A sine function has been fitted through the torque signals. The sine function has been split into two functions, one in phase and one out of phase with the motion, all according to Section 5-8. The out of phase signal represents the damping.



(a) $V = 1.26 \text{ m/s}$, $\varphi_A = 30^\circ$, $\omega = 2.798 \text{ rad/s}$



(b) $V = 0.63 \text{ m/s}$, $\varphi_A = 20^\circ$, $\omega = 2.052 \text{ rad/s}$

Figure 6-8: Torque signal for the hull without rudders

Chapter 7

Conclusions

In this chapter, conclusions will be drawn based on the results discussed in the previous chapter. The research question introduced in Chapter 1 will be answered and some recommendations for further research will be given.

7-1 Conclusions

To answer the research question, a mathematical model has been developed to predict the roll damping of a sailing surfaced submarine. Experiments have been performed to validate the model. A fair amount of assumptions have been made in the model, some of which could be considered to be bold ones. It was assumed that the rudders behaved as wings and that the generation of lift could be predicted by thin airfoil theory. Also, it was assumed that the circulation over the rudders was elliptical, which is clearly not the case. Even with these major assumptions, the model gave a more than fair prediction of the experimental results. More complicated signals, such as the surface piercing rudders of the large X-configuration, were predicted well.

Overall, it can be concluded that the mathematical model predicts the damping force generated by the rudders well. The forces generated by the bowplanes and horizontal rudders in the +-configuration are predicted very well. The surface piercing rudders of the large X-configuration are predicted well.

The prediction of the normal force experienced by the deeply submerged rudders proved most difficult. In the cases where the rudder is heavily loaded, right up to the point of stall, the prediction is accurate. For lower angles of attack the prediction is too large by a factor 1.5. This factor seems to be consistent. Further investigations into this change of the lift curve slope is recommended. However, since all deeply submerged rudders have this phenomenon, a qualitative comparison between the different rudder configurations is still possible. The quantitative result may be in doubt, the qualitative trend is right.

In Chapter 1 the following research question was posted:

Which rudder configuration provides the most roll damping for a surfaced submarine at speed?

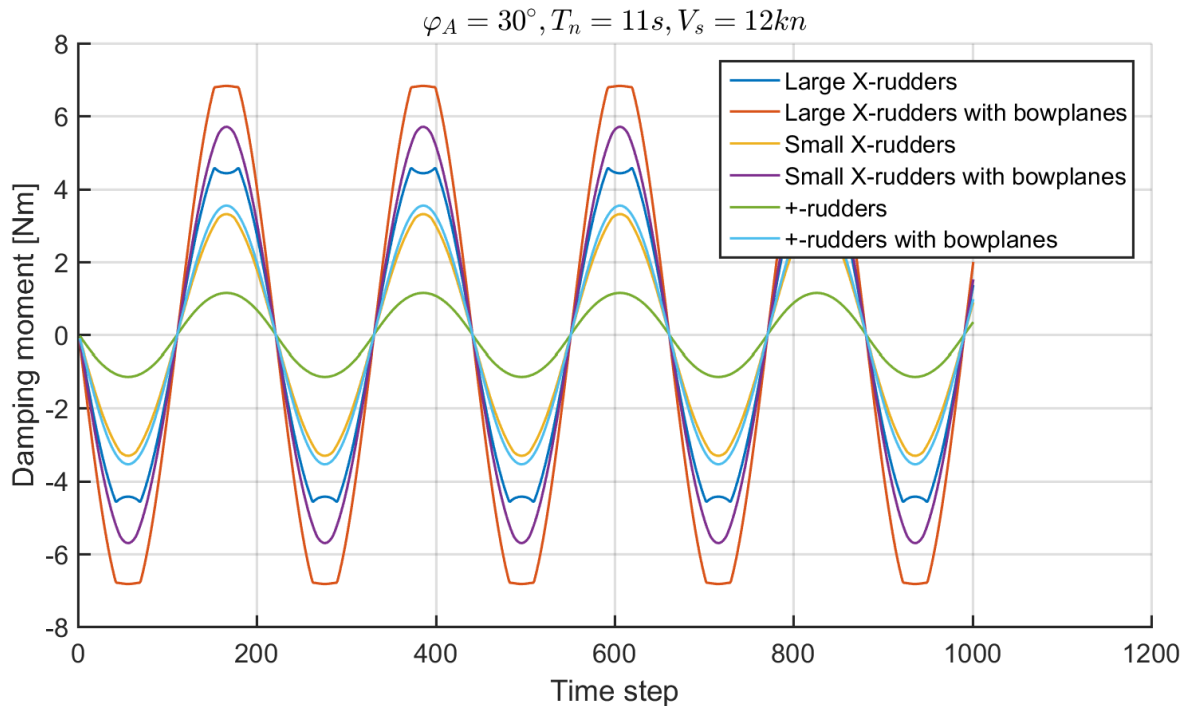


Figure 7-1: Damping moment for six different rudder configurations. Note the flattened tops for the configuration with large X-rudders. This is caused by the stalling of the rudder tips.

Now, with the help of the mathematical model, this question is answered. For every combination of velocity, roll angle and roll frequency, the same qualitative result was obtained, of which an example is shown in Figure 7-1. The larger the rudder area, the larger the damping moment. The addition of bowplanes always significantly increases the damping moment. As such, the large X-configuration with bowplanes provides the largest roll damping moment to the submarine.

To check the assumption that the hull indeed causes little to no damping, the torque signals of the bare hull measurements were studied. These torque measurements proved troublesome. As can be seen in Figure 5-8b, the torque signal was often disturbed by the not purely sinusoidal motion imposed by the drive motor. These disturbances impede the fitting of a sine function through the signals, which is necessary to determine the part of the signal that is out of phase with the roll motion. The signals of two cases where the disturbance was limited are shown in Figure 6-8. It can be seen that the phase shift is very small. Hence, the damping is very small and it can be concluded that the hull generates hardly any roll damping.

7-2 Recommendations for further research

Over the course of this research, new questions arose that deserve further research. Also, a few things were noticed that could be improved if this research is repeated or similar research is to be performed in the future.

The mathematical model takes, as of now, only the out of phase forces into account. The experiments have shown that in certain cases significant in phase forces occur. Although this

in phase part does not influence the actual roll damping of the submarine, it would help to gain a better understanding of the forces that are generated by the rudders.

This research focussed on the damping moment of a surfaced, sailing submarine. A large roll damping is indeed required to reduce the roll motion. This research skipped over the excitation of the roll motion however. Excitation of the rudders by, for instance, the waves may have a significant influence on the actual roll motion of the submarine. The influence of the rudder configuration on the excitation in roll would be an interesting area for further research.

The most difficult part of the model is the determination of the lift curve slope to be used in the calculations. As was stated in Chapter 6, the lift curve slope for low angles of attack for deeply submerged rudders seems to differ from the lift curve slope for larger angles of attack. The phenomenon that causes this change in angle of attack is as of yet unknown. Further research to this change in lift curve slope is thus recommended.

As far as the experiments are concerned, the usable experimental data would be significantly increased if force sensors with a smaller range are used. Now, too many experiments resulted in unusable data because the force amplitude was too low.

Finally, disturbances in the experiments could be further decreased if a different drive mechanism was used to force the motion. Instead of an oscillating drive, it might be better to use a continuously rotating motor. The reversing of the linear drive, together with the required PID-controller caused disturbances in the measurements. By eliminating the need for a PID-controller, a better motion can be forced on the model, thus reducing unwanted frequencies in the measurements.

Appendix A

Sonar flankarrays

Submarines are generally equipped with sonar arrays over the length of the submarine. These so called flankarrays can either be mounted in the space between the pressure hull and the outer hull, creating a flush surface with the outer hull, or externally on the outer hull. Figure A-1 shows a sketch of these two possibilities. See also Figure 1-1 for a perspective view on a sonar flankarray. The protrusions of the hull of an externally mounted sonar flankarray may increase the roll damping of the submarine.

This chapter will investigate the effect of external flankarrays on the roll damping. The investigation is of a qualitative nature, meant to get the magnitude of the effect rather than the exact contribution to the roll damping.

A-1 Assumptions

For the purpose of this investigation, the following assumptions have been made with regard to the dimensions of externally mounted sonar flankarrays:

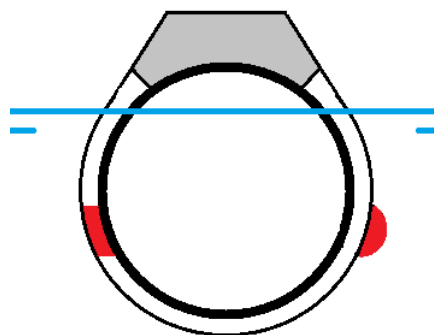


Figure A-1: Cross section of a submarine hull. Sonar flankarrays of two possible configurations are shown in red. On the left an internal flankarray, on the right an external flankarray with a streamlined shape.

- The length of the array is 30 m.
- The array has a semi-elliptic cross section. The radii of the cross section are 0.4 m and 0.8 m. The shorter radius is normal to the hull.
- The distance between the axis of roll and the flankarray is 2.3 m.
- The submarine rolls in its eigenperiod of 13 s.
- The roll amplitude is 40 degrees.
- The sonar flankarray is always submerged.

A-2 Calculations

Zero speed

With zero forward speed, the flankarray can only generate drag. The flow over the flankarray is equivalent to the flow over a two dimensional ellipse. Since the curvature of the outer hull is small when compared to the curvature of the flankarray, the outer hull functions as an endplate to the semi-circular cross section.

The drag coefficient of a 2D-elliptic cross section is given by White (2009) as 0.6 in the case of laminar flow. Hence, the total drag for one flankarray is approximated by:

$$D = C_D A \frac{1}{2} \rho v^2 \quad (\text{A-1})$$

With A the frontal area of the flankarray, ρ the density of the water and v the velocity. At zero forward speed, the velocity is only dependent on the roll period, the amplitude of roll and the distance from the flankarray to the axis of roll.

Calculating the result gives a total drag for both flankarrays combined of 1845 N.

Positive forward speed

At forward speed, the flankarrays will generate a lift force. Hoerner (1975) divides the lift for slender streamlined bodies in two components: circulatory lift and lift due to a cross flow over the body. Both components will be treated consecutively.

Circulatory lift The circulatory lift is caused by the circulation around the streamline body. Since the long slender bodies are inefficient in the generation of circulation, this lift force is necessarily small. Hoerner (1975) gives a maximum value for the change in the lift coefficient:

$$\frac{dC_L}{d\alpha} = 0.0274$$

However, he also refers to evidence that a correction should be applied for the growth of the boundary layer over the aft body. He proposes the following correction:

$$\Delta \frac{dC_L}{d\alpha} = (0.0001 \text{ to } 0.0002) \sqrt{l/d} \quad (\text{A-2})$$

For the flankarrays, with length of 30 m and diameter of 0.4 m this results in a correction of:

$$\Delta \frac{dC_L}{d\alpha} = 0.0013$$

At a forward speed of 12 knots, this results in a lift force of:

$$L = \frac{1}{2} \rho v^2 \left(\frac{dC_L}{d\alpha} + \Delta \frac{dC_L}{d\alpha} \right) \alpha d^2 \quad (\text{A-3})$$

Which equates to a lift force of 832 N for both flankarrays combined.

Cross flow force A certain amount of lift is generated by the cross flow over the streamline body that is placed at an angle of attack. This lift results from a pressure difference between upper and lower side of the streamline body as a result of the viscous flow crossing over from the lower to the upper side. Hoerner (1975) gives a description of the lift force arising from cross flow. The cross flow force is dependent on the so called cross flow coefficient C_C , which is equal to the drag coefficient C_D for a cylinder aligned perpendicular to the flow. Based on this coefficient, Hoerner (1975) defines both the lift and drag coefficient of a cylinder at an angle of attack to the flow:

$$C_D = C_C \sin^3(\alpha) \quad (\text{A-4})$$

$$C_L = C_C \sin^2(\alpha) \cos(\alpha) \quad (\text{A-5})$$

Where α is the angle of attack of the flow with the cylinder. For the flankarrays combined this results in a lift force of 606 N.

Conclusion

The flankarrays of a submarine will generate an opposing moment to the rolling motion. Two cases have been investigated, using conservative approaches. In the case of zero forward speed, the only opposing force is a drag force. This drag force is 1845 N and creates an opposing moment of 8.5 kNm.

With forward speed, lift forces are created. The total lift force generated equals 1438 N at a forward speed of 12 knots. This equals an opposing moment of 6.6 kNm.

The reduction in moment at forward speed is a consequence of the changing flow. The flow was assumed to be laminar at zero forward speed. At 12 knots however, the flow becomes turbulent and turbulent flow has a much lower drag coefficient for elliptic cylinders (0.2 rather than 0.6 (White, 2009)).

The resulting roll opposing moment is small when compared to the moment that will be generated by the rudders and henceforth the effect of sonar flankarrays is deemed negligible.

Appendix B

Partial flooding of the casing

The casing is the superstructure of the submarine, that is build on top of the pressure hull. The casing provides a flat deck for the crew to work on. A very clear example of the casing is shown in Figure B-1. The void space between the casing and the pressure hull is flooded when the submarine is submerged. Upon surfacing, water leaves the casing through a number of flood gates. See for instance Figure B-2. However, in the case of severe rolling, water can enter the casing through the flood gates. Water trapped in the casing may trigger free-surface effects, causing instability, and raises the center of gravity, thus reducing stability and altering the roll motion of the submarine.

This appendix will investigate the effect of partial flooding of the casing. Attention will be given to the amount of water trapped in the casing and the effects of that amount on the stability of the submarine. The investigation is meant to give a quick insight in the importance of this effect. As such, many factors have been excluded from this initial analysis. Section B-1 lists the assumptions made for this initial analysis.

B-1 Assumptions

As stated in the introduction of this appendix, the aim of this analysis is to give an initial estimate of the effects of water trapped in the casing. A number of assumptions have been made to make this quick analysis possible:

- Flooding gates are situated at the lowest points of the floodable part of the casing. All the water can leave the casing.
- There are no waves, nor is there a heave motion. Water can only enter the casing through the rolling motion of the submarine.



Figure B-1: USS Bowfin, a submarine from the second world war era, showing the casing in light grey on top of the pressure hull in dark grey. Interesting is also the folded bowplane just aft of the anchor.

Source: [https://en.wikipedia.org/wiki/Casing_\(submarine\)](https://en.wikipedia.org/wiki/Casing_(submarine)) (accessed on May 12, 2016)



Figure B-2: Flood gates of a surfaced submarine. Water can be seen to escape through the port flood gates (inside the red ellipsis).

Source: <http://www.rdm-archief.nl/RDM-NB/RDM-320.htm> (accessed April 7, 2015)

- The casing is modelled as a prismatic tank with constant rectangular cross section. The dimensions of this tank are:
 - $L = 42$ m
 - $B = 4.5$ m
- When in upright condition, the floodgates are 0.65 m above the waterline.
- The cross sectional area of the combined floodgates is 0.3 m^2
- The submarine rolls with a period of $T_n = 15$ s.
- The amplitude of the roll motion is 30 degrees.

B-2 Calculations

Water flowing into and out of the casing is based upon a pressure difference due to a difference in water levels inside and outside of the tank, see Figure B-3. The rate at which the water flows into the tank depends on the flow velocity at point 2. Apply Bernoulli's equation:

$$p_1 + \frac{1}{2}\rho v_1^2 + \rho g z_1 = p_2 + \frac{1}{2}\rho v_2^2 + \rho g z_2 \quad (\text{B-1})$$

Due to ventilation of the tank at the top, p_1 and p_2 both equal to p_0 , the atmospheric pressure. Assuming that point 1 is chosen at a sufficiently large distance from the flood gate, the velocity at point 1 can be considered zero. Hence the equation reduces to:

$$\rho g z_1 = \frac{1}{2}\rho v_2^2 + \rho g z_2 \quad (\text{B-2})$$

Or, after rewriting and dropping the density:

$$v_2 = \text{sgn}(z_1 - z_2) \sqrt{2g |z_1 - z_2|} \quad (\text{B-3})$$

The volume flow equals:

$$\dot{V} = v_2 \cdot A_{\text{flood gates}} \cdot C_d \cdot dt \quad (\text{B-4})$$

Where C_d is the so called discharge coefficient, which accounts for loss effects due to the viscous flow of the water through the flood gate. Several values for the discharge coefficient are given: van Slooten (2014) gives a value of 0.37, while on the other hand Ruponen (2007) cites a research by Vassalos et al. (1997), stating that a value of 0.6 is a good approximation for (damage) openings.

The new volume of water in the tank is equal to the previous volume plus the volume flow over the time interval:

$$V^{n+1} = V^n + \dot{V}^n dt = V^n + v_2 \cdot A_{\text{flood gates}} \cdot C_d \cdot dt \quad (\text{B-5})$$

The variable z_2 can be expressed as a function of the known volume of fluid and the rolling angle φ :

$$z_2 = \sqrt{\frac{2V^n/L_t}{\sin \varphi \cos \varphi}} \sin \varphi \cos \varphi \quad (\text{B-6})$$

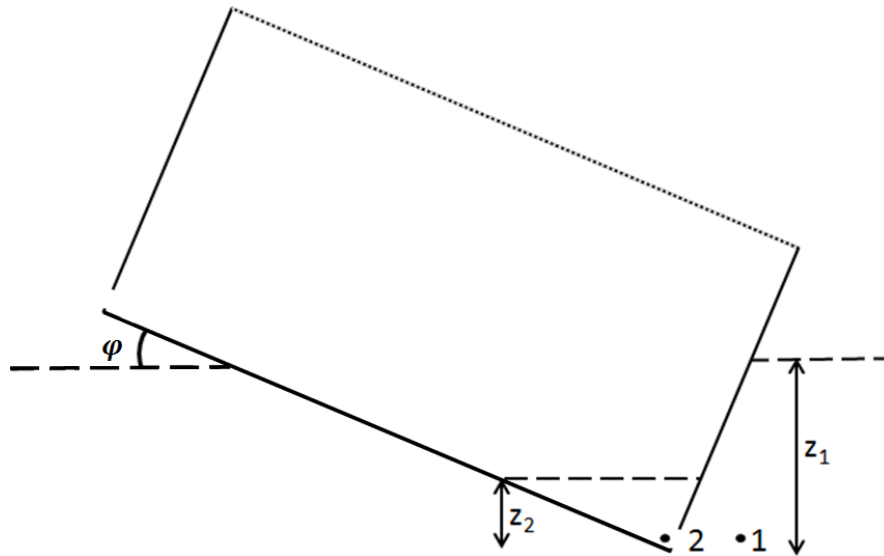


Figure B-3: The modelled tank. The top side of the tank is ventilated to the outside. Outside, respectively inside water levels are indicated by z_1 and z_2

Where L_t is the length of the tank. Applying Eq. (B-3), Eq. (B-4), Eq. (B-5) and Eq. (B-6) to a known sinusoidal roll motion results in the volume of water in the casing over time. Figure B-4 shows the volume of water in the casing when the discharge coefficient is set to 0.6 (Ruponen, 2007). Over time, the volume of water converges to 3 m^3 , which is equivalent to a layer of 1.6 cm over the bottom of the tank or an increase of 0.1 % of the displacement of the submarine. If the even lower discharge coefficient of 0.37 is chosen (van Slooten, 2014), even less water is entrained in the casing: 1.3 m^3 , equalling a layer of only 0.8 cm or an increase of 0.05 % in the surfaced displacement of the submarine.

B-3 Conclusion

A large rolling motion will cause the casing of the submarine to be partially filled with water. The water enters the casing through the flood gates, that are needed to drain the casing and the sail from water after surfacing the submarine. The amount of water in the casing converges to a mean value, which is dependent on the discharge coefficient C_d .

The calculations here are conservative. The tank is assumed to be a rectangular prism without any internal structure hampering the flow of water. The more realistic cross section is shown in Figure A-1. The casing is certainly not rectangular. Rather, the curvature of the pressure hull in combination with any internal structure reduces the free surface effects of water in the casing.

Even with the conservative estimate of the discharge coefficient, only a limited amount of water enters the casing. This amount is considered to be small enough to be neglected.

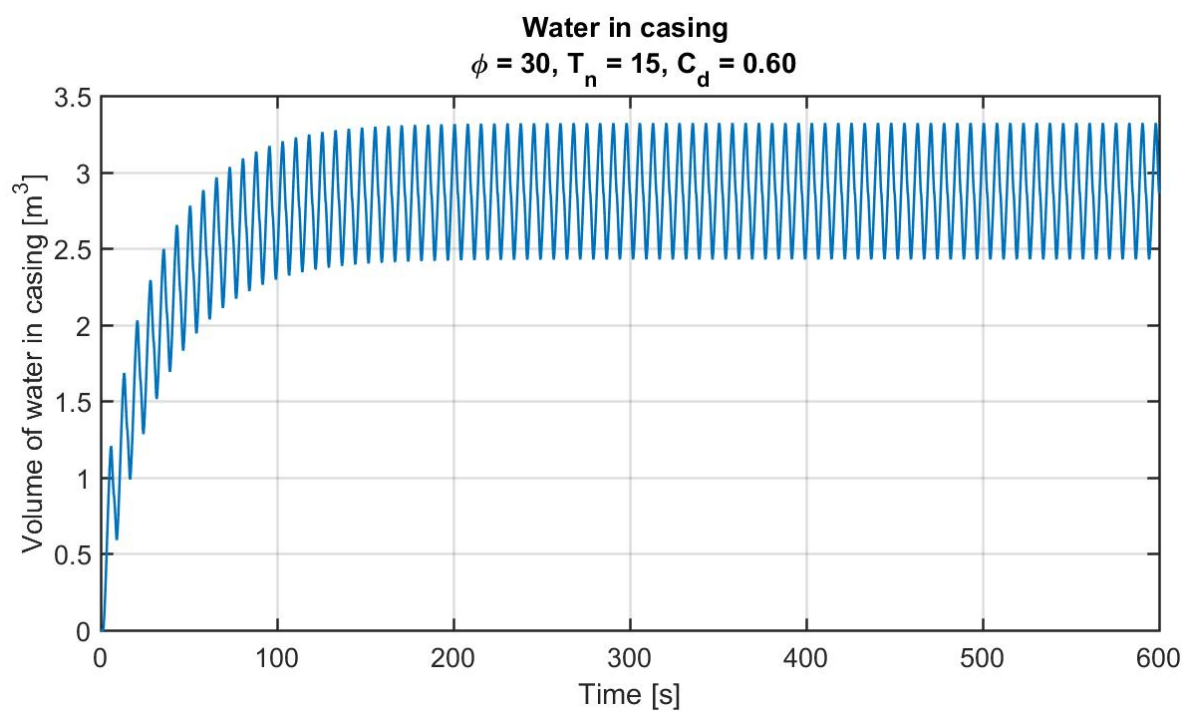


Figure B-4: The volume of water in the tank as a function of time.

Appendix C

Lift coefficients of the NACA 0018 foil

The lift coefficients of the NACA 0018 foilsection are presented in this appendix. The two dimensional coefficients are determined experimentally by Sheldahl and Klimas (1981). Table C-1 shows the two-dimensional lift coefficients for a Reynolds number of $5 \cdot 10^6$ and up to an angle of attack of 50 degrees. For higher angles of attack or other Reynolds numbers, the reader is referred to the paper of Sheldahl and Klimas (1981).

The three-dimensional lift coefficients are derived from the two-dimensional coefficients by assuming that the correction for three dimensional flow conditions, as given in Eq. (3-5), is valid for all angles of attack.

Table C-1: The 2D and 3D lift coefficients of the NACA 0018 at $Re = 5 \cdot 10^6$. The 3D lift coefficients correspond to a wing with an effective aspect ratio of 2.57 (i.e.: an X-rudder).

Angle of attack degrees	2D lift coefficient	3D lift coefficient
0	0.023	0.013
2	0.162	0.091
4	0.359	0.202
6	0.562	0.316
8	0.768	0.432
10	0.883	0.496
12	0.944	0.531
14	1.003	0.564
14.5	1.014	0.570
15	1.025	0.576
15.5	0.805	0.453
16	0.426	0.240
18	0.495	0.278
20	0.570	0.321
22	0.609	0.343
24	0.645	0.362
26	0.678	0.381
28	0.728	0.409
30	0.772	0.434
32	0.821	0.462
34	0.858	0.482
36	0.868	0.488
37	0.879	0.494
38	0.876	0.493
39	0.833	0.469
40	0.547	0.308
42	0.563	0.316
44	0.559	0.314
46	0.556	0.313
48	0.553	0.311
50	0.55	0.309

Appendix D

Experimental results

This chapter contains all the results from the experiments. The results are shown as time traces of the signals of the force sensors. Each time trace is complemented by the filtered signal and the corresponding result of the mathematical model. The filtered signal contains all frequencies below 10 Hz. This filter frequency corresponds to the 3 dB reduction point of the analogue filter used in the experimental set-up. It is believed that frequency components higher than 10 Hz are more a matter of noise than an actual response of the sensor. Therefore, these frequencies are removed.

The results of the bowplanes and the aft rudders are reported in separate sections.

D-1 Bowplanes

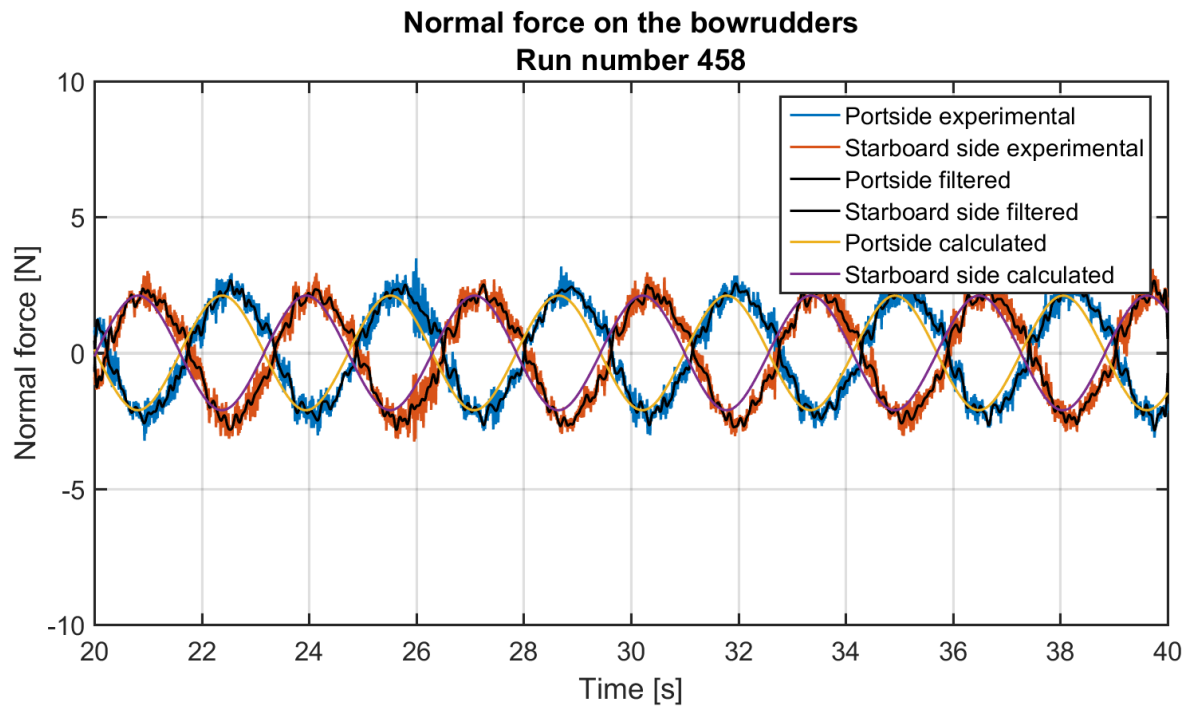


Figure D-1: large X-configuration
 $V = 0.84 \text{ m/s}$, $\varphi_A = 30^\circ$, $\omega = 2.052 \text{ rad/s}$

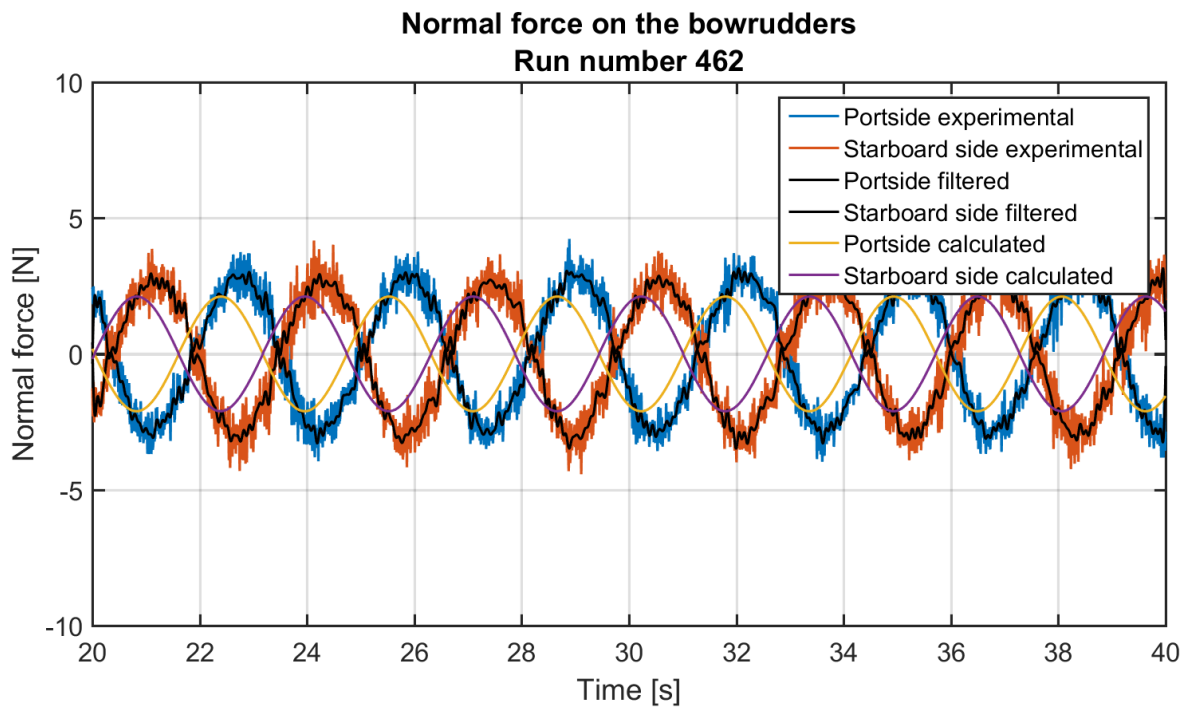


Figure D-2: large X-configuration
 $V = 1.26 \text{ m/s}$, $\varphi_A = 20^\circ$, $\omega = 2.052 \text{ rad/s}$

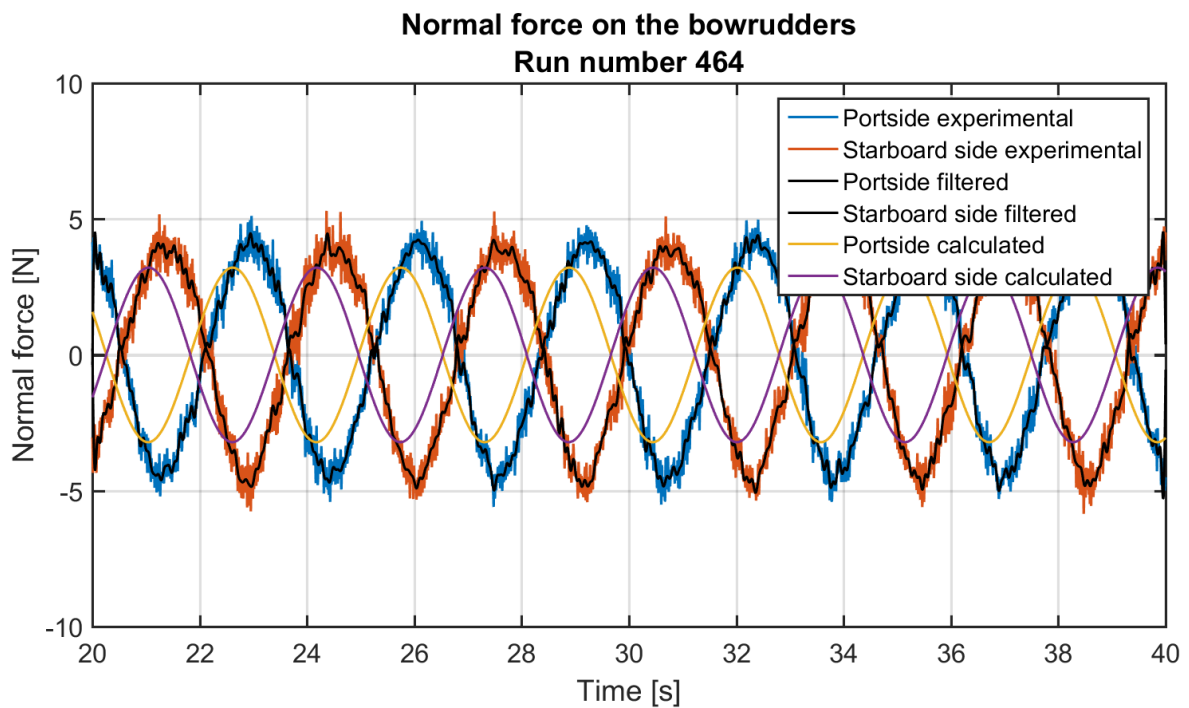


Figure D-3: large X-configuration
 $V = 1.26 \text{ m/s}$, $\varphi_A = 30^\circ$, $\omega = 2.052 \text{ rad/s}$

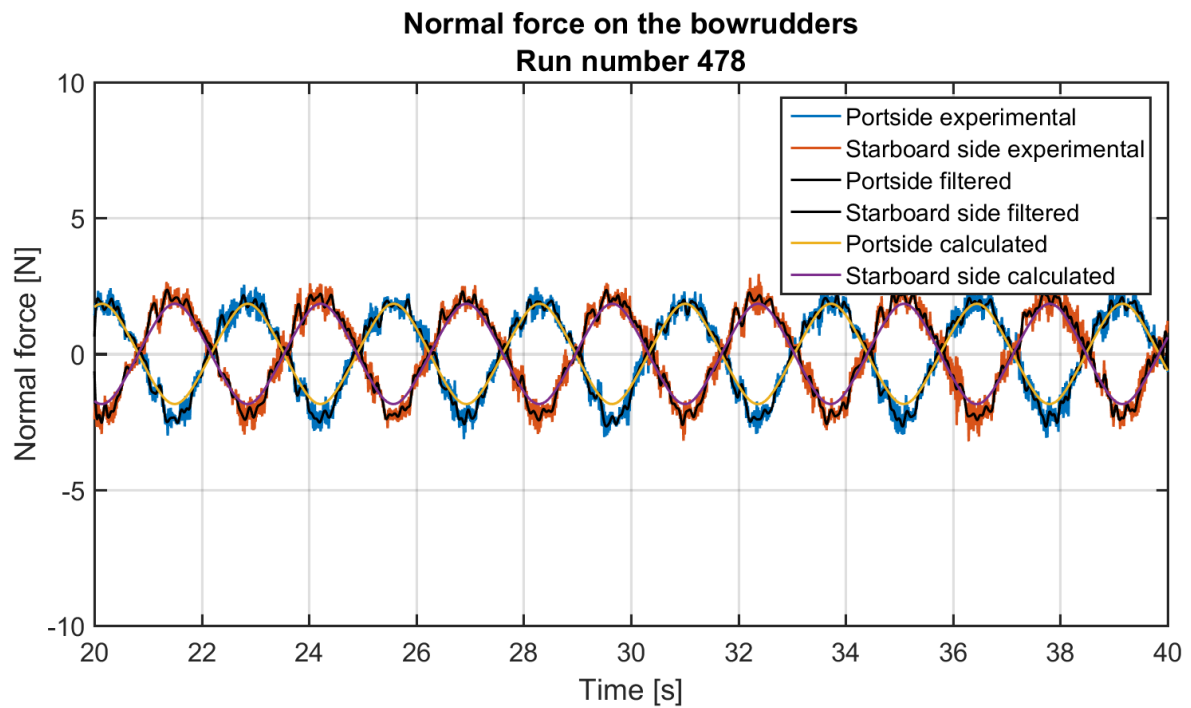


Figure D-4: large X-configuration
 $V = 0.63 \text{ m/s}$, $\varphi_A = 30^\circ$, $\omega = 2.368 \text{ rad/s}$

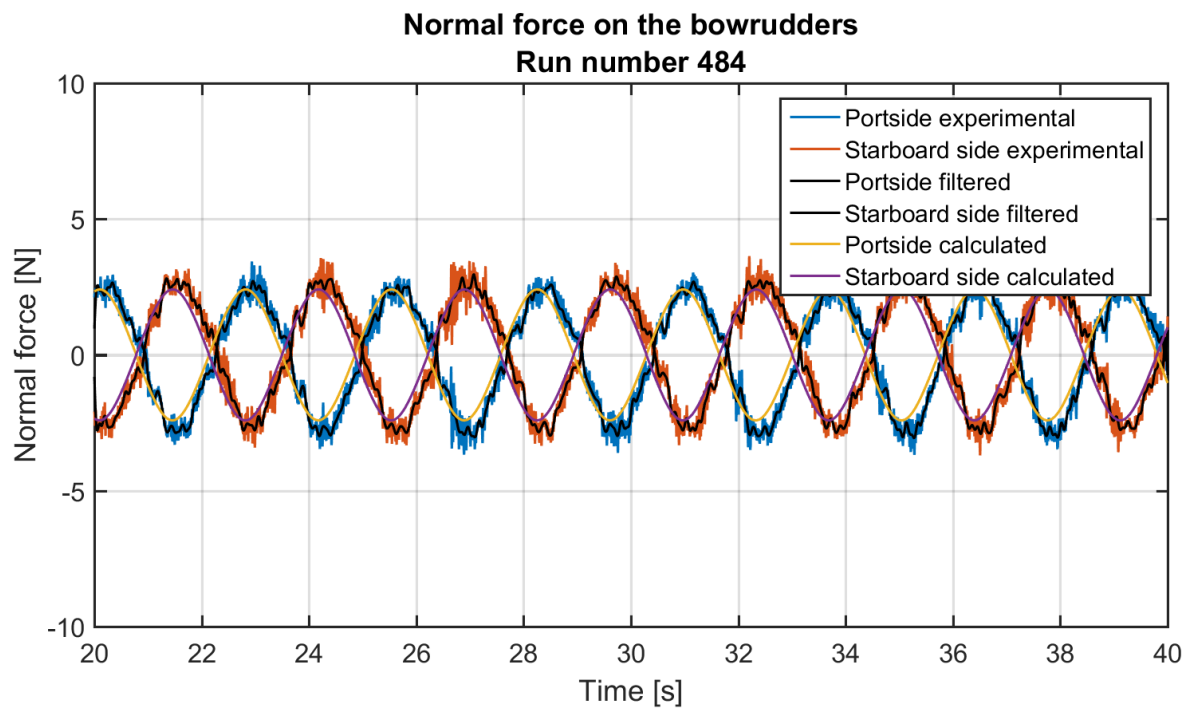


Figure D-5: large X-configuration
 $V = 0.84 \text{ m/s}$, $\varphi_A = 30^\circ$, $\omega = 2.368 \text{ rad/s}$

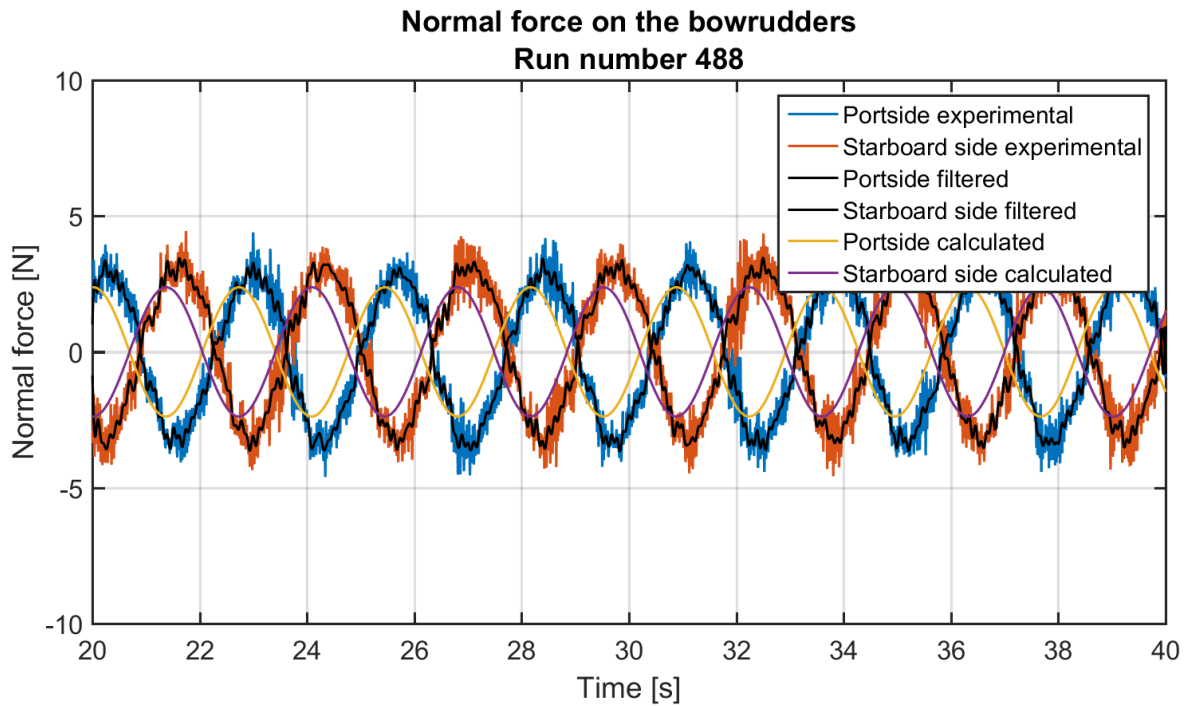


Figure D-6: large X-configuration
 $V = 1.26 \text{ m/s}$, $\varphi_A = 20^\circ$, $\omega = 2.368 \text{ rad/s}$

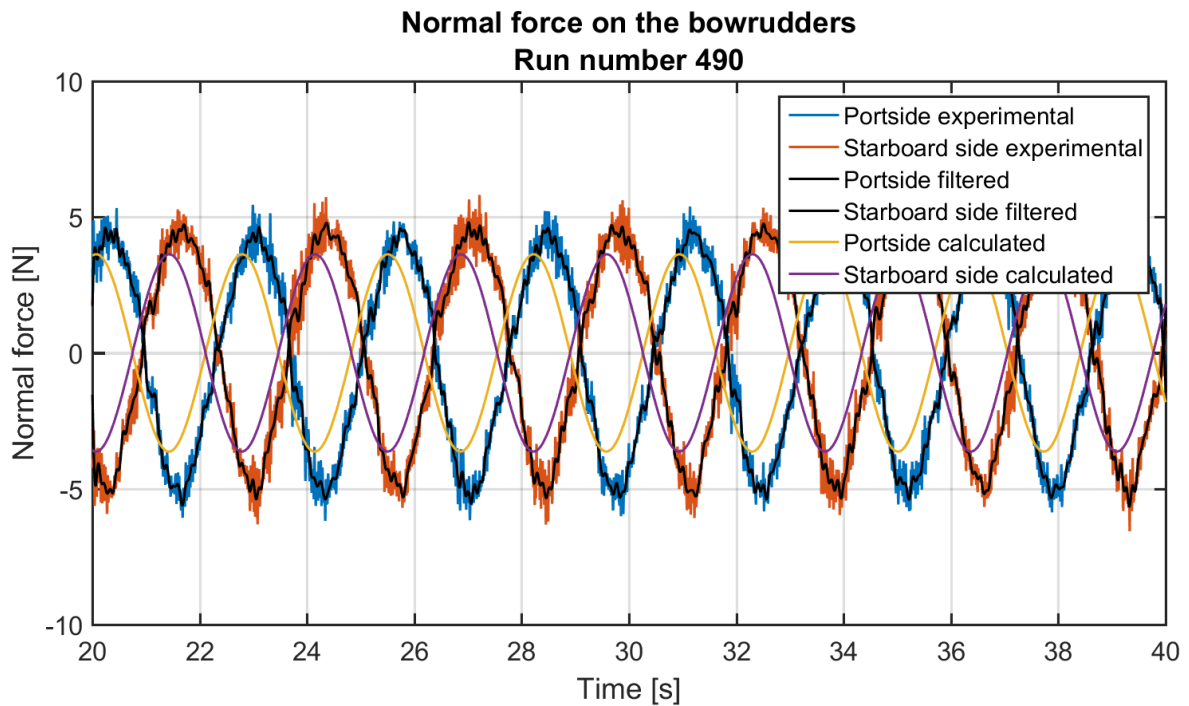


Figure D-7: large X-configuration
 $V = 1.26 \text{ m/s}$, $\varphi_A = 30^\circ$, $\omega = 2.368 \text{ rad/s}$

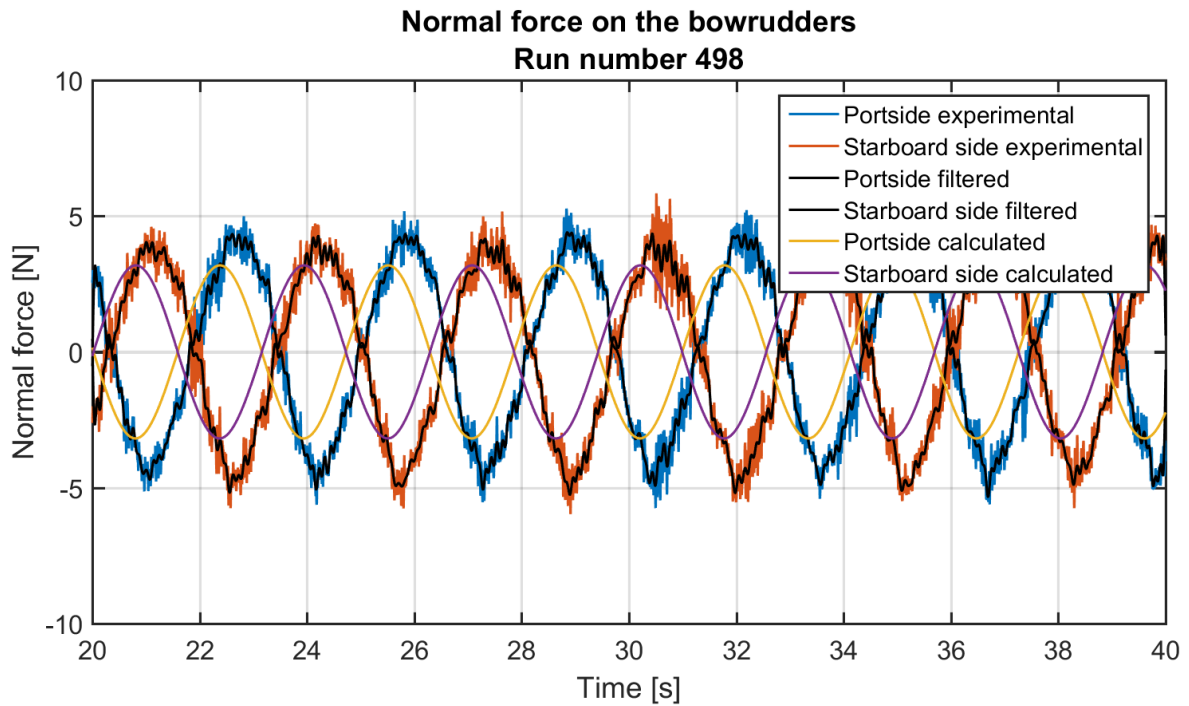


Figure D-8: large X-configuration
 $V = 0.84 \text{ m/s}$, $\varphi_A = 30^\circ$, $\omega = 2.798 \text{ rad/s}$

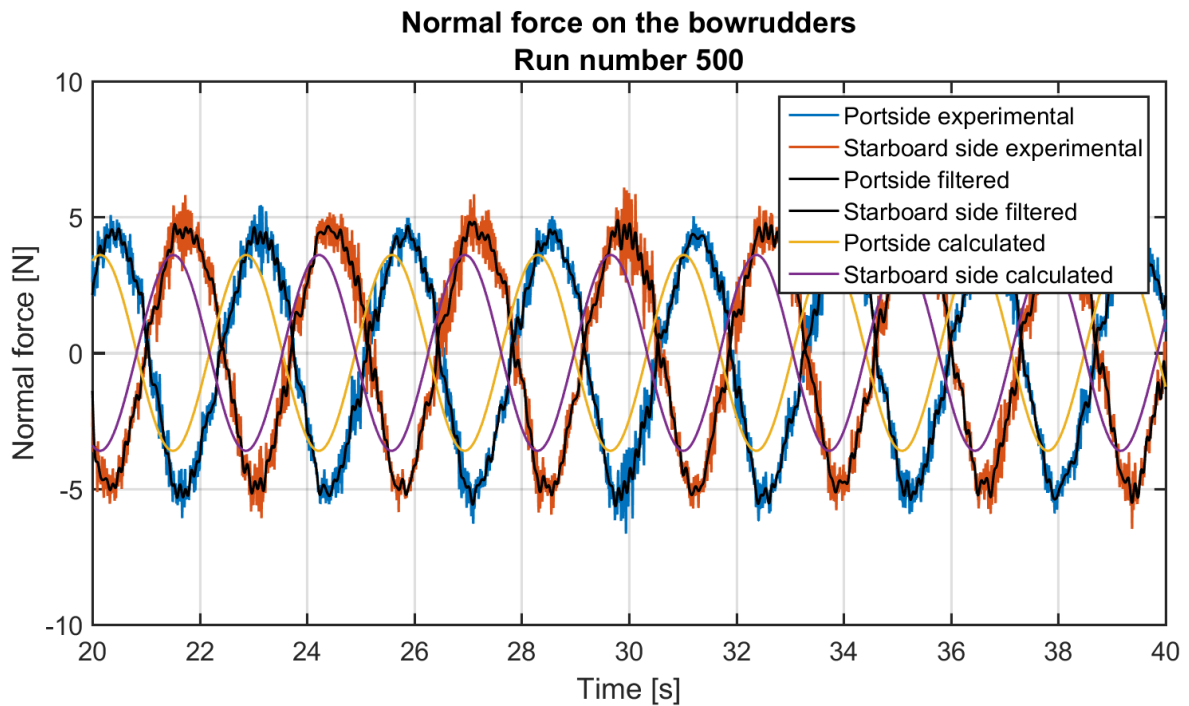


Figure D-9: large X-configuration
 $V = 0.84 \text{ m/s}$, $\varphi_A = 30^\circ$, $\omega = 2.798 \text{ rad/s}$

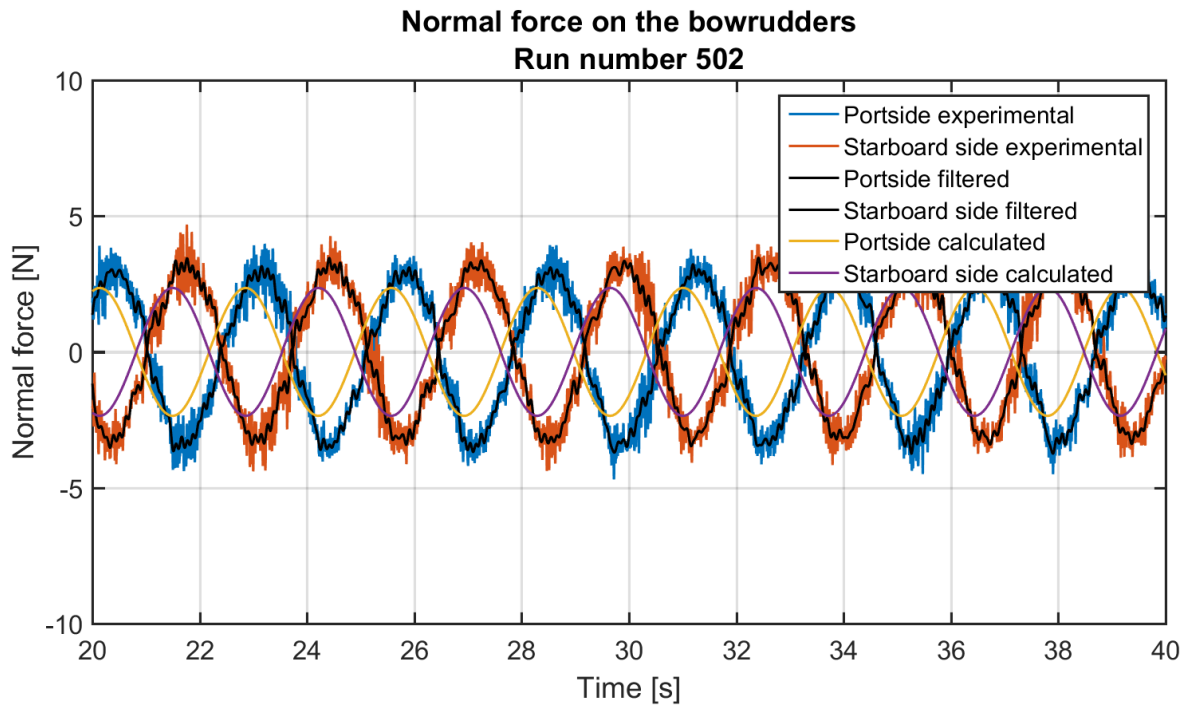


Figure D-10: large X-configuration
 $V = 1.26 \text{ m/s}$, $\varphi_A = 20^\circ$, $\omega = 2.368 \text{ rad/s}$

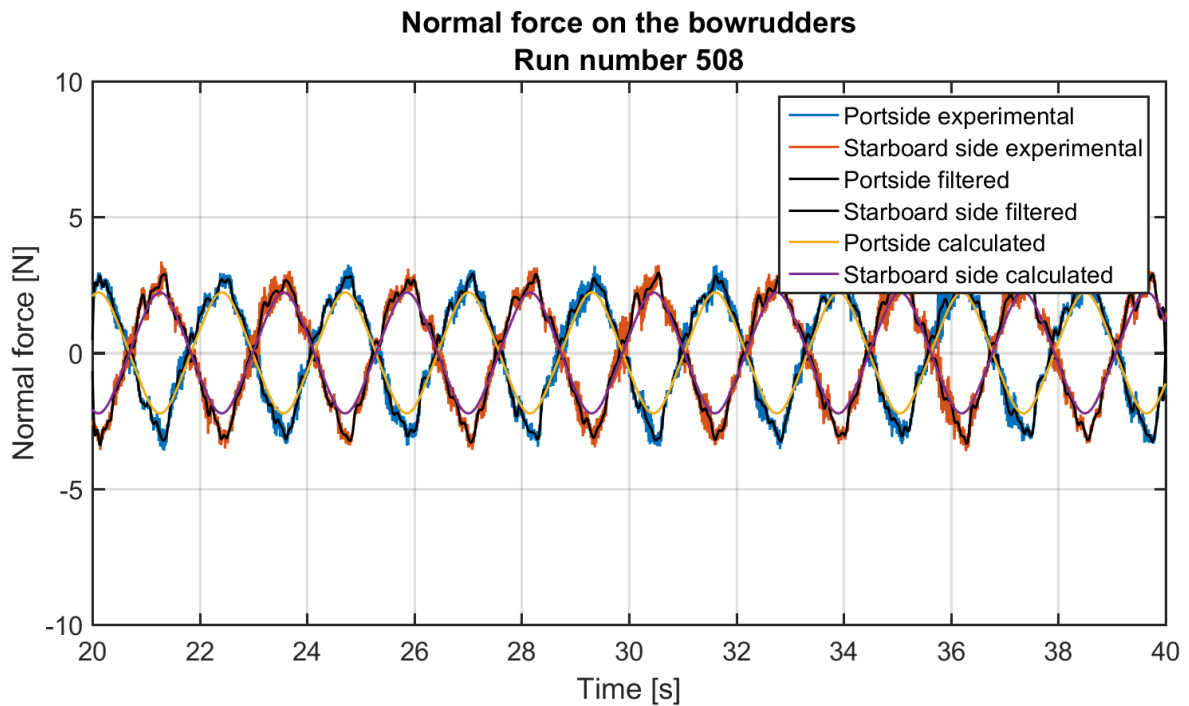


Figure D-11: large X-configuration
 $V = 0.63 \text{ m/s}$, $\varphi_A = 30^\circ$, $\omega = 2.798 \text{ rad/s}$

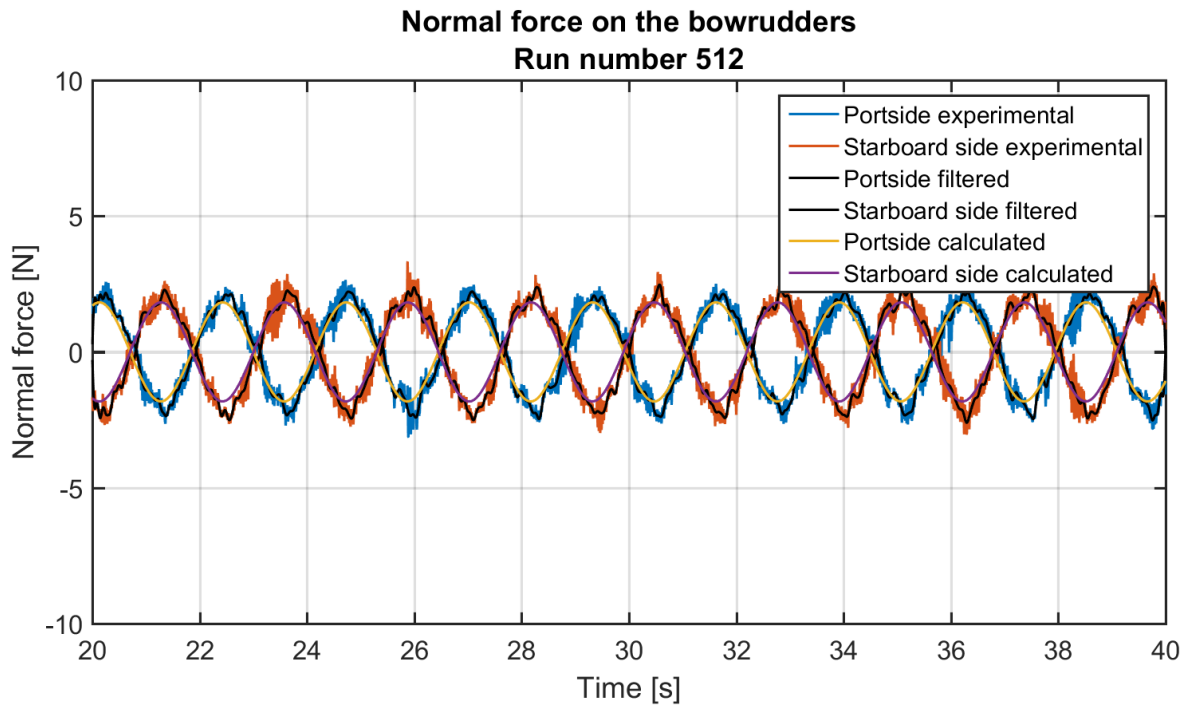


Figure D-12: large X-configuration
 $V = 0.84 \text{ m/s}$, $\varphi_A = 20^\circ$, $\omega = 2.798 \text{ rad/s}$

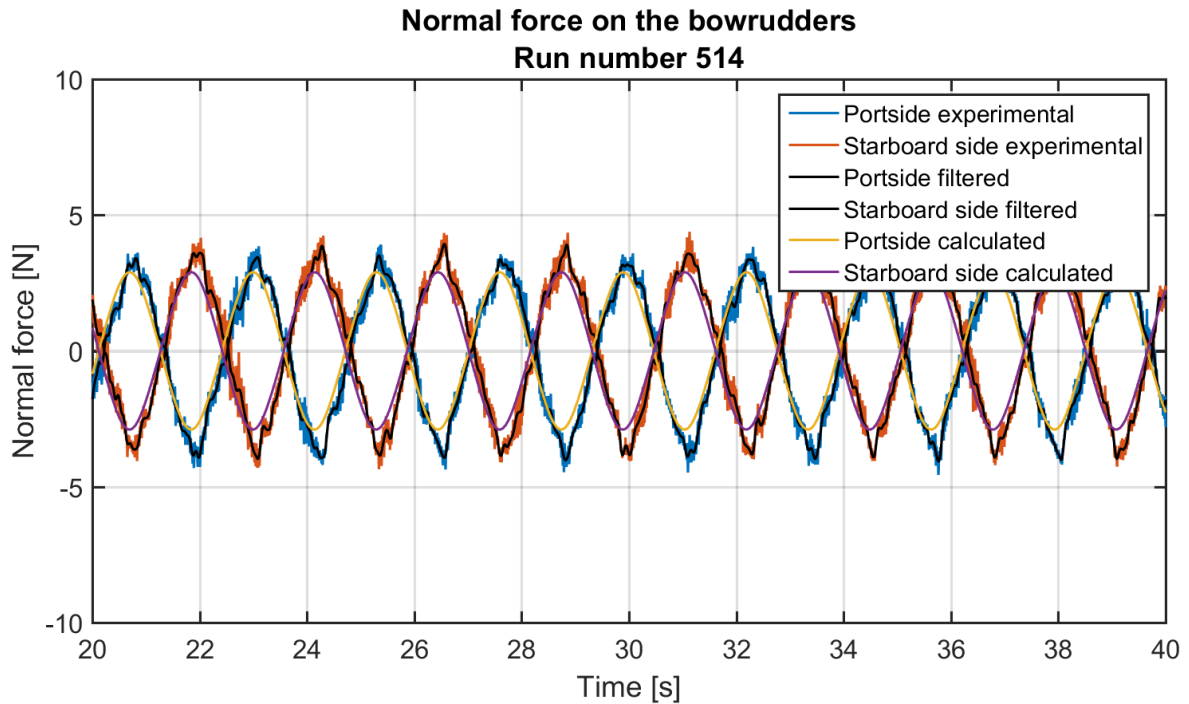


Figure D-13: large X-configuration
 $V = 0.84 \text{ m/s}$, $\varphi_A = 30^\circ$, $\omega = 2.798 \text{ rad/s}$

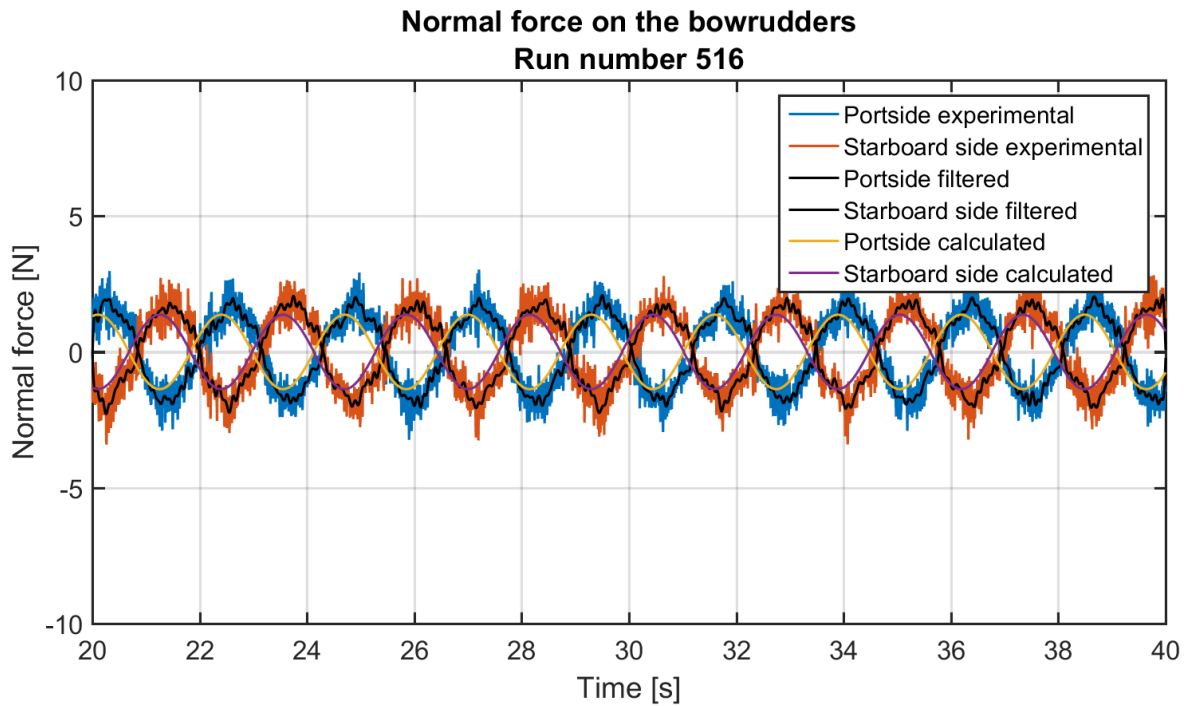


Figure D-14: large X-configuration
 $V = 1.26 \text{ m/s}$, $\varphi_A = 10^\circ$, $\omega = 2.798 \text{ rad/s}$

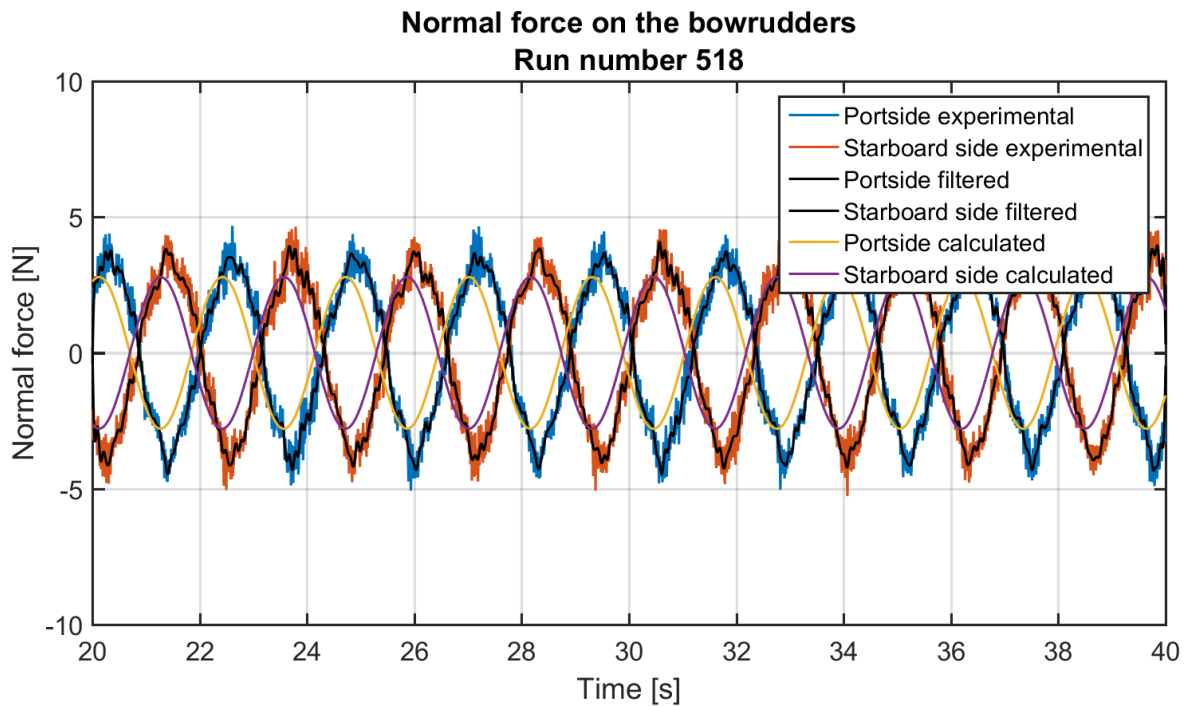


Figure D-15: large X-configuration
 $V = 1.26 \text{ m/s}$, $\varphi_A = 20^\circ$, $\omega = 2.798 \text{ rad/s}$

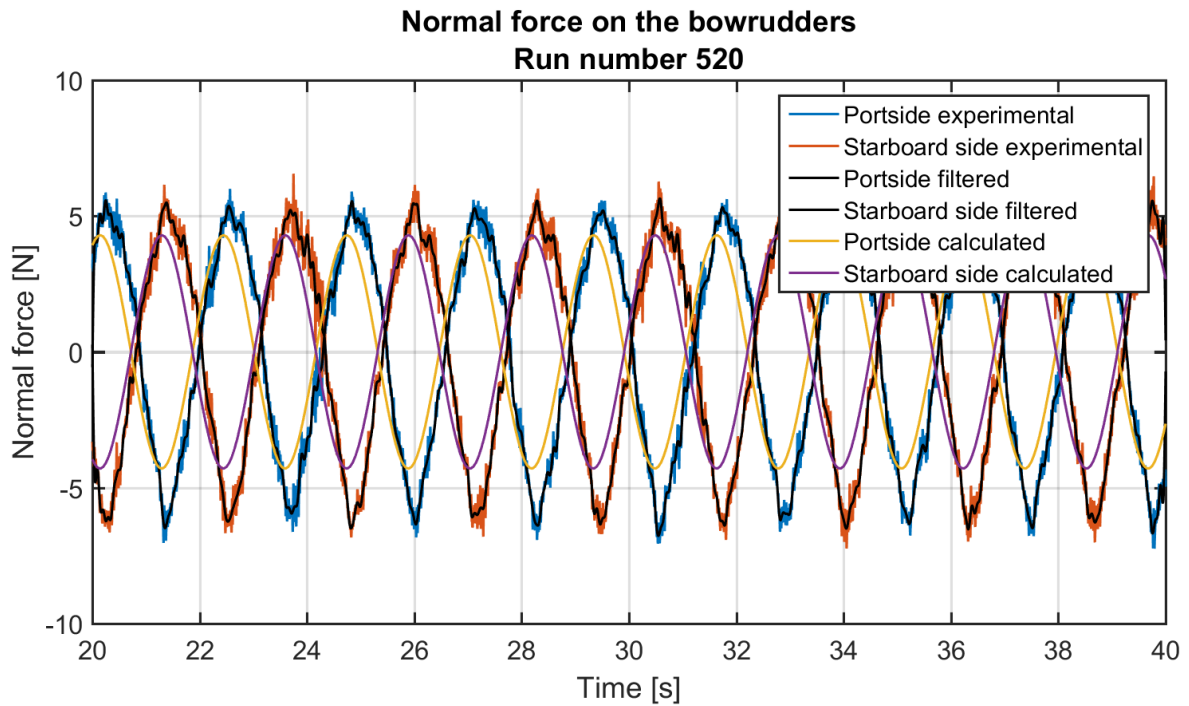


Figure D-16: large X-configuration
 $V = 1.26 \text{ m/s}$, $\varphi_A = 30^\circ$, $\omega = 2.798 \text{ rad/s}$

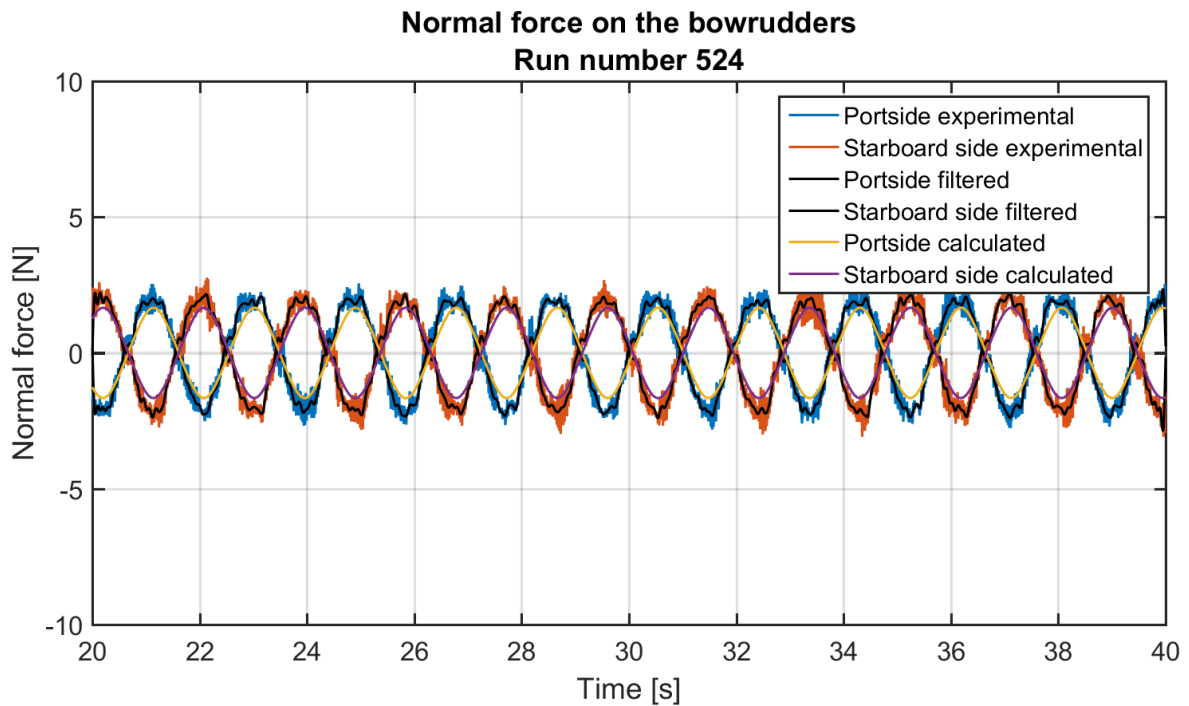


Figure D-17: large X-configuration
 $V = 0.63 \text{ m/s}$, $\varphi_A = 20^\circ$, $\omega = 3.420 \text{ rad/s}$

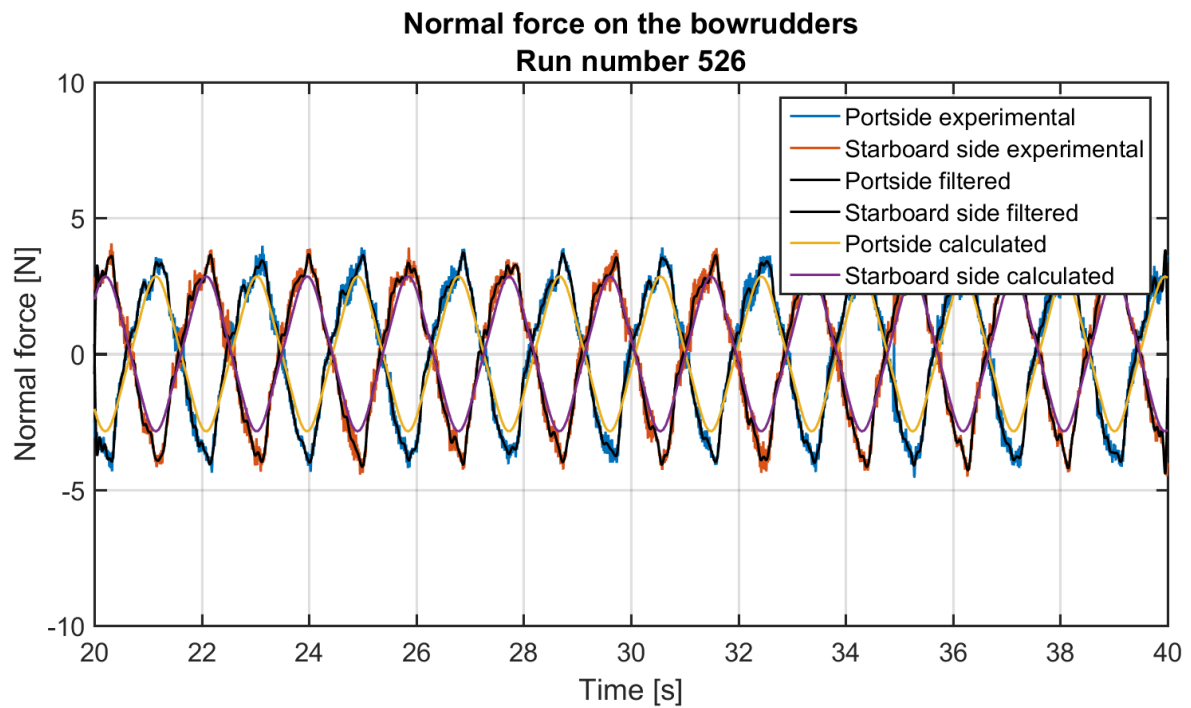


Figure D-18: large X-configuration
 $V = 0.63 \text{ m/s}$, $\varphi_A = 30^\circ$, $\omega = 3.420 \text{ rad/s}$

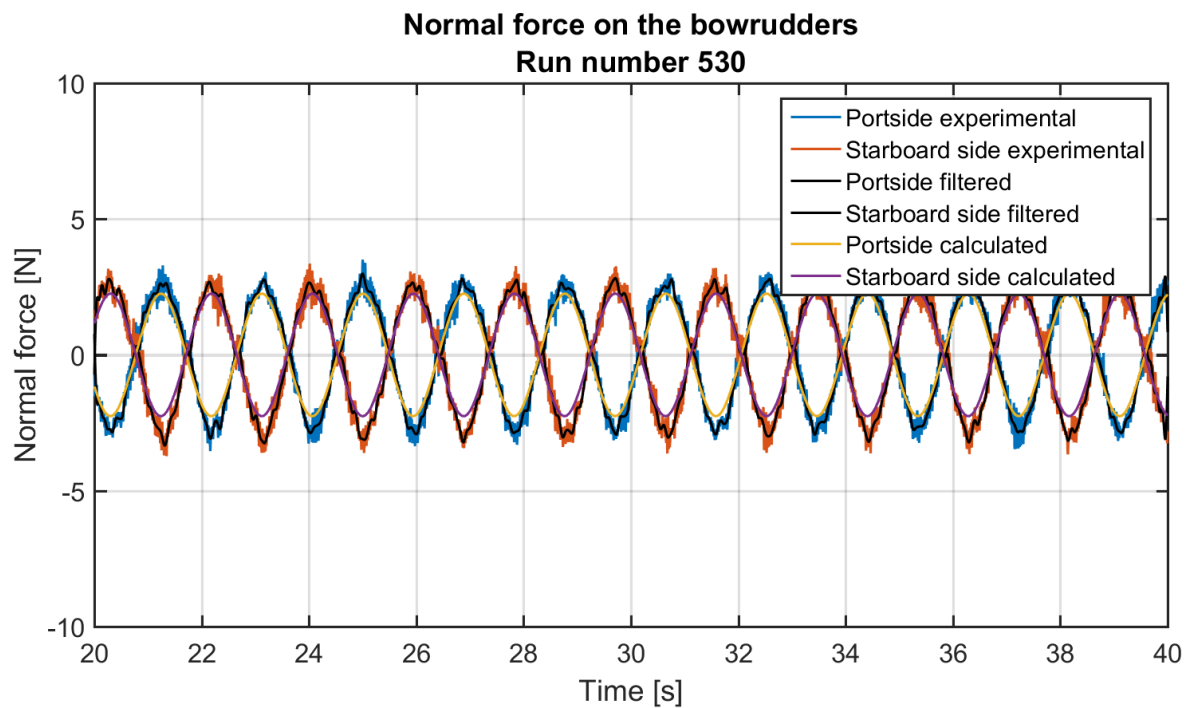


Figure D-19: large X-configuration
 $V = 0.84 \text{ m/s}$, $\varphi_A = 20^\circ$, $\omega = 3.420 \text{ rad/s}$

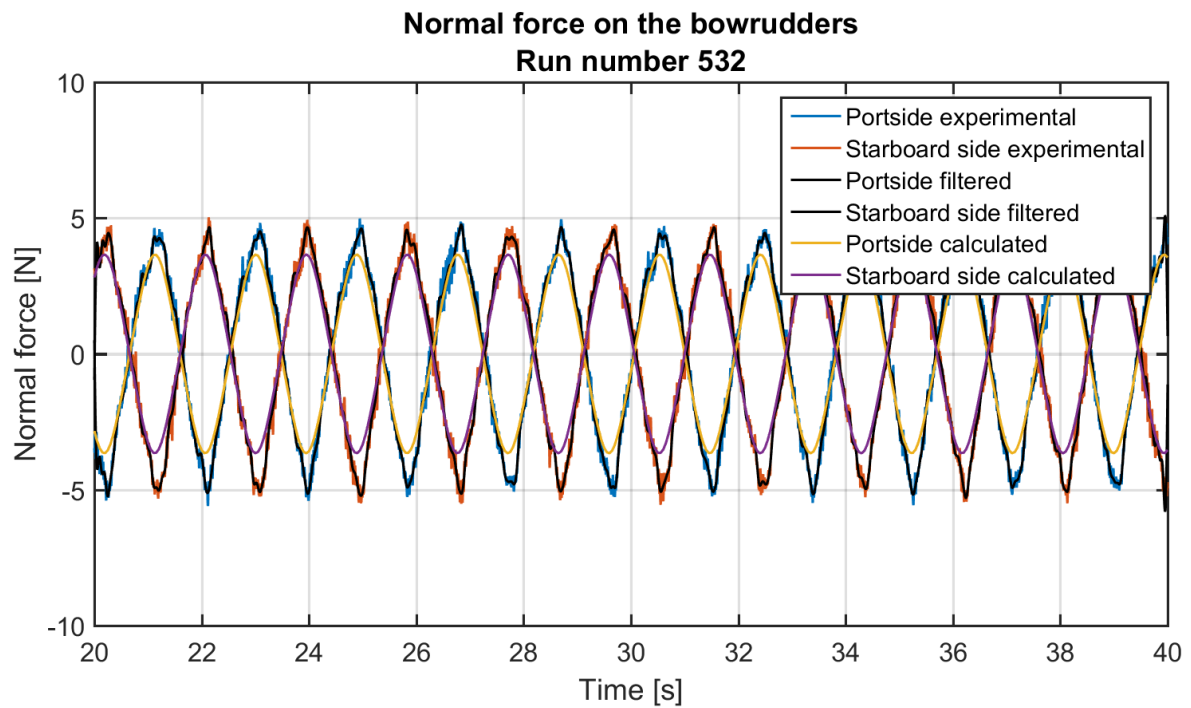


Figure D-20: large X-configuration
 $V = 0.84 \text{ m/s}$, $\varphi_A = 30^\circ$, $\omega = 3.420 \text{ rad/s}$

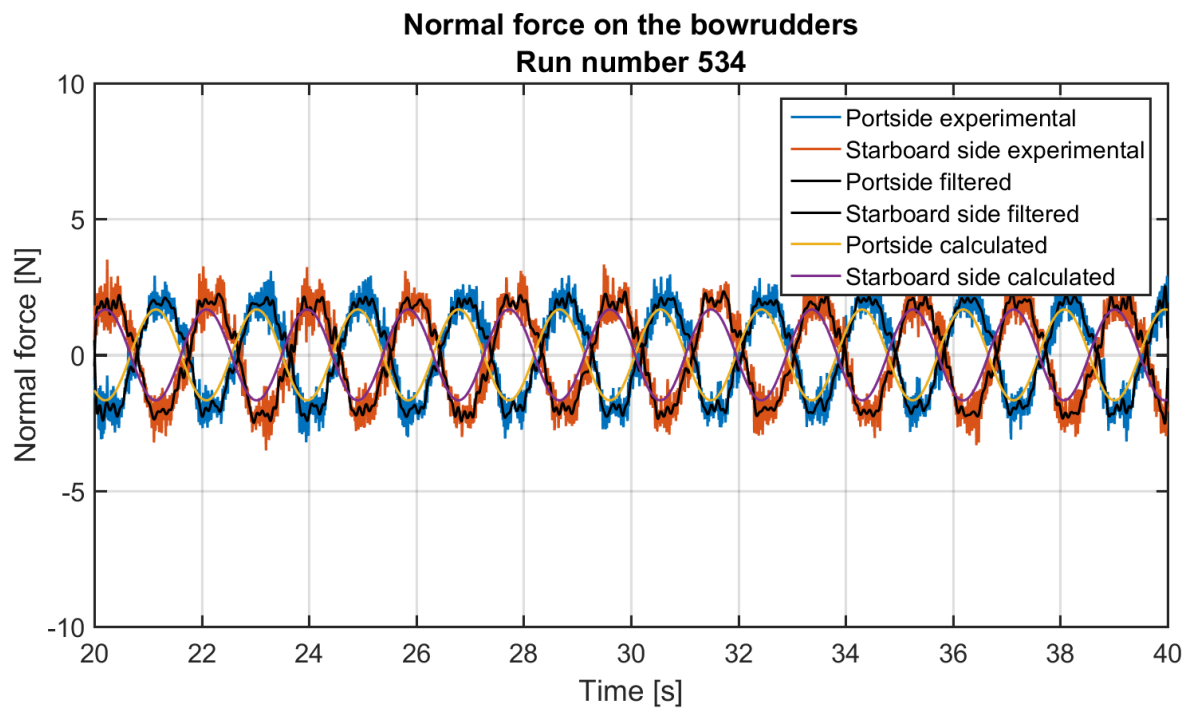


Figure D-21: large X-configuration
 $V = 1.26 \text{ m/s}$, $\varphi_A = 10^\circ$, $\omega = 3.420 \text{ rad/s}$

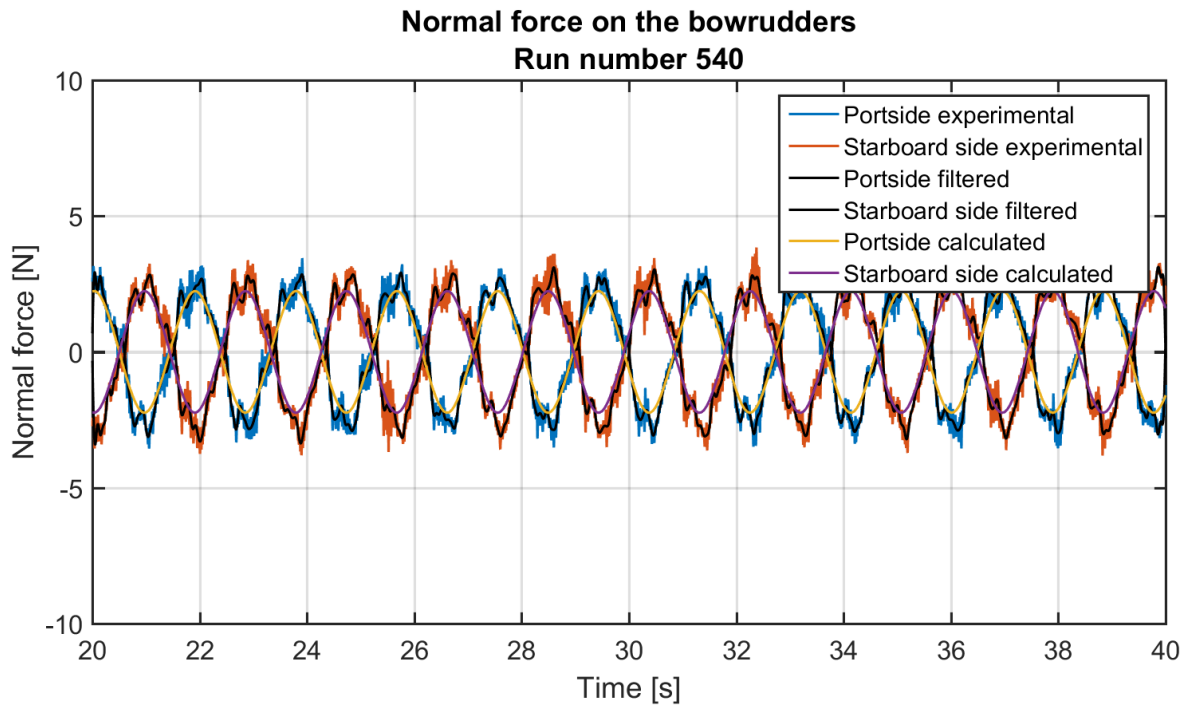


Figure D-22: large X-configuration
 $V = 0.84 \text{ m/s}$, $\varphi_A = 20^\circ$, $\omega = 3.420 \text{ rad/s}$

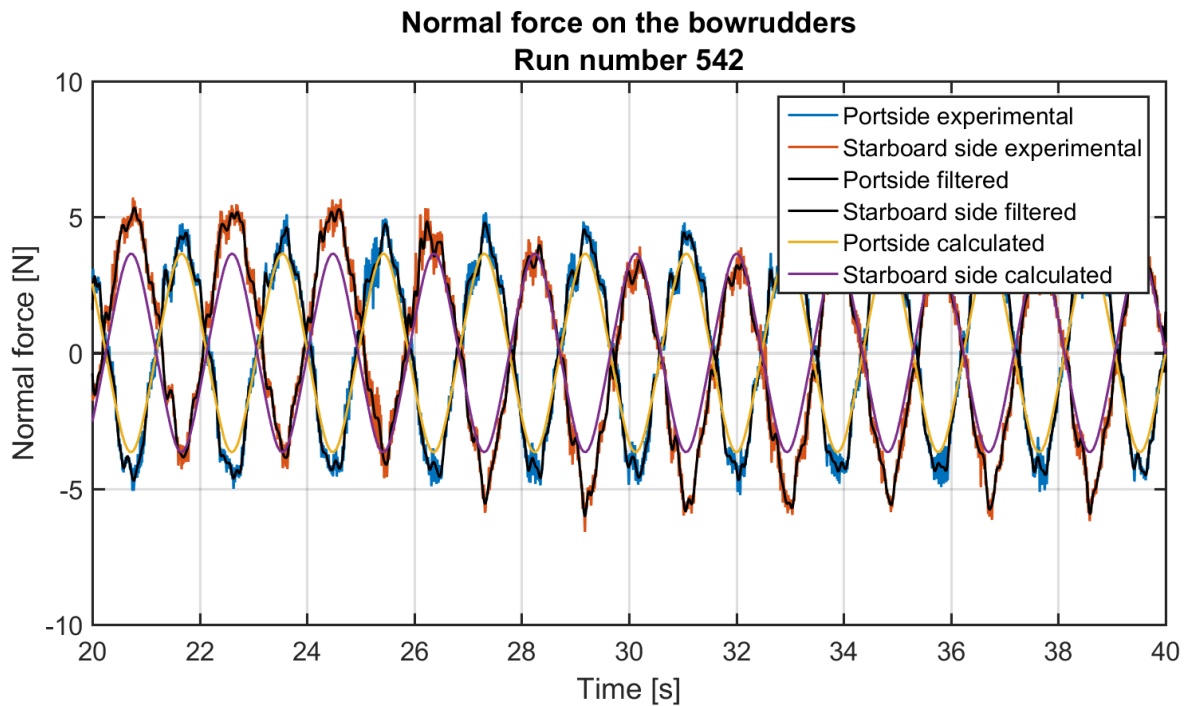


Figure D-23: large X-configuration
 $V = 0.84 \text{ m/s}$, $\varphi_A = 30^\circ$, $\omega = 3.420 \text{ rad/s}$

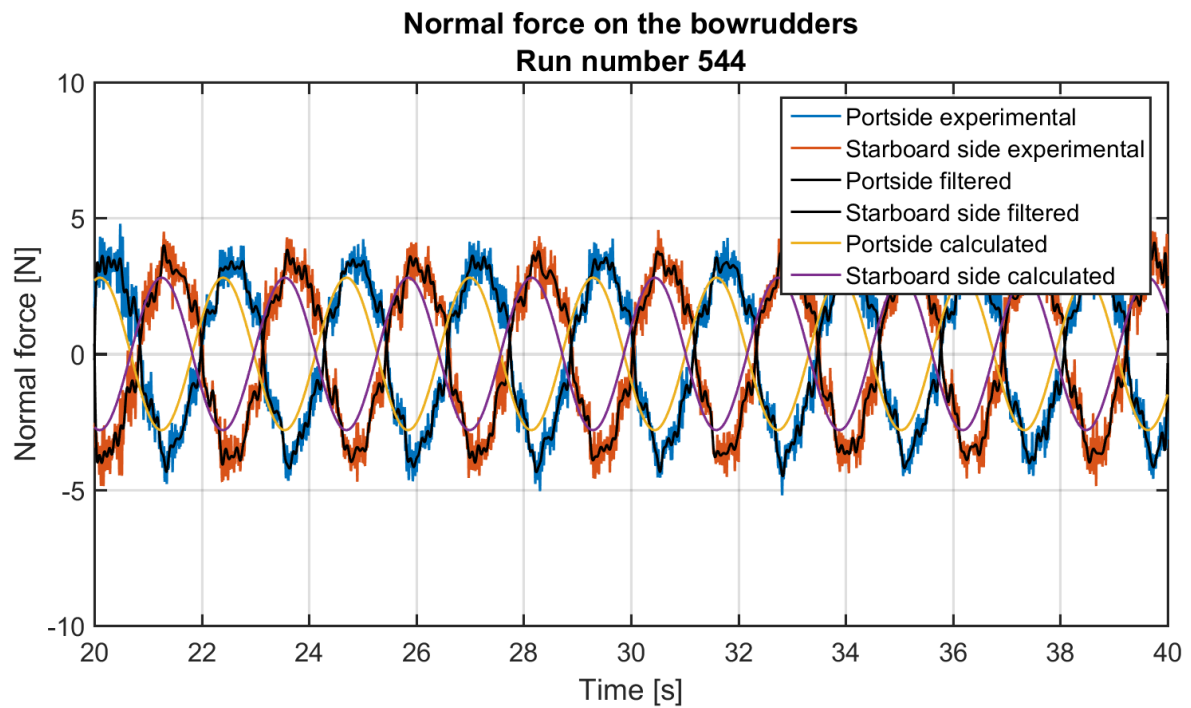


Figure D-24: large X-configuration
 $V = 1.26 \text{ m/s}$, $\varphi_A = 20^\circ$, $\omega = 2.798 \text{ rad/s}$

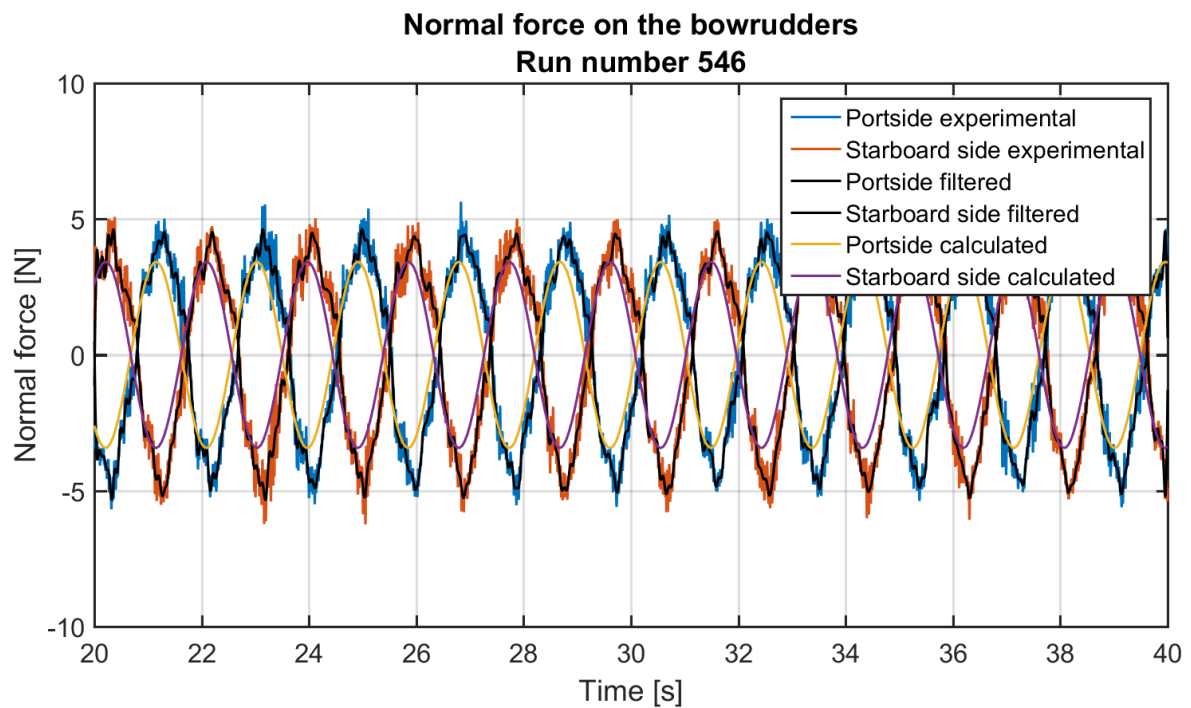


Figure D-25: large X-configuration
 $V = 1.26 \text{ m/s}$, $\varphi_A = 20^\circ$, $\omega = 3.420 \text{ rad/s}$

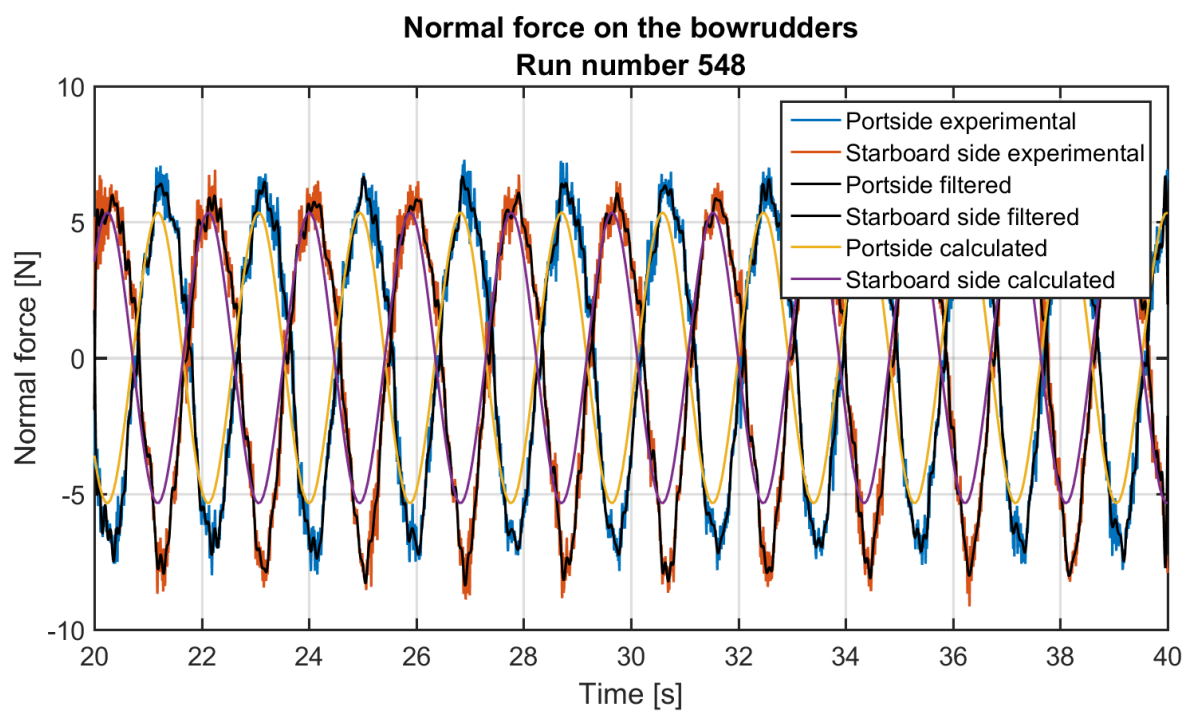


Figure D-26: large X-configuration
 $V = 1.26 \text{ m/s}$, $\varphi_A = 30^\circ$, $\omega = 3.420 \text{ rad/s}$

D-2 Aft rudders

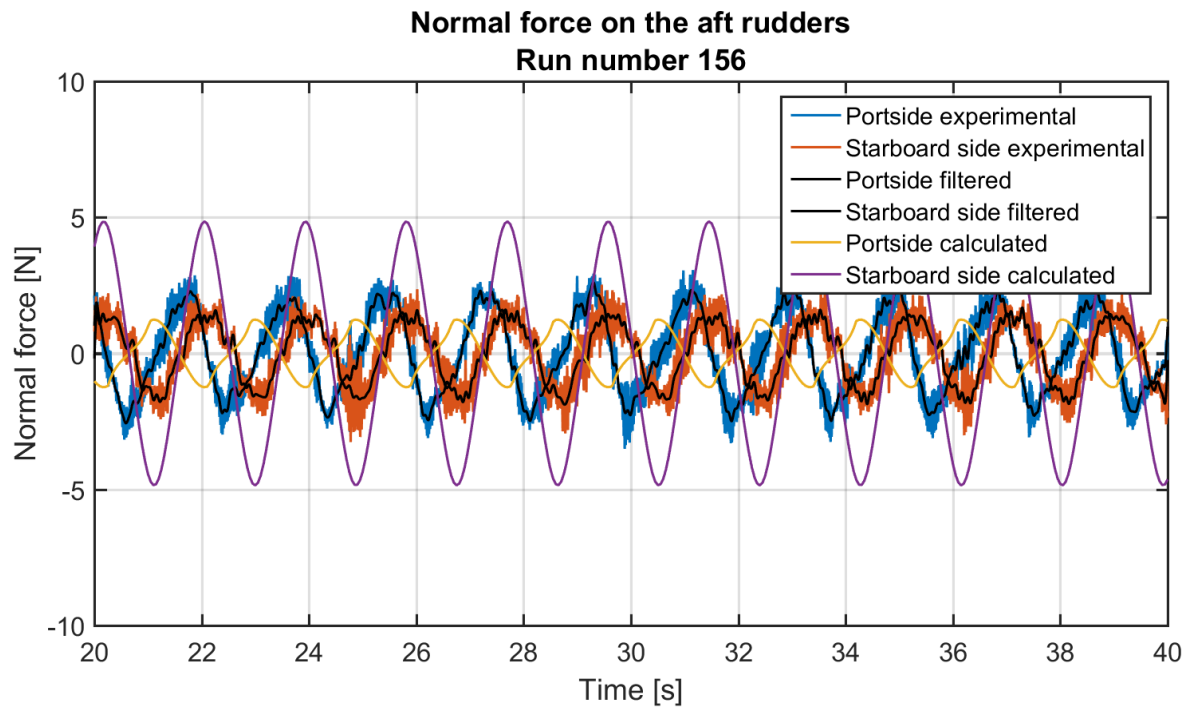


Figure D-27: small X-configuration
 $V = 0.84 \text{ m/s}$, $\varphi_A = 30^\circ$, $\omega = 3.420 \text{ rad/s}$

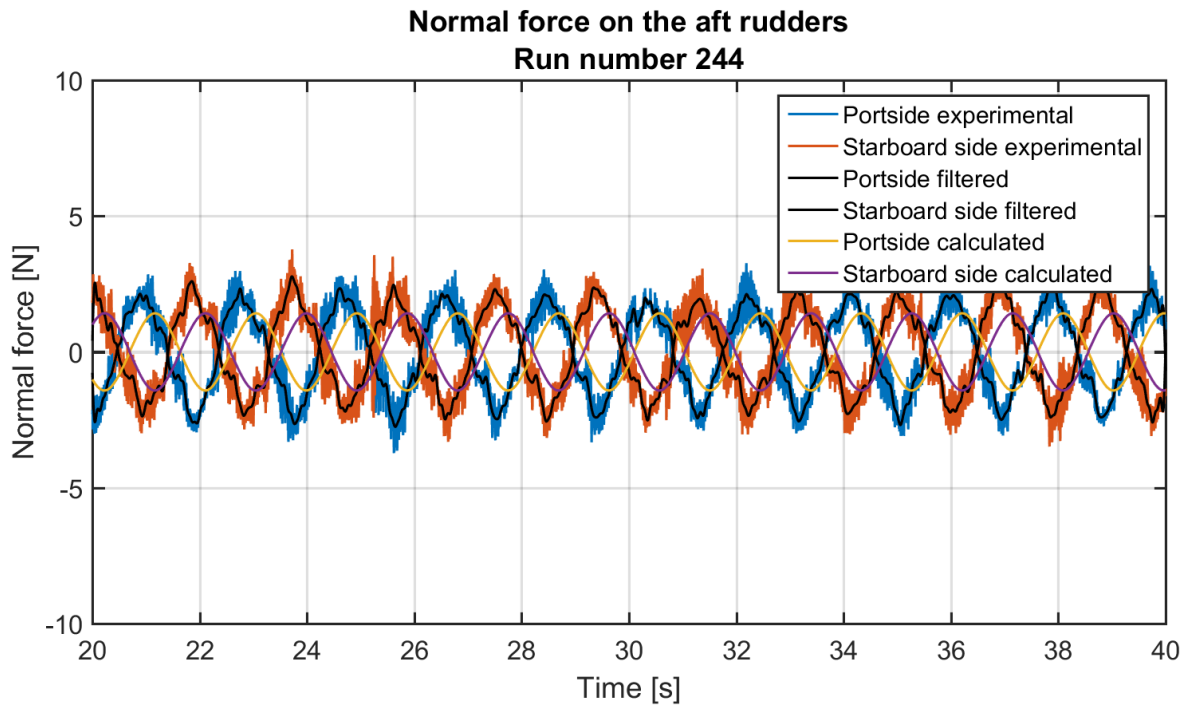


Figure D-28: +-configuration, horizontal rudders
 $V = 0.84 \text{ m/s}$, $\varphi_A = 30^\circ$, $\omega = 3.420 \text{ rad/s}$

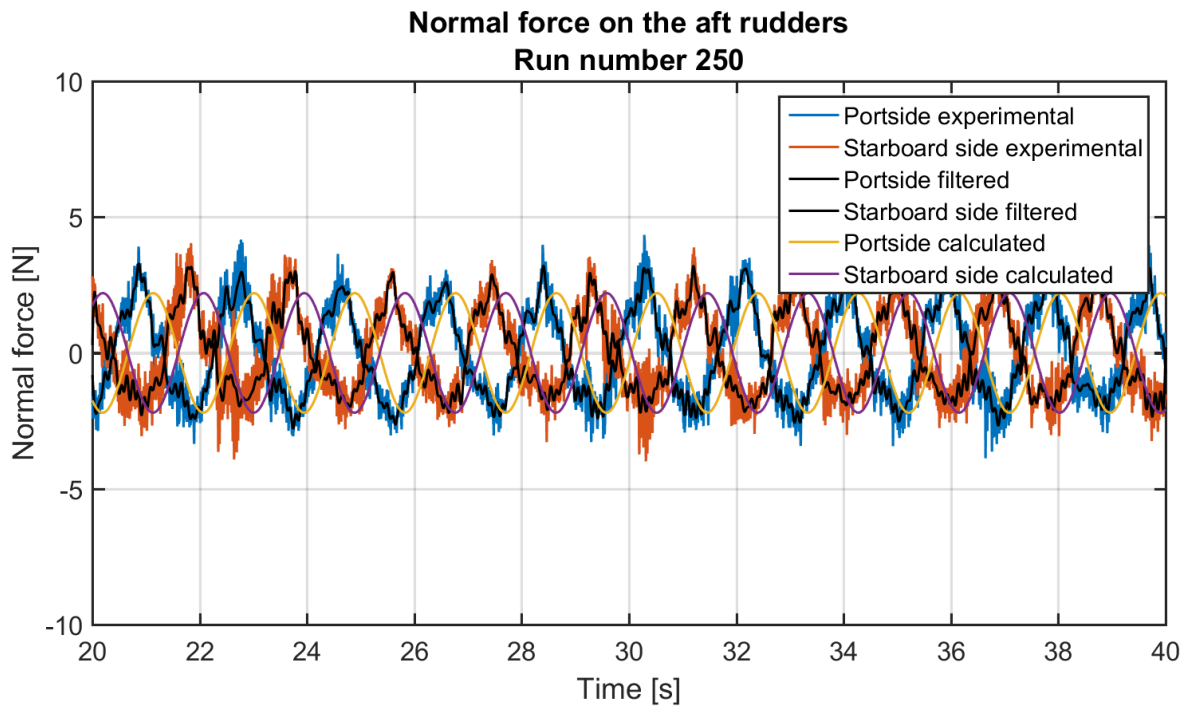


Figure D-29: +-configuration, horizontal rudders
 $V = 1.26 \text{ m/s}$, $\varphi_A = 30^\circ$, $\omega = 3.420 \text{ rad/s}$

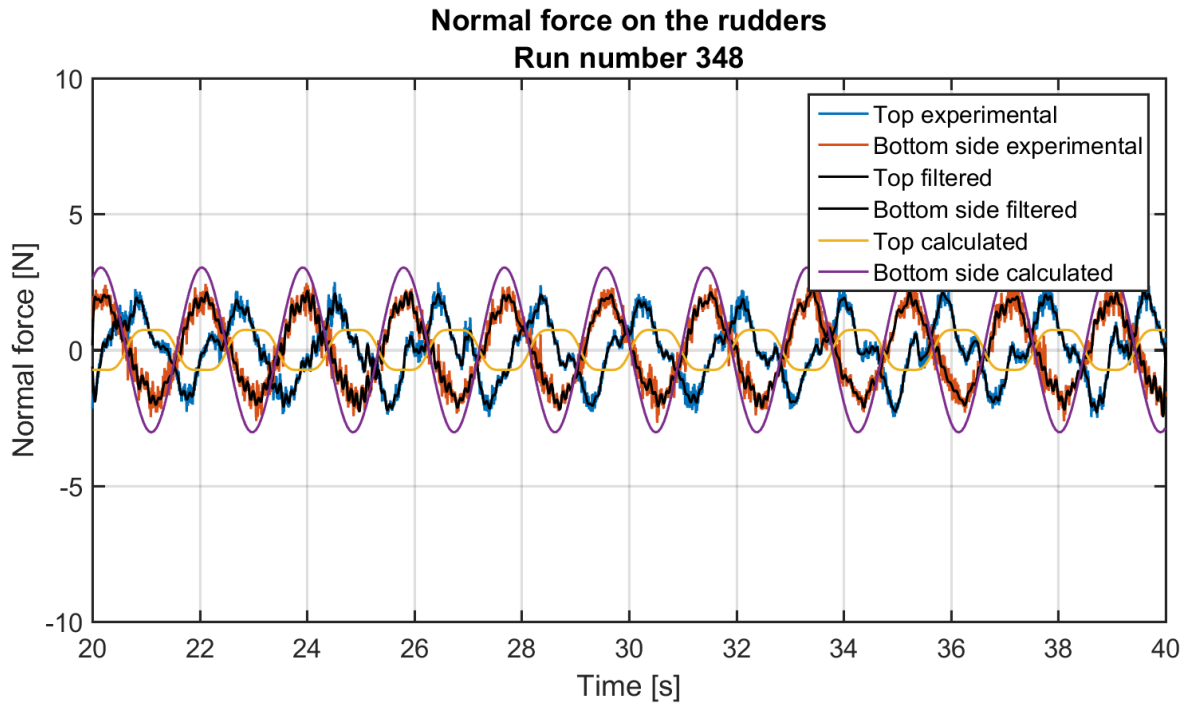


Figure D-30: +-configuration, vertical rudders
 $V = 1.26 \text{ m/s}$, $\varphi_A = 30^\circ$, $\omega = 3.420 \text{ rad/s}$

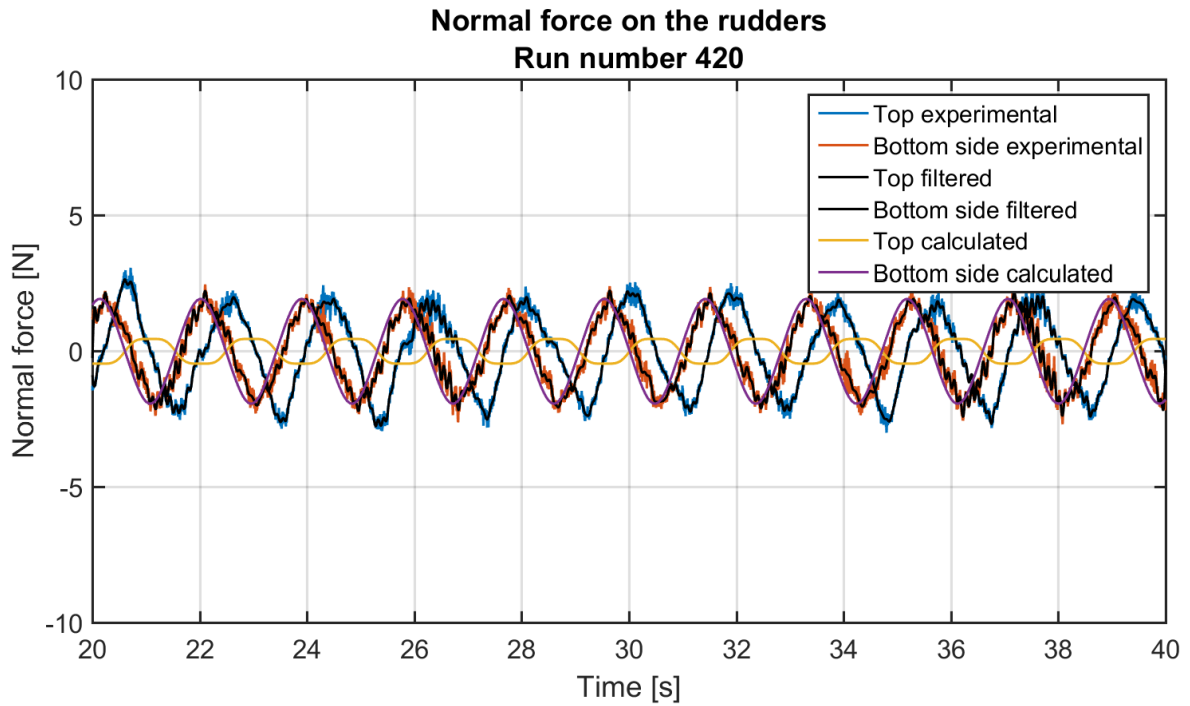


Figure D-31: +-configuration, vertical rudders
 $V = 0.84 \text{ m/s}$, $\varphi_A = 30^\circ$, $\omega = 3.420 \text{ rad/s}$

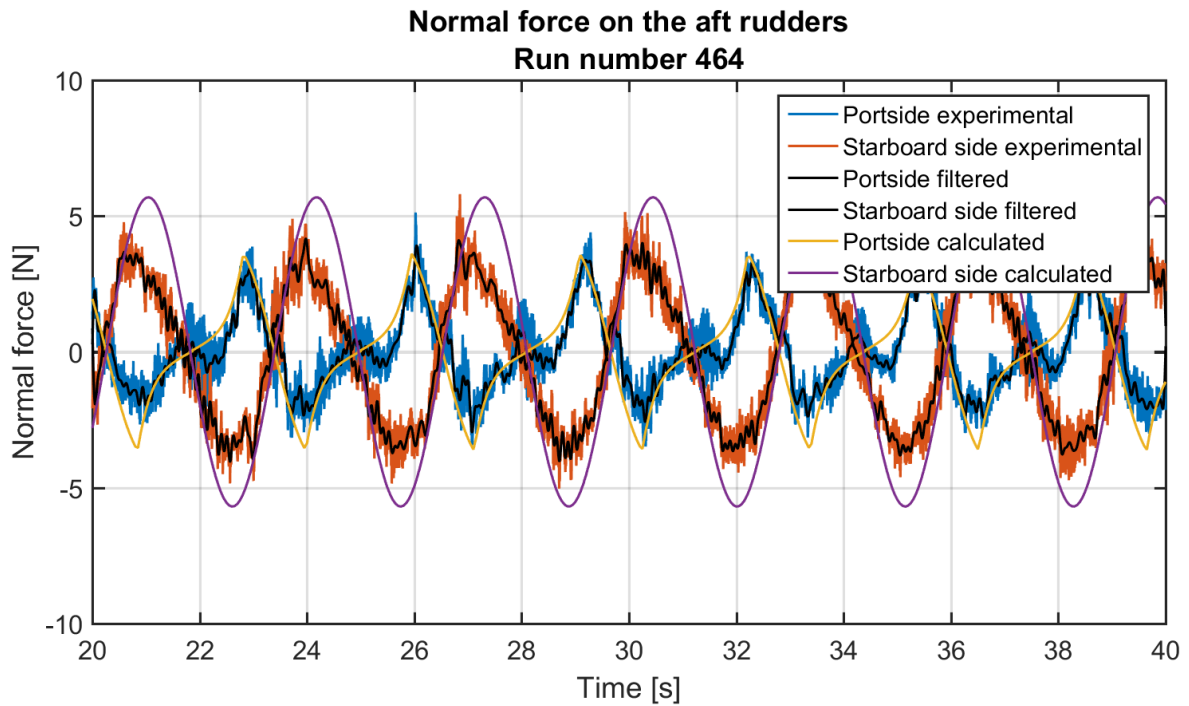


Figure D-32: large X-configuration, with bowplanes
 $V = 1.26 \text{ m/s}$, $\varphi_A = 30^\circ$, $\omega = 2.052 \text{ rad/s}$

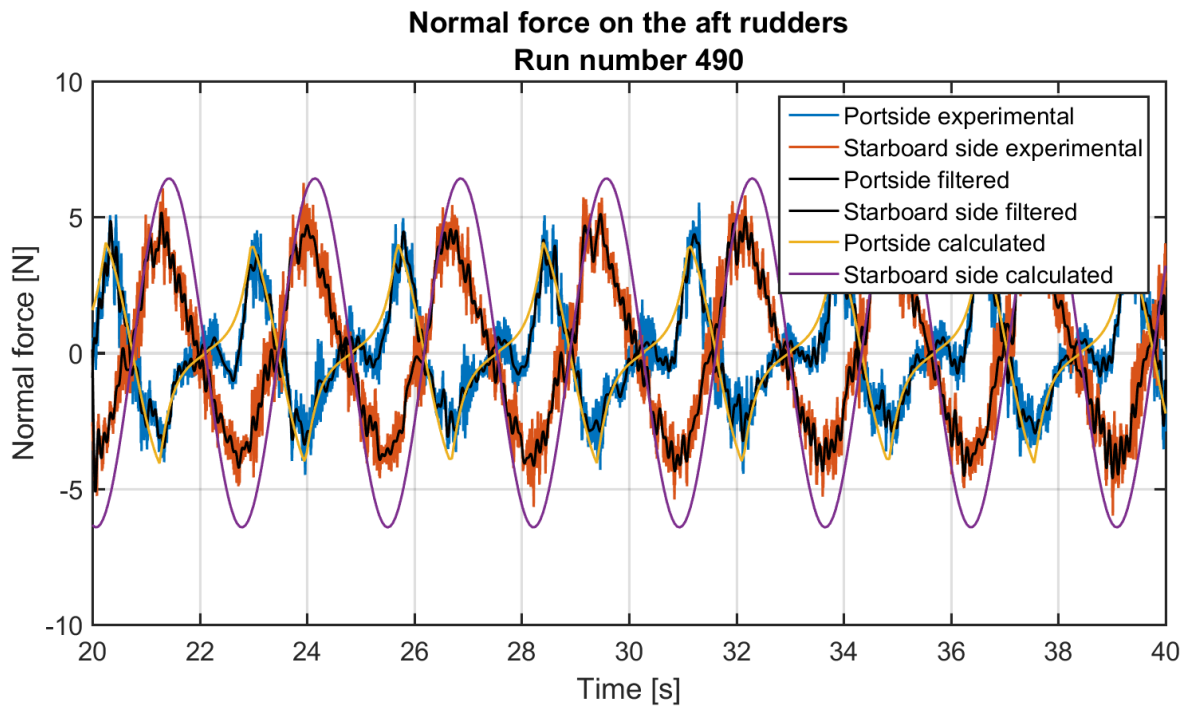


Figure D-33: large X-configuration, with bowplanes
 $V = 1.26 \text{ m/s}$, $\varphi_A = 30^\circ$, $\omega = 2.368 \text{ rad/s}$

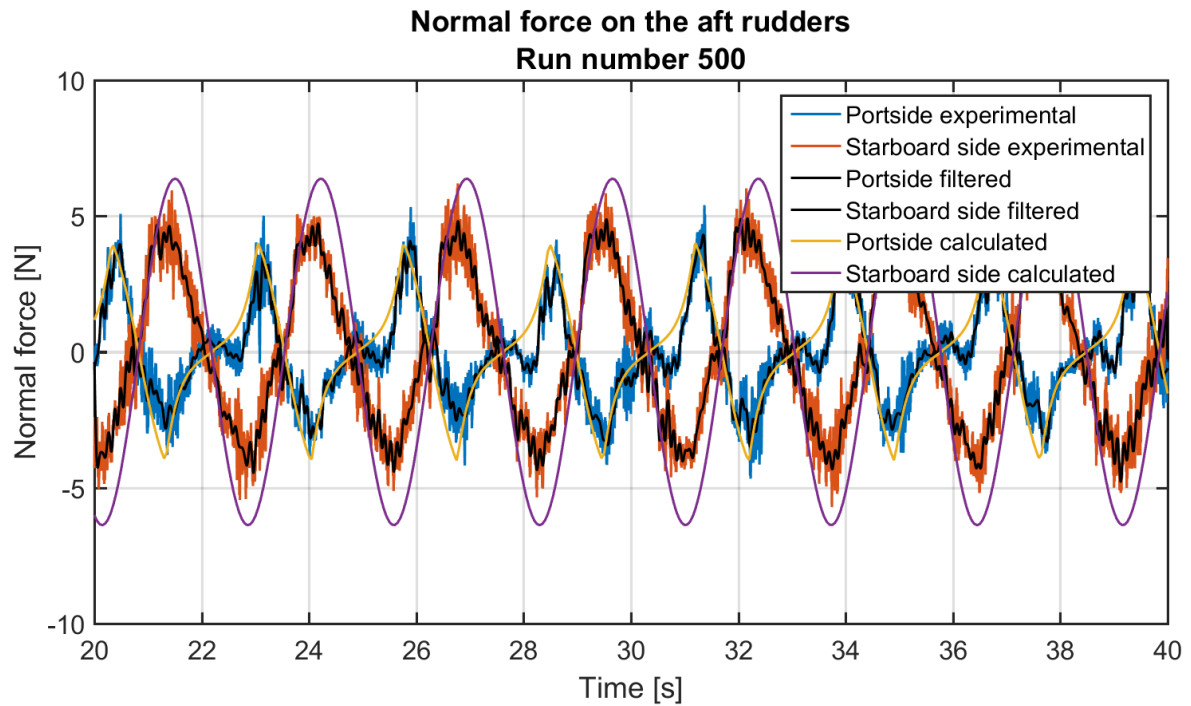


Figure D-34: large X-configuration, with bowplanes
 $V = 1.26 \text{ m/s}$, $\varphi_A = 30^\circ$, $\omega = 2.368 \text{ rad/s}$

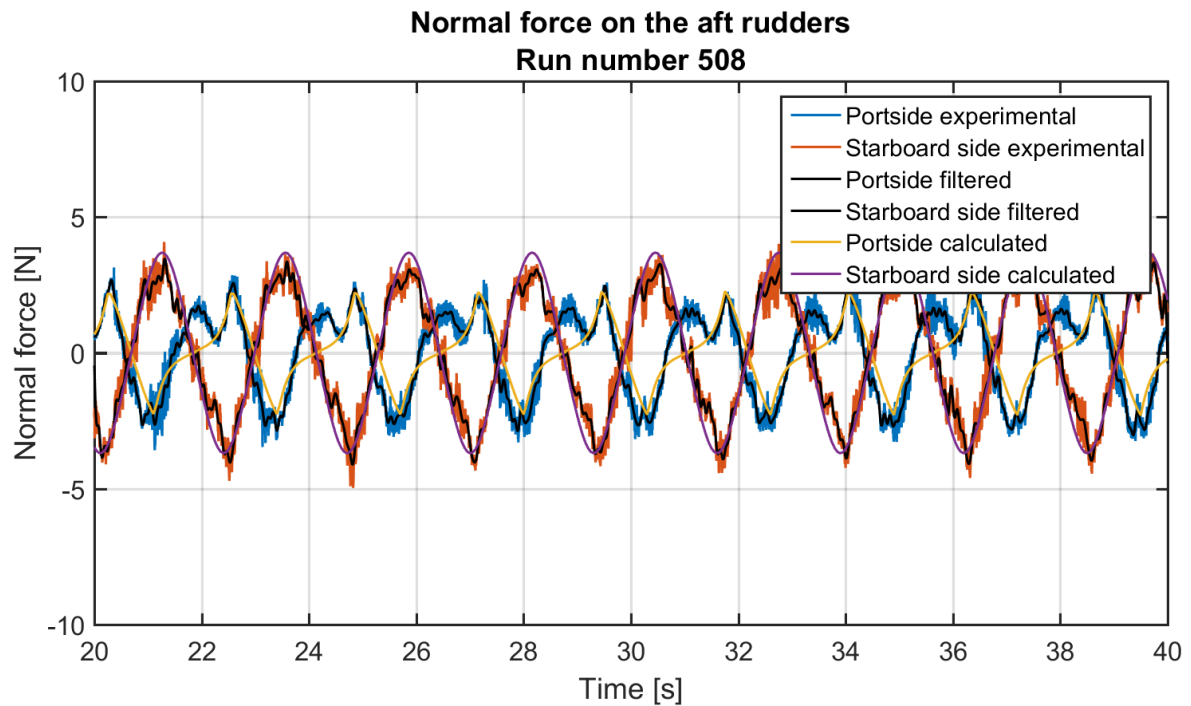


Figure D-35: large X-configuration, with bowplanes
 $V = 0.63 \text{ m/s}$, $\varphi_A = 30^\circ$, $\omega = 2.798 \text{ rad/s}$

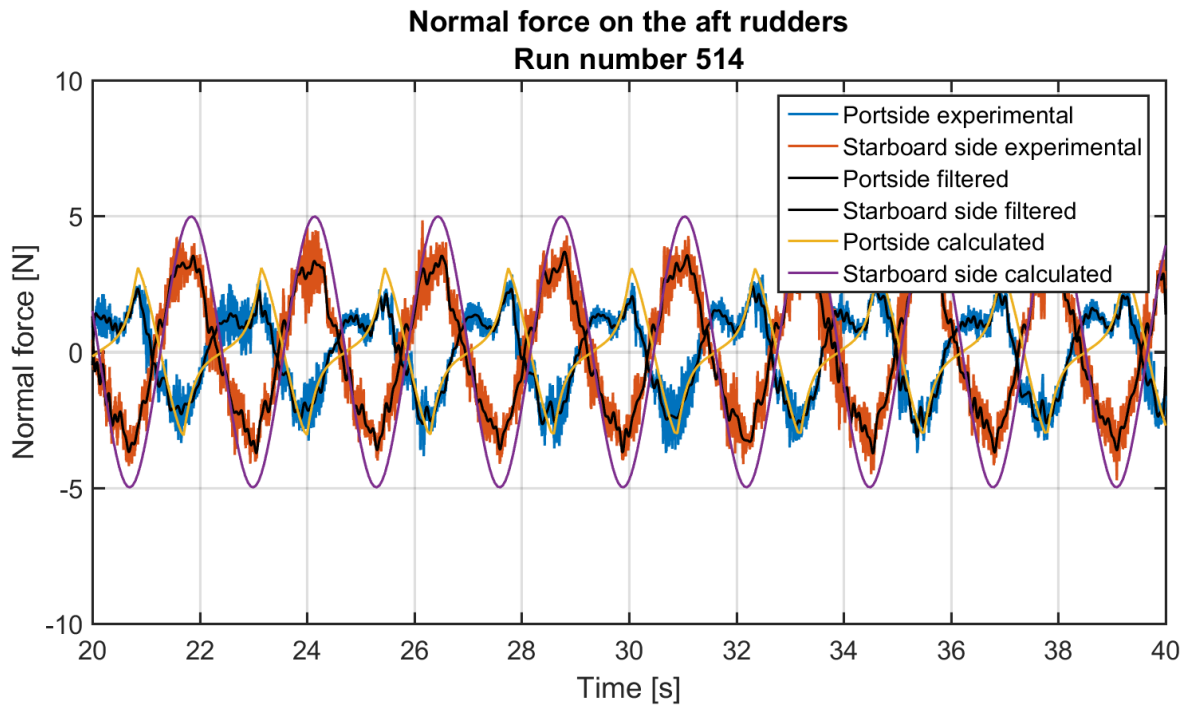


Figure D-36: large X-configuration, with bowplanes
 $V = 0.84 \text{ m/s}$, $\varphi_A = 30^\circ$, $\omega = 2.798 \text{ rad/s}$

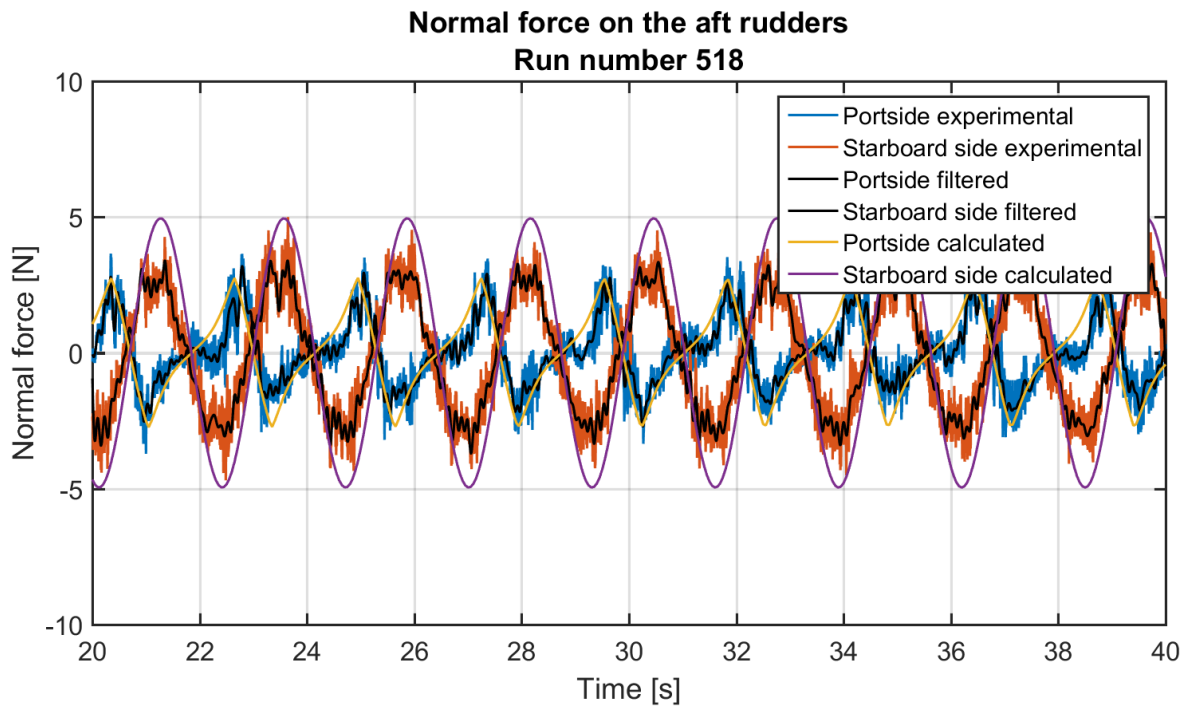


Figure D-37: large X-configuration, with bowplanes
 $V = 1.26 \text{ m/s}$, $\varphi_A = 20^\circ$, $\omega = 2.798 \text{ rad/s}$

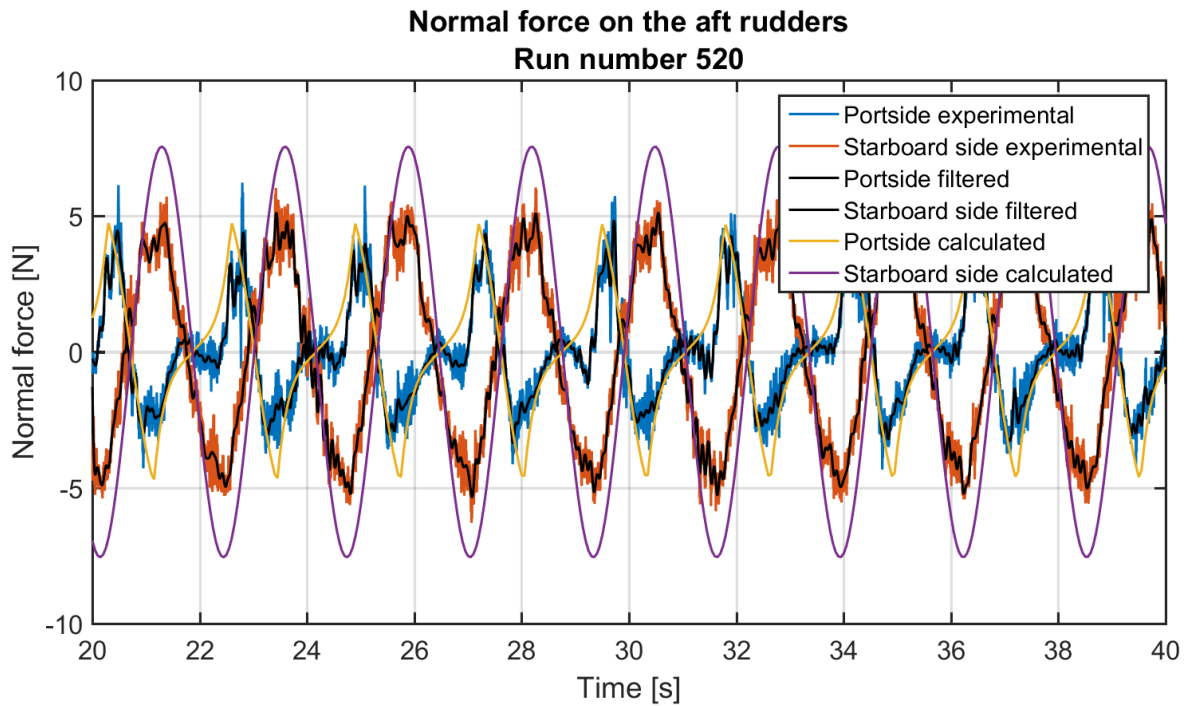


Figure D-38: large X-configuration, with bowplanes
 $V = 1.26 \text{ m/s}$, $\varphi_A = 30^\circ$, $\omega = 2.798 \text{ rad/s}$

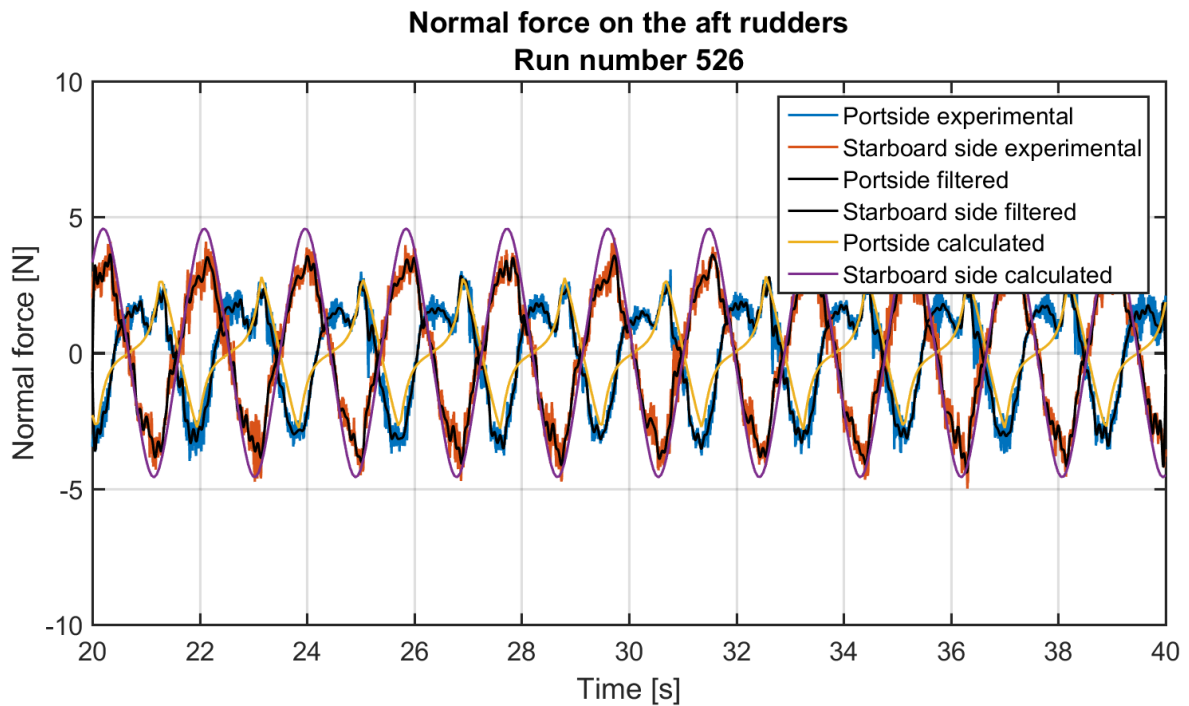


Figure D-39: large X-configuration, with bowplanes
 $V = 0.63 \text{ m/s}$, $\varphi_A = 30^\circ$, $\omega = 3.420 \text{ rad/s}$

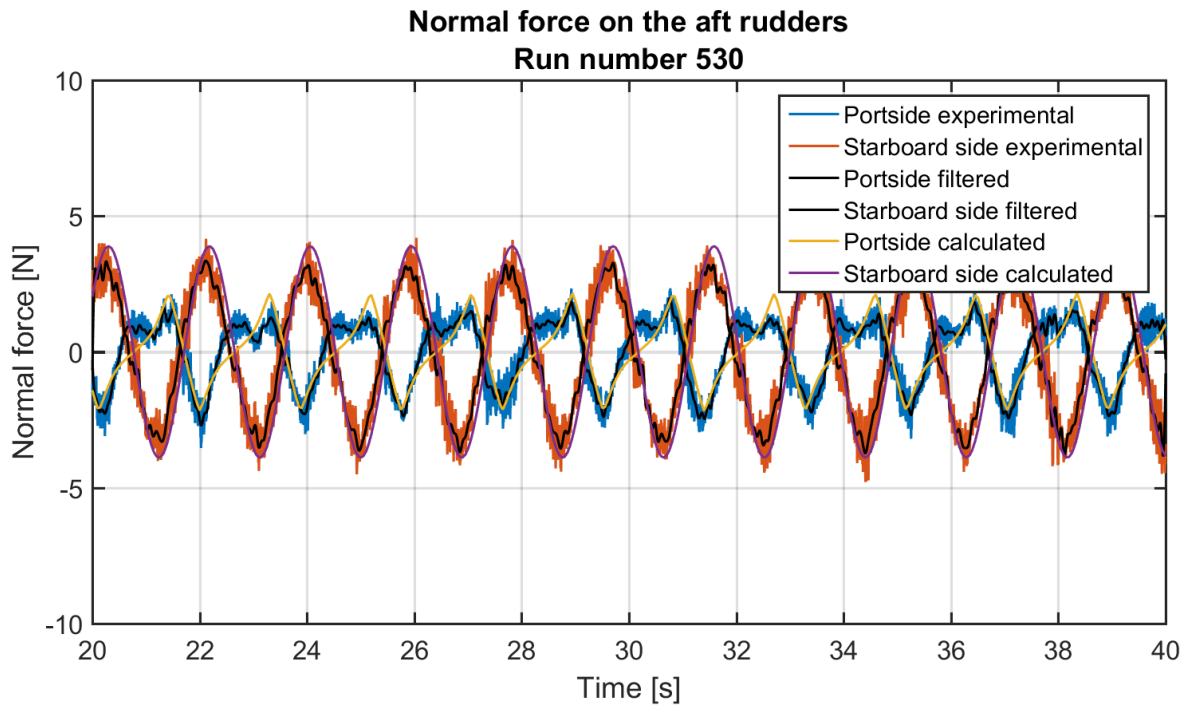


Figure D-40: large X-configuration, with bowplanes
 $V = 0.84 \text{ m/s}$, $\varphi_A = 20^\circ$, $\omega = 3.420 \text{ rad/s}$

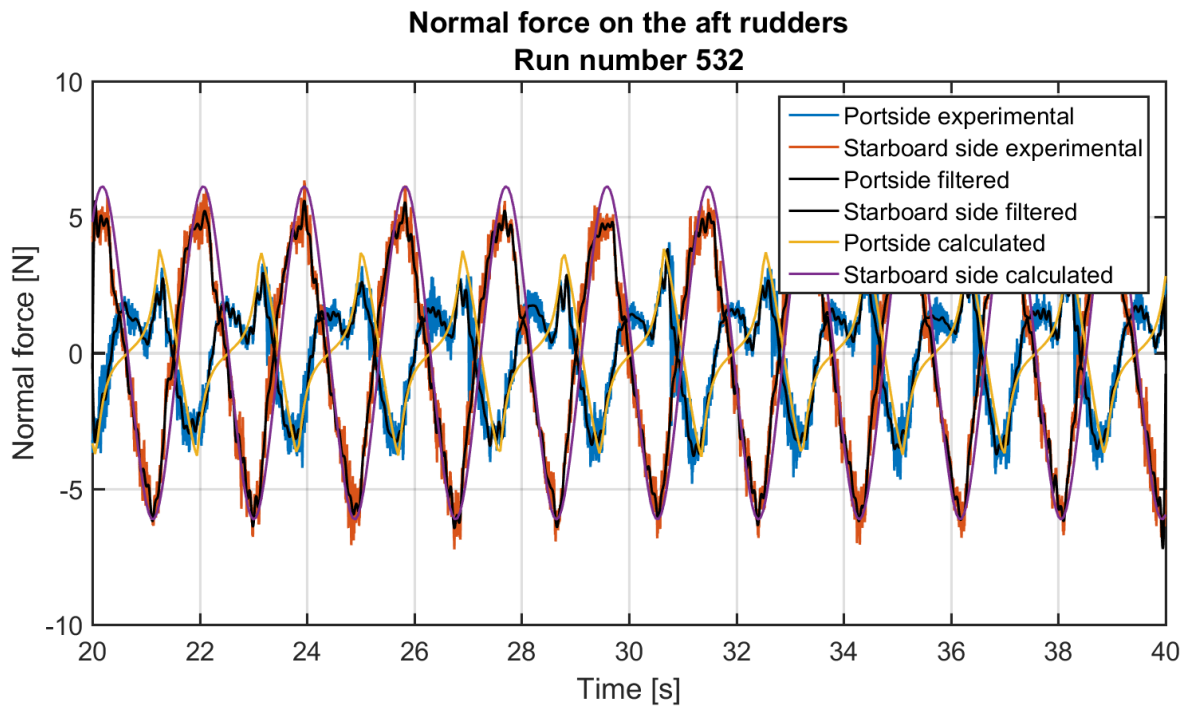


Figure D-41: large X-configuration, with bowplanes
 $V = 0.84 \text{ m/s}$, $\varphi_A = 30^\circ$, $\omega = 3.420 \text{ rad/s}$

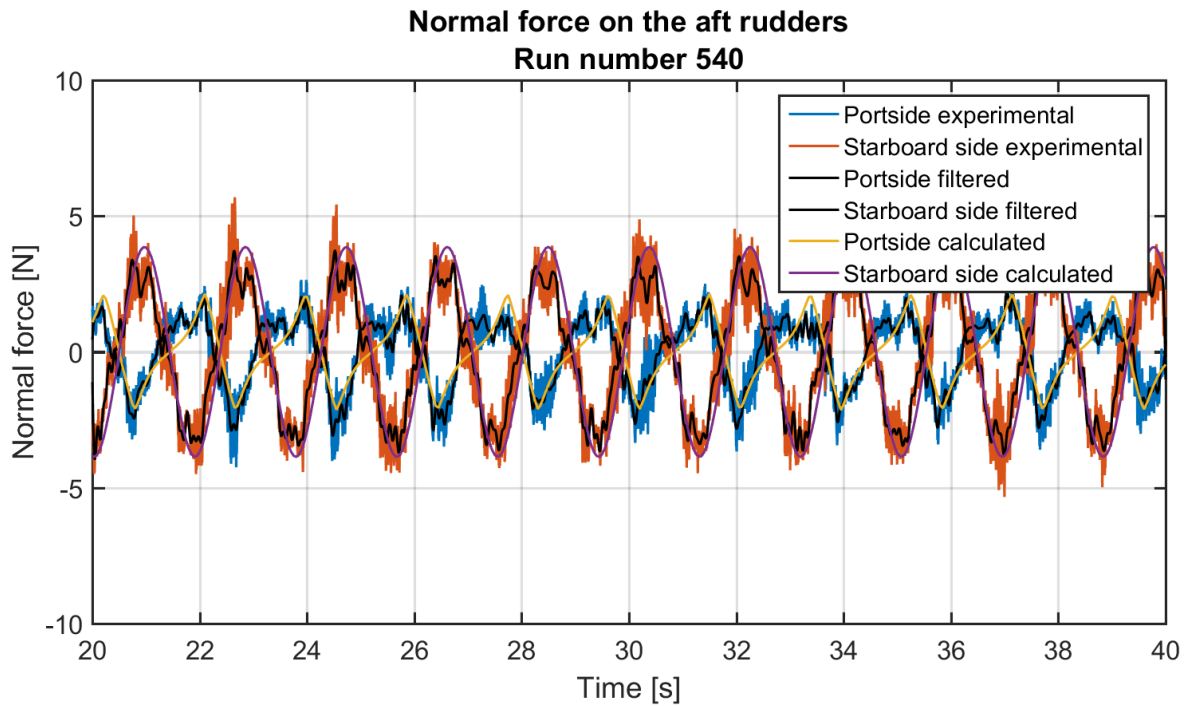


Figure D-42: large X-configuration, with bowplanes
 $V = 0.84 \text{ m/s}$, $\varphi_A = 20^\circ$, $\omega = 3.420 \text{ rad/s}$

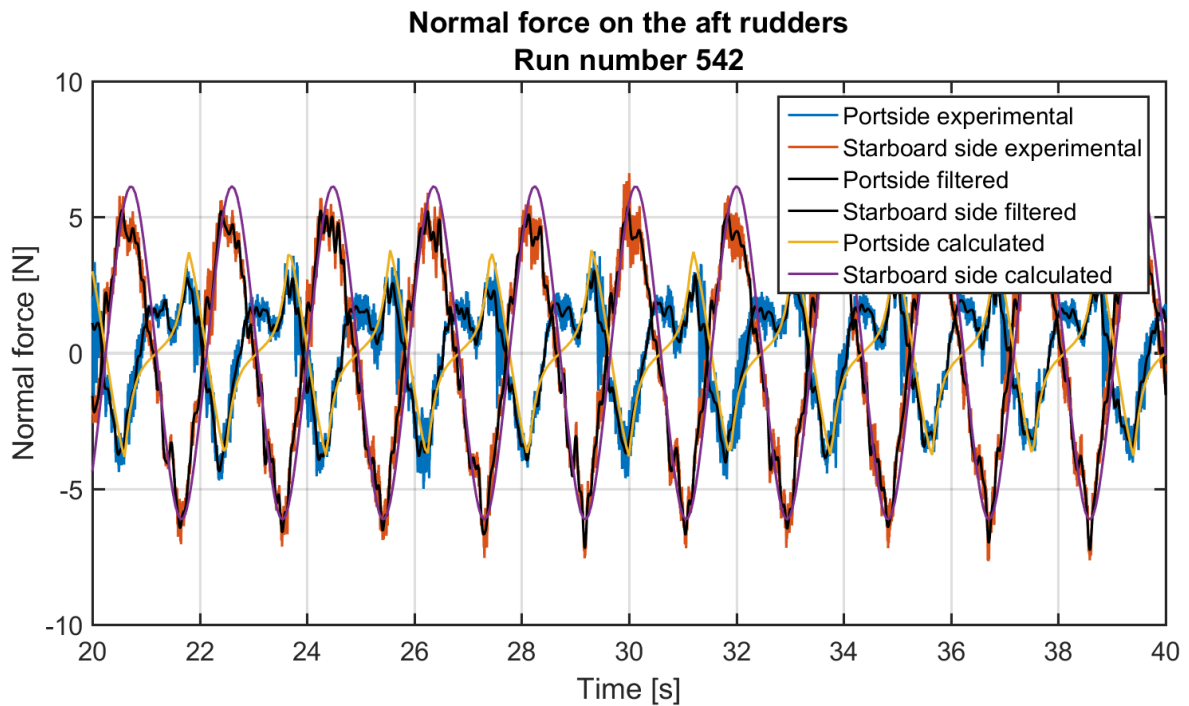


Figure D-43: large X-configuration, with bowplanes
 $V = 0.84 \text{ m/s}$, $\varphi_A = 30^\circ$, $\omega = 3.420 \text{ rad/s}$

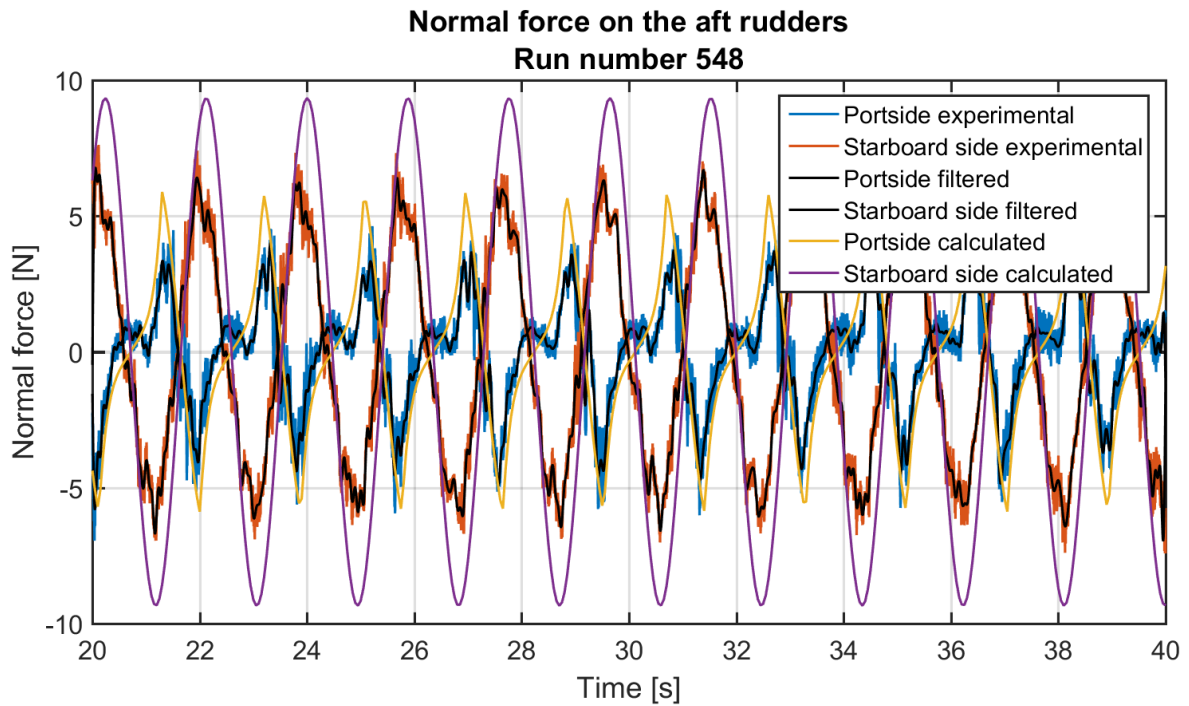


Figure D-44: large X-configuration, with bowplanes
 $V = 1.26 \text{ m/s}$, $\varphi_A = 30^\circ$, $\omega = 3.420 \text{ rad/s}$

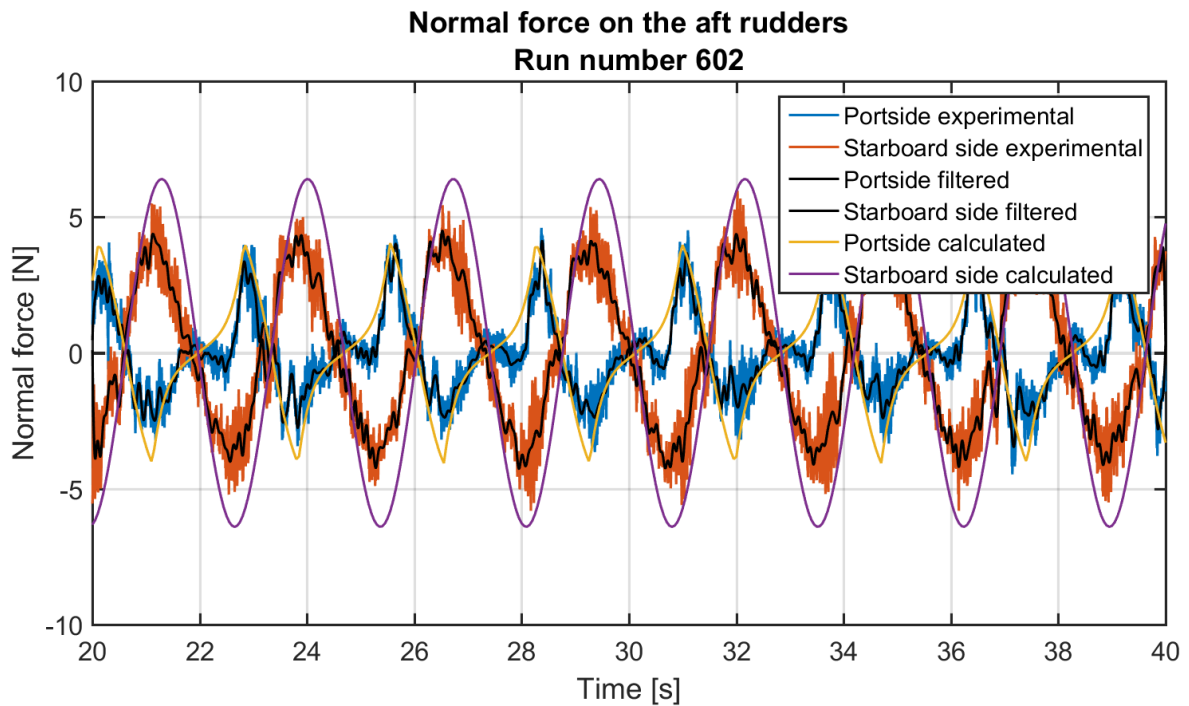


Figure D-45: large X-configuration, without bowplanes
 $V = 1.26 \text{ m/s}$, $\varphi_A = 30^\circ$, $\omega = 2.368 \text{ rad/s}$

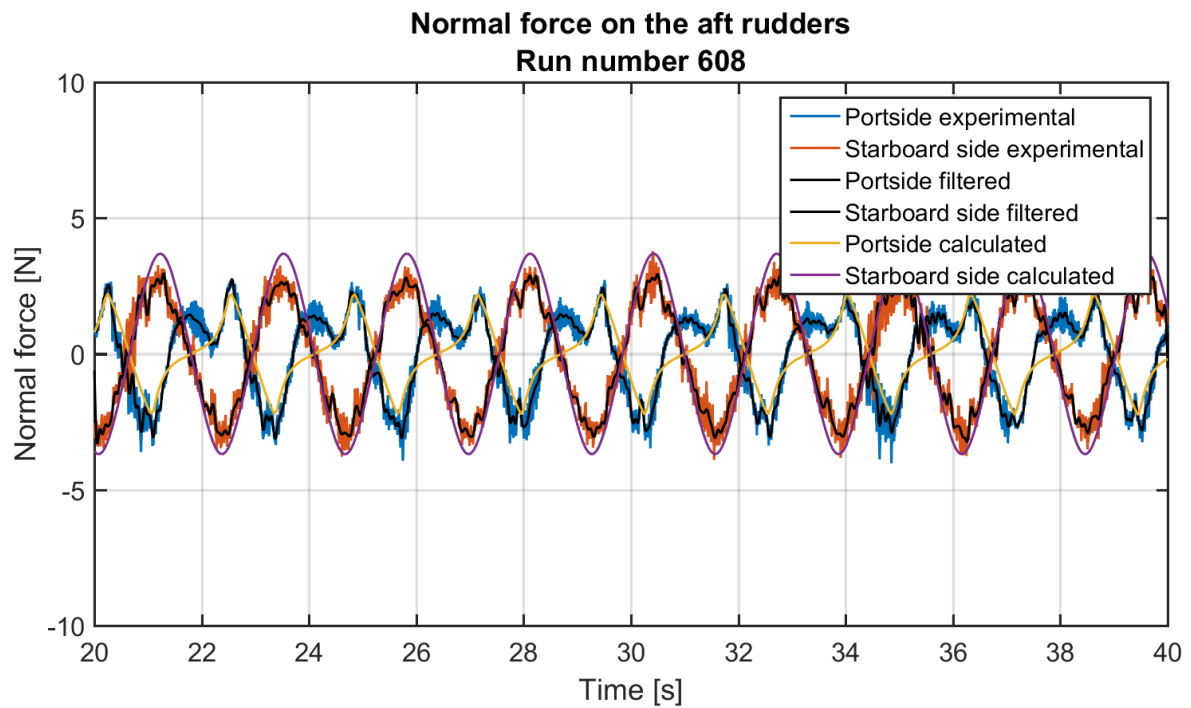


Figure D-46: large X-configuration, without bowplanes

$$V = 0.63 \text{ m/s}, \varphi_A = 30^\circ, \omega = 2.798 \text{ rad/s}$$

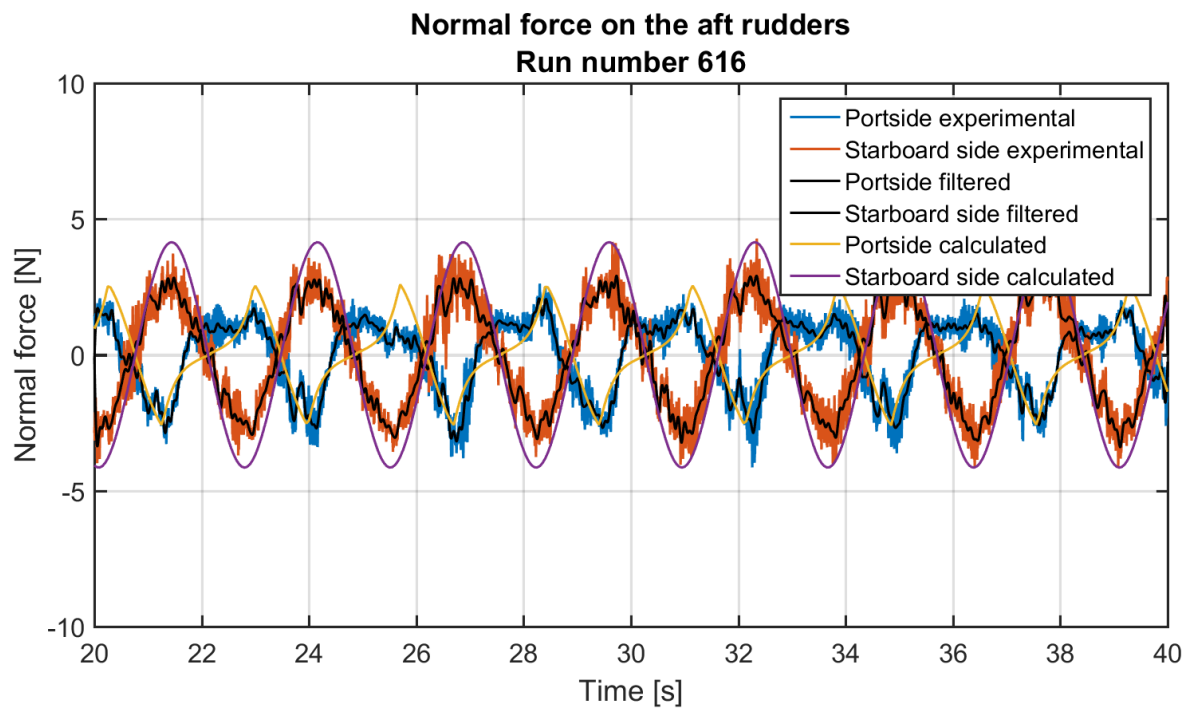


Figure D-47: large X-configuration, without bowplanes

$$V = 0.84 \text{ m/s}, \varphi_A = 30^\circ, \omega = 2.368 \text{ rad/s}$$

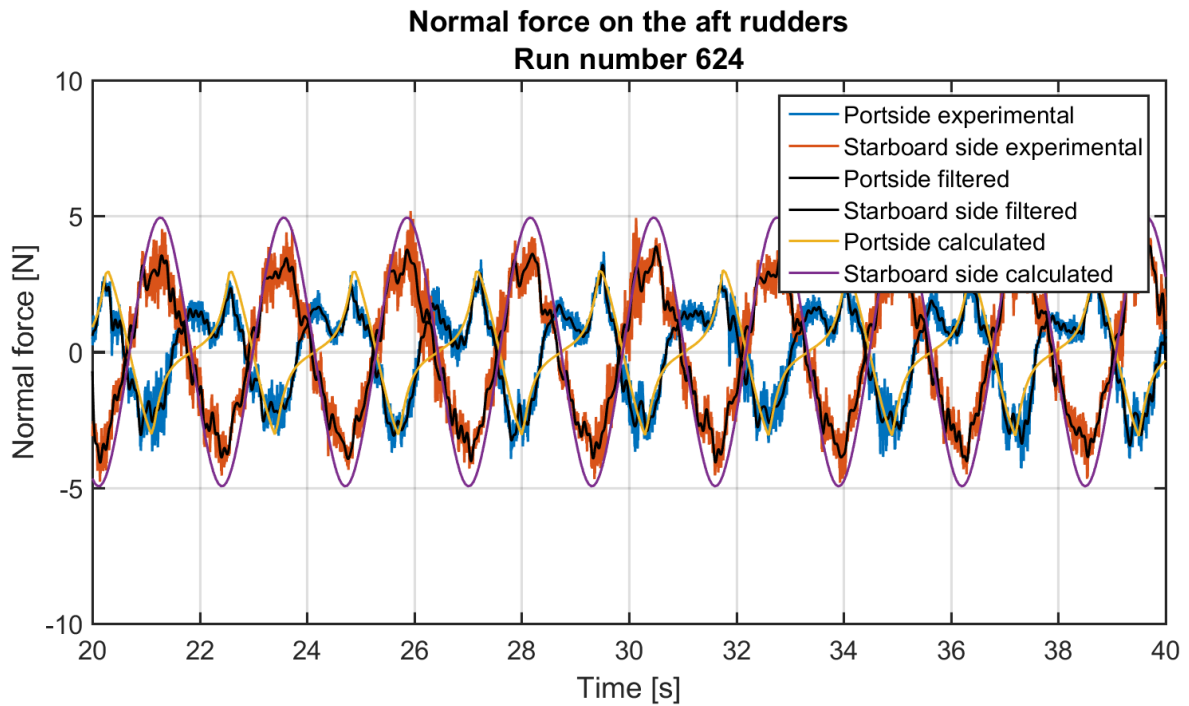


Figure D-48: large X-configuration, without bowplanes
 $V = 0.84 \text{ m/s}$, $\varphi_A = 30^\circ$, $\omega = 2.798 \text{ rad/s}$

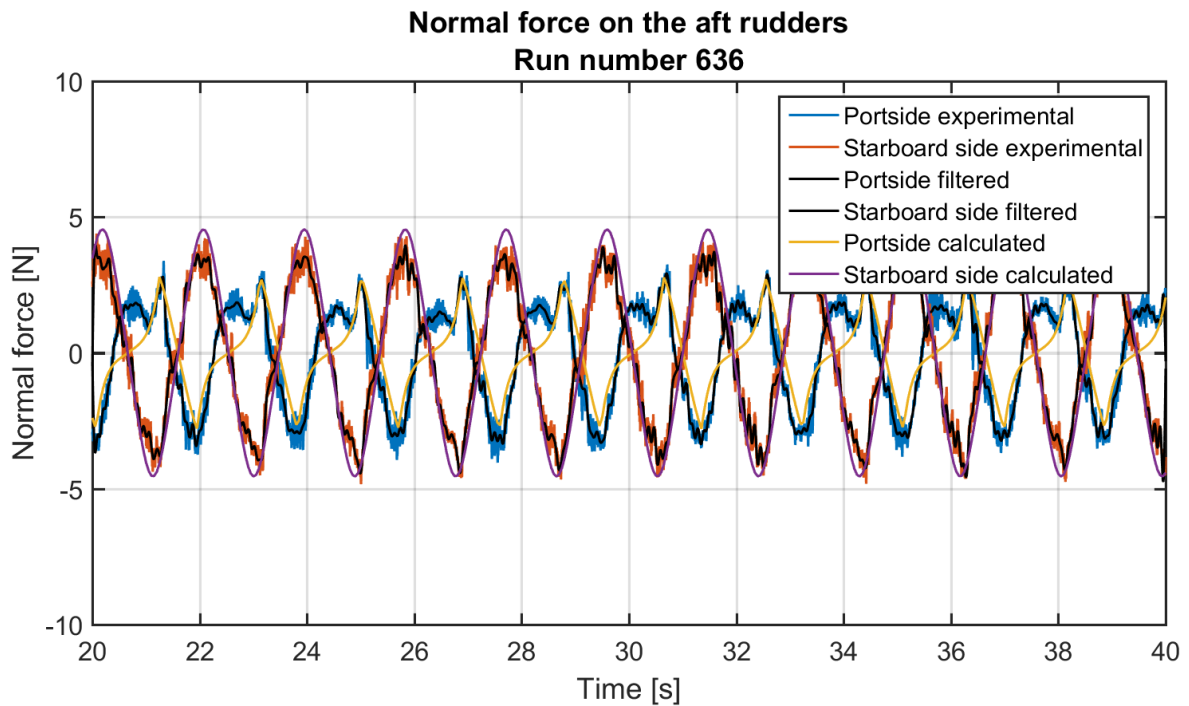


Figure D-49: large X-configuration, without bowplanes
 $V = 0.63 \text{ m/s}$, $\varphi_A = 30^\circ$, $\omega = 3.420 \text{ rad/s}$

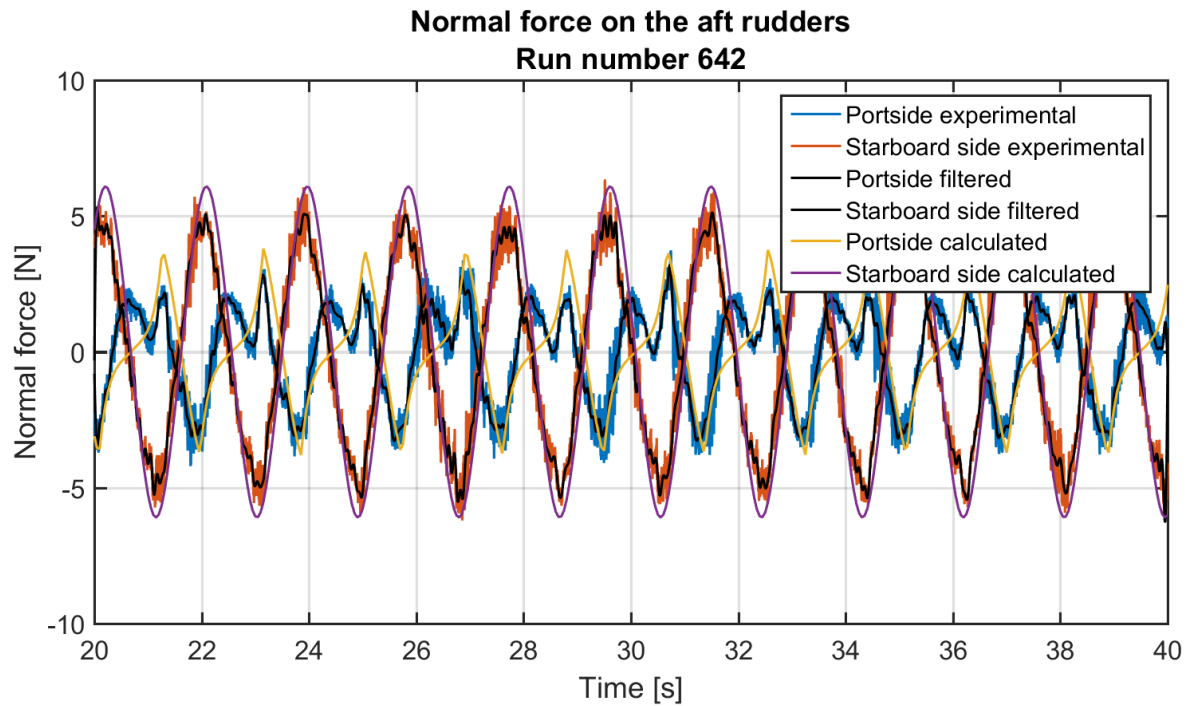


Figure D-50: large X-configuration, without bowplanes
 $V = 0.84 \text{ m/s}$, $\varphi_A = 30^\circ$, $\omega = 3.420 \text{ rad/s}$

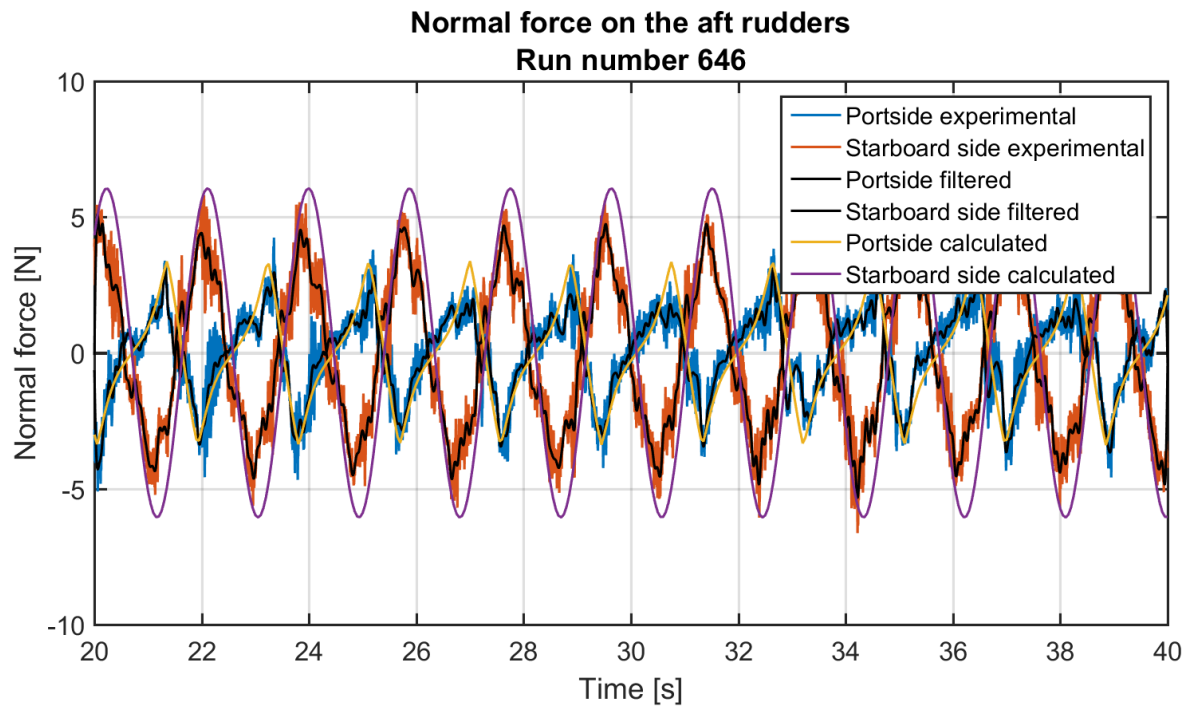


Figure D-51: large X-configuration, without bowplanes
 $V = 1.26 \text{ m/s}$, $\varphi_A = 20^\circ$, $\omega = 3.420 \text{ rad/s}$

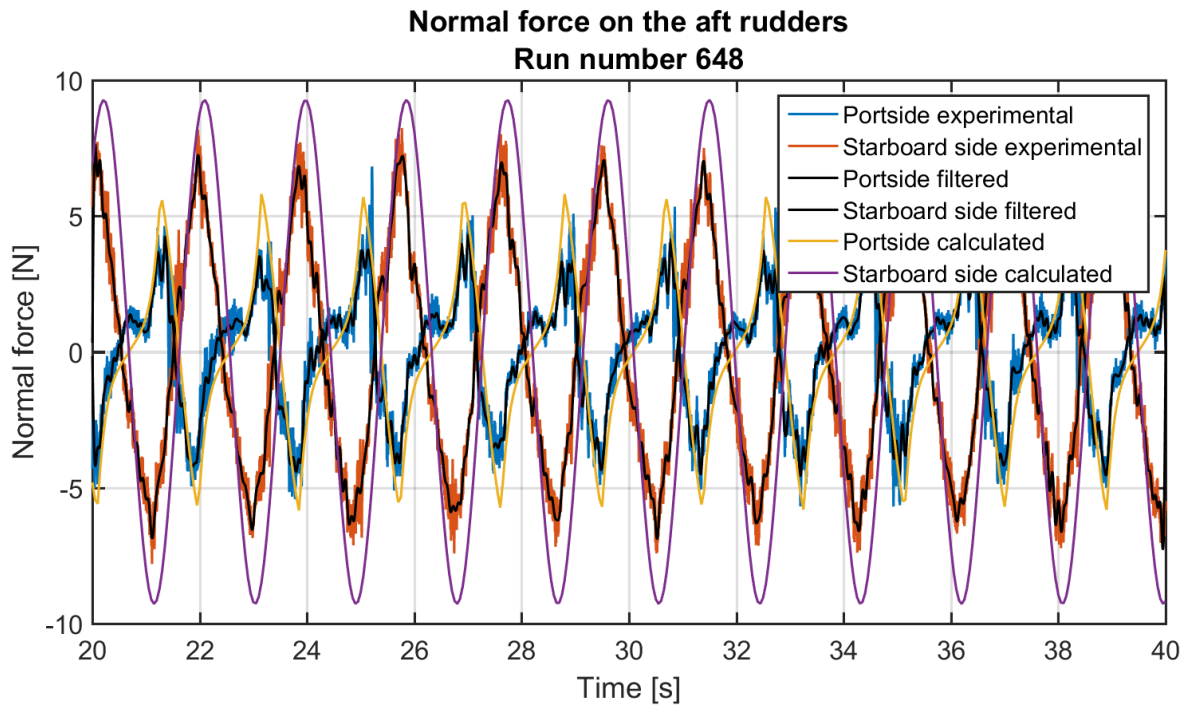


Figure D-52: large X-configuration, without bowplanes
 $V = 1.26 \text{ m/s}$, $\varphi_A = 30^\circ$, $\omega = 3.420 \text{ rad/s}$

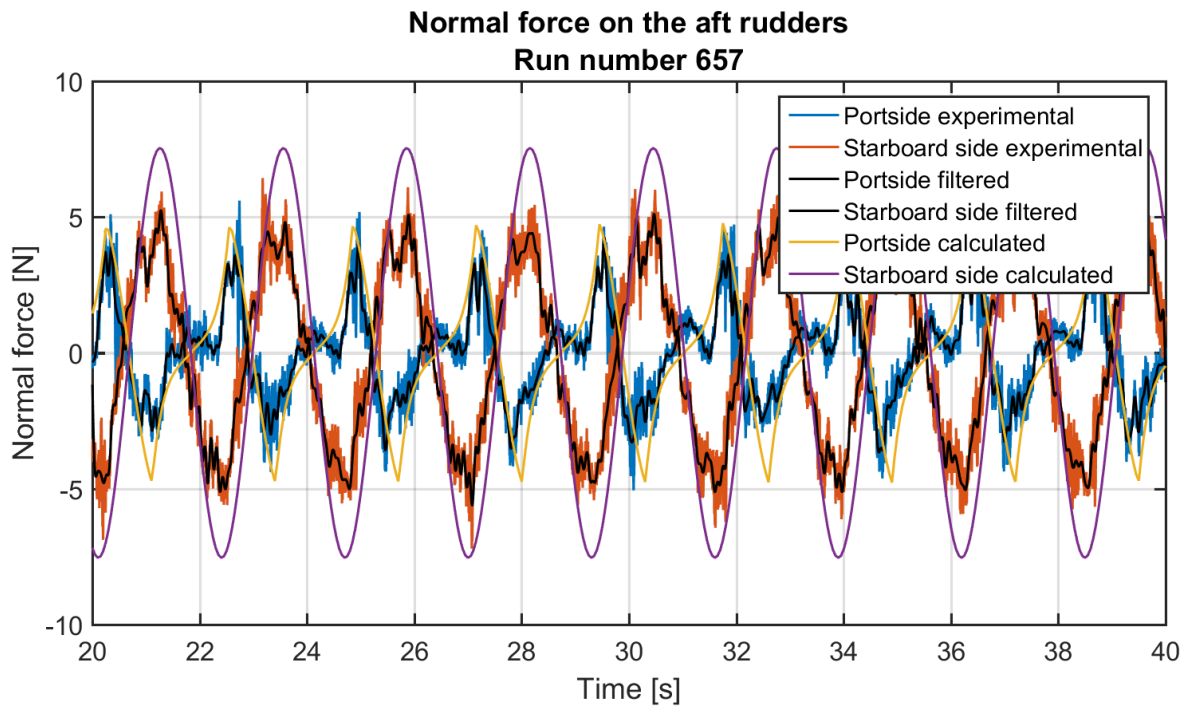


Figure D-53: large X-configuration, without bowplanes
 $V = 1.26 \text{ m/s}$, $\varphi_A = 30^\circ$, $\omega = 2.798 \text{ rad/s}$

Bibliography

- Anderson, J. D. (2011). *Fundamentals of Aerodynamics*. McGraw-Hill, fifth edition.
- Breslin, J. P. and Skalak, R. (1959). Exploratory Study of Ventilated Flows about Yawed Surface-Piercing Struts. Technical report, NASA.
- Chakrabarti, S. (2001). Empirical calculation of roll damping for ships and barges. *Ocean Engineering*, 28:915–932.
- Efimov, A. V., Mrykin, V. O., and Baranov, A. I. (2003). Assessment of superstructure effect upon the submarine stability in surface condition in heavy seas. In *Proceedings of the 8th International Conference on Stability of Ships and Ocean Vehicles*, pages 151–154.
- Falzarano, J., Somayajula, A., and Seah, R. (2015). An overview of the prediction methods for roll damping of ships. *Ocean Systems Engineering*, 5(2):55–76.
- Fossati, F. (2009). *Aero-Hydrodynamics and the Performance of Sailing Yachts*. Adlard Coles Nautical, London, first edition.
- Froude, W. (1955). On the rolling of ships. In *The Papers of William Froude M.A., LL.D., F.R.S. 1810-1879*, pages 40–76. The Institution of Naval Architects, London.
- Hedberg, S. (2006). *Investigation of Submarine Roll Behaviour*. Master's thesis, The Royal Institute of Technology (KTH).
- Himeno, Y. (1981). Prediction of ship roll damping - State of the art. Technical report, The University of Michigan - Department of Naval Architecture & Marine Engineering.
- Hoerner, S. (1965). *Fluid-Dynamic Drag*. First edition.
- Hoerner, S. (1975). *Fluid-Dynamic Lift*. Second edition.
- ITTC (2008). ITTC - Recommended Procedures and Guidelines: Testing and Extrapolation Methods Manoeuvrability Captive Model Test Procedures. Technical report.
- Kato, H. (1958). On the Frictional Resistance to the Rolling of Ships. *Journal of Zosen Kyokai*, 102:115–122 (in Japanese).

- Larsson, L. and Raven, H. C. (2010). *Principles of Naval Architecture - Ship Resistance and Flow*. The Society of Naval Architects and Marine Engineers.
- Molland, A. and Turnock, S. (2007). *Marine rudders and control surfaces: principles, data, design and applications*.
- Ogilvie, T. (1958). The theoretical prediction of the longitudinal motions of hydrofoil craft. Technical report, David Taylor model basin.
- Ruponen, P. (2007). *Progressive flooding of a damaged passenger ship*. PhD thesis, Helsinki University of Technology.
- Schmitke, R. T. (1978). Ship Sway, Roll, and Yaw Motions in Oblique Seas. In *SNAME Transactions*, pages 26–46.
- Sheldahl, R. E. and Klimas, P. (1981). Aerodynamic Characteristics of Seven Symmetrical Airfoil Sections Through 180-Degree Angle of Attack for Use in Aerodynamic Analysis of Vertical Axis Wind Turbines. Technical report, Sandia National Laboratories.
- Tamiya, M. and Komura, T. (1972). Topics on Ship Rolling Characteristics with Advance Speed (in Japanese). *JSNA Japan*, 132.
- van Slooten, M. A. (2014). *Mathematical modeling of free-flooding anti-roll tanks*. Master's thesis, Delft University of Technology.
- White, F. M. (2009). *Fluid Mechanics*. McGraw-Hill, sixth edition.